TESIS DEFENDIDA POR

Rodger Evans

Y aprobada por el siguiente comité:

Dr. Santiago Camacho López

Director del Comité

Dr. Víctor Ruiz Cortés

Miembro del Comité

Dr. Raúl Rangel Rojo

Miembro del Comité

Dr. Rubén Ramos García

Miembro del Comité

Dr. Alfred U'Ren Cortés

Miembro del Comité

Dr. Serguei Stepanov

Coordinador del Posgrado en Óptica

Dr. David Covarrubias Rosales

Director de Estudios de Posgrado

2 de febrero de 2009

CENTRO DE INVESTIGACIÓN CIENTÍFICA Y DE EDUCACIÓN
SUPERIOR DE ENSENADA

PROGRAMA DE POSGRADO EN CIENCIAS
EN ÓPTICA CON ORIENTACIÓN EN OPTICA FÍSICA

Fenómenos físicos en el microprocesado de materiales con láser

TESIS

que para cubrir parcialmente los requisitos necesarios para obtener el grado de

DOCTOR

Presenta:

Rodger Evans

Ensenada, Baja California a febrero de 2009.

RESUMEN de la tesis de **Rodger Evans**, presentada como requisito parcial para obtener el grado de DOCTOR en ÓPTICA con orientación en ÓPTICA FÍSICA . Ensenada, Baja California. febrero de 2009.

Fenómenos físicos en el microprocesado de materiales con láser

Resumen aprobado por:

Dr. Santiago Camacho López

Director de Tesis

Se presenta un estudio experimental de interacción láser-materia, los experimentos se llevaron a cabo usando una estación de microprocesado láser de materiales construida específicamente para este propósito. Se utilizaron cuatro configuraciones distintas de la estación de microprocesado, las cuales se presentan en la tesis junto con los resultados obtenidos. Se utilizó en este trabajo un láser pulsado de $Nd:YAG$, doblado en frecuencia, con una duración por pulso de nanosegundos y miliJoules de energía. Los materiales sujetos a irradiación láser fueron capas delgadas metálicas y modelos de tejido biológico. En el caso de las capas metálicas utilizamos tungsteno (W) y titanio (Ti). Para el tungsteno se consiguió oxidar y cristalizar la capa usando una exposición de apróximadamente 500 pulsos, en un haz enfocado, con una fluencia por pulso de $89 J/cm^2$. En el caso del titanio, utilizando un haz sin enfocar, y fluencia por pulso de $0.25 J/cm^2$, se consiguió el efecto de oxidación y cristalización. Además surgió un efecto nuevo de gran interés, la formación de una rejilla constituida de franjas de titanio y de dióxido de titanio; la periodicidad de esta rejilla es del orden de la longitud de onda ($532nm$), y su orientación está determinada por la polarización de la luz láser utilizada en el procesado. En el caso de modelos de tejido biológico usamos gel de agar, y soluciones de agua con algunas sales, además de un colorante. Usando dos pulsos de nanosegundos a las longitudes de onda fundamental ($1064nm$) y del segundo armónico ($532nm$), se llevaron a cabo experimentos de bombeo-sonda con haces altamente enfocados tanto en gel de agar como en soluciones acuosas. Con la técnica conocida como *laser-flash shadowgraphy* se obtuvieron imagenes de la formación de burbujas de cavitación y ondas de choque. Se determinó el origen de estos dos eventos en la producción de plasma (material-ionizado) debido a la alta intensidad de los pulsos láser utilizados. Se llevó a cabo un estudio detallado de la creación y evolución del plasma, en combinación con otros efectos como la absorción óptica lineal y no lineal del medio. Se encontró que los resultados sobre el plasma se pueden explicar a través del mecanismo de la fuerza ponderomotiva que ejerce el pulso láser sobre la nube de plasma

Palabras clave: ablación láser, películas delgadas, biofotónica, fisica de plasma.

ABSTRACT of the thesis presented by **Rodger Evans**, as a partial requirement to obtain the DOCTOR degree in OPTICS with orientation in OPTO-PHYSICS. Ensenada, Baja California. February 2009.

Physical phenomena excited in laser-material processing

Abstract approved by:

Dr. Santiago Camacho López

Thesis director

In this thesis I present an experimental study of laser-material interaction, where the experiments were performed on a laser-microprecessing system designed and built specially for the study. Several distinct configurations of the microprocessing system were used, and are presented along with the results obtained. This work was performed with a pair of $Nd:YAG$ nanosecond lasers that were used both in their fundamental $1064nm$ wavelength, and frequency doubled $532nm$, with pulse energies up to twenty milliJouls per pulse. The materials that were exposed to the laser were metallic thin films, and biological tissue phantoms. For the metallic thin films, titanium (Ti) and tungsten (W) were used. Tungsten showed evidence of becoming oxidized, and that oxide becoming crystalized after exposure of 500 pulses with a per-pulse fluence of $89J/cm^2$. Titanium was exposed with up to 4000 pulses of unfocused laser irradiation at a per-pulse fluence of $0.25J/cm^2$. From this exposure the titanium showed evidence of becoming oxidized and crystalized; similar to the tungsten. The oxide formation on the titanium formed a surface grating the alternated between titanium dioxide and metallic titanium. The spacing of the grating was on the order of the $532nm$ wavelength for the irradiating light, and the orientation of the fringes was parallel to the polarization of the incident light field. The biological tissue phantoms were agar gel, distilled water, and distilled water with salts and coloured dyes in solution. For these exposures, we used the two $Nd:YAG$ lasers both in the fundamental, $1064nm$ and second harmonic $532nm$ wavelengths, in a pump-probe (laser-flash shadowgraph) system; the infrared $1064nm$ laser beam was the probe beam (laser-flash), and the green $532nm$ laser was the pump beam. The laser was tightly focused inside the liquids/gel. The focal region of the pump beam was imaged onto a CCD where the laser-produced-plasma (LPP), and the shadowgraph IR laser were captured. The images allowed the observation of the laser produced plasma, the formation of a cavitation bubble and the accompanying shock wave. A theoretical study is presented of the creation and evolution of the laser-produced plasma, which includes other effects such as nonlinear

optical absorption, and the saturation of linear absorption. Results from these studies led to the conclusion that the observed LPP created cannot be explained without the used of the ponderomotive-force to alter the plasma density in the laser focus.

Keywords: laser ablation, thin films, biophotonics, plasma physics.

This work is dedicated to the long line of thinkers and doers who investigated the world, not for personal gain, nor technological power, but for the simple enjoyment of figuring something out. I hope that my work becomes a link in that chain. In the end, this is for the future generations, with the hope that I may be as useful and inspiring to them as history has been to me.

Acknowledgments

Thanks go largly to my family, whom have supported me throughout my studies. From the concert stage to the laboratory, my family has been there helping me. To my mother I send the most thanks for her support, physical, emotional, and economical, without her help I would not have reached so far and accomplished so much.

My interest in physics started early, but the road to my university studies is largly thanks to two great scientists. Jerry Mitrovica for his consul when I was in first year at UofT, and Robin Marjoribanks who inspired me to enter the lab and graduate studies. While at Toronto it was my friendship with Santiago Camacho-Lopéz that lead to riding my motorbike to Ensenada Mexico, and finishing my graduate studies here under the Baja sun.

While in Ensenada I have had many teachers helping me with physics, spanish, and culture. Alexandro Ruiz was an excellent lab partner, and taught me a great deal about Mexico, computers, and late night taco stands (sorry again about the appendicitis.) The list of friends who have helped me is long, Raúl , Víctor, Alfred, Noemí, Minerva, Eliseo, Manos, Boogie, Pedro L. Raúl M. and his merry men, and many more, but you know who you are.

In the end it was Tete who had inspired and helped me to finish. Her love, encouragement, and positive approach lead to this final work, and will lead far beyond it.

Ensenada, México — Rodger Evans
2 de febrero de 2009.

Table of Contents

Table of Contents (Continued)

List of Figures

List of Figures (Continued)

List of Figures (Continued)

List of Figures (Continued)

List of Figures (Continued)

Chapter I

Introduction

In the summer of 1998 I entered for the first time an optics laboratory. My first exposure to the field was the design and construction of an x-ray spectrograph to be used in high-intensity terrawatt (TW) picosecond laser-plasma interactions. The combination of theory, design, and ingenious experiment presented in a modern optical laboratory was captivating.

In the ten years that have followed since my first summer of laboratory work, I have had the pleasure of thousands of hours in the laboratory, learning from scientists in all of North America and working with a diverse selection of lasers systems. My laser experience started with the undergrad introductory $HeNe$ gas laser at the University of Toronto, followed by various solid state diode lasers. My first experience with a pulsed laser system was the Nd:YAG *feed back controlled* (FCM) picosecond oscillator in the Ultra-intense & Ultra-fast laser-matter interaction group at the University of Toronto (Marjoribanks *et al.*, 1993). I later went on to work on a Cr:LiSGaF femtosecond laser (Loesel *et al.*, 1997; Sorokina *et al.*, 1996) which was eventually replaced by a Ti:Saph oscillator (Moulton, 1986; Spence *et al.*, 1991). All the above pulsed laser systems were followed by a *chirped pulse amplifier* (CPA) system (Strickland and Mourou, 1985). While working on this thesis experiments have been performed using the Ti:Saph CPA system in Laval University in Quebec, a tunable Nd:YAG laser (EKSPLA NT 342/1 system that used optical parametric oscillator; OPO) at the UC Riverside, and both the Ti:Saph CPA and Nd:YAG lasers in CICESE.

On my arrival to CICESE in November of 2003 the laboratory had a proof of concept,

home built Ti:Saph CPA system (de-la Cruz and Rangel-Rojo, 2006). While not covered in what follows, this system was the focus of my work in CICESE until late 2007 when I was drawn to the experiments reported here in these writings.

I.1 Laser Processing

A focused laser beam can cause ablation of a material through a combination of melting, vaporization and plasma formation. The typical experiment involves focusing the beam onto the surface of a sample which is moved through the focal volume of the laser. The focal volume of the laser is roughly a cylinder with diameter equal to twice the half-width at $1/e^2$ maximum of the beam waist (w_0), and length of the confocal parameter ($2 \times z_R$) which are given by the equations;

$$w_0 = \frac{\lambda}{\pi\ tan(\theta)}, \tag{1}$$

$$z_R = \frac{\pi w_0^2}{\lambda M^2}, \tag{2}$$

where the M^2 (m-squared) of the beam is a measure of the beam quality, $M^2 = 1$ being a perfect Gaussian beam, and *theta* is the half-angle divergence of the beam.

If it is the surface of a target being exposed to the laser beam, focusing increases the irradiance by reducing the beam size; the interaction is effectivly two-dimensional. In opaque or reflective surfaces the electric field will only penetrated with evanescent waves to a depth of several wavelengths. When a hole is drilled it is the continuos ablation of the material surface, as it drops into the material, that forms the eventual hole (the side-walls also become important, and the interaction can become quite complex as the beam coherence drops at deeper holes (Dean *et al.*, 2008).)

Laser ablation is defined as the removal of material through the non-chemical interaction of the laser and material. When a chemical change is induced by the laser

light, the interaction is more complicated, and the light can release more energy than it contains. The term ablation is reserved for interactions where the only energy source causing the removal of the material is the laser.

When a laser focused inside a target is combined with an irradiance dependent absorption, the concept of a focal volume becomes important as energy absorption is confined to the focal region. The confined energy can modify the target material by exploding outward, inducing immense stresses on the material; figure 1 shows a glass slide after exposure to a nanosecond laser. The laser focus was scanned horizontally across the surface of the slide (right side), and vertically through the glass bulk (left side of image.) The photo was taken through a microscope with the slide between a partially crossed polarizer pair. The light regions are caused by stresses in the glass incurred by the sudden loading of energy in the bulk adding a stress induced birefringence to the glass.

The interaction of a laser and target material is dependent on both the duration of the laser pulse and the pulse energy. Many experiments have shown that the mechanisms involved in laser ablation vary wildly depending on the laser irradiance which itself is inversely related to the pulse duration (Liu *et al.*, 1997; Noack and Vogel, 1999; Oraevsky *et al.*, 1996).

A laser primarily heats the electrons in a material. The electrons transferee their heat to the ion lattice. If the electrons are heated enough, their kinetic energy is greater than the potential well binding them to their host ions and they become freed. The freed electrons, accelerated by the electric field, will transfer energy to the ion lattice, and thermalize with the ions within picoseconds; this state of matter is called a plasma. Most analytical and computational models of a plasma consider it as two oppositely charged fluids; two fluid modes (García *et al.*, 2000; Sinha *et al.*, 1979; Weber *et al.*, 2004). The entire mass of hot ions and electrons has an entirely different response to

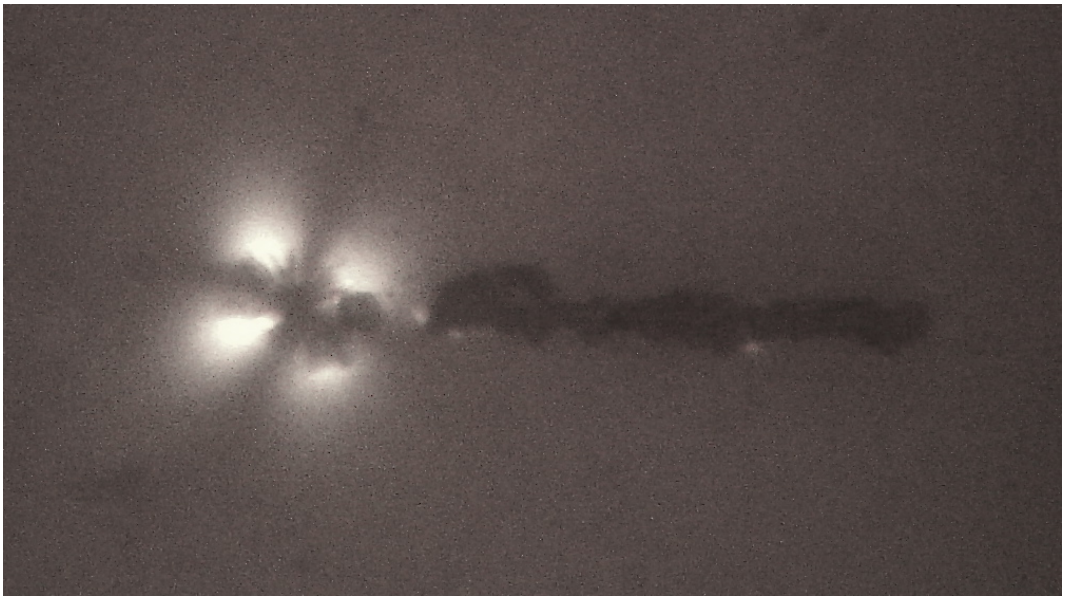

Figure 1: Image of nanosecond laser damage in glass. Image was taken with an optical microscope where the glass sample was between a pair of partially crossed polarizers. The track on the right measured about $1mm$ in length, and was made through surface exposure. The left hand damage was made by a vertical scan of the beam focus through the glass bulk. The pattern of light was caused by laser induced stresses visible as birefringence in the glass.

an applied electric field. The plasma response to a laser depends on the plasma density and temperature. At high enough densities the plasma can become a mirror to the light field. A plasma also has a higher absorption than the cold material, and its index of refraction is less than unity so that it alters the light amplitude and propagation direction. The more time the light beam has to interact with the plasma the more it changes the plasma, and the more the plasma changes the light.

If the pulse duration is shorter than the thermalization time of the plasma, then the laser pulse is over before the plasma has been formed. This allows for the laser to change the electron states without heating the ion lattice. The $Ti : Saph$ and other femtosecond lasers are able to change the index of refraction of glasses and plastics (Itoh and Watanabe, 2005; Mao *et al.*, 2004), generate colour centers in crystals (Hertwig *et al.*, 2004), and rewritable change the structure of a semiconductor from crystalline to amorphous (Solis and Afonso, 2003).

I.2 Experimental and Design approach

Laser machining was, and still is, a reasonable new area of study. The system that has been built is only one of a handful of femtosecond lasers in Mexico, and the only amplified one. The laser processing system, as well, is unique in the country. My investigations began by making a survey of materials exposed to femtosecond and nanosecond laser pulses both to calibrate and compare the processing system to published work, and to look for interactions that called for further investigation.

The original design approach in this thesis was to expose the target to the laser beam in patterns that could be decoded when the target was later analyzed; encoding exposure conditions in exposure geometry. Several computer programs were written to move the machining stages under the laser in controllable vectors. The mechanism that we were looking for, index change and oxidization, are cumulative. Thus by controlling

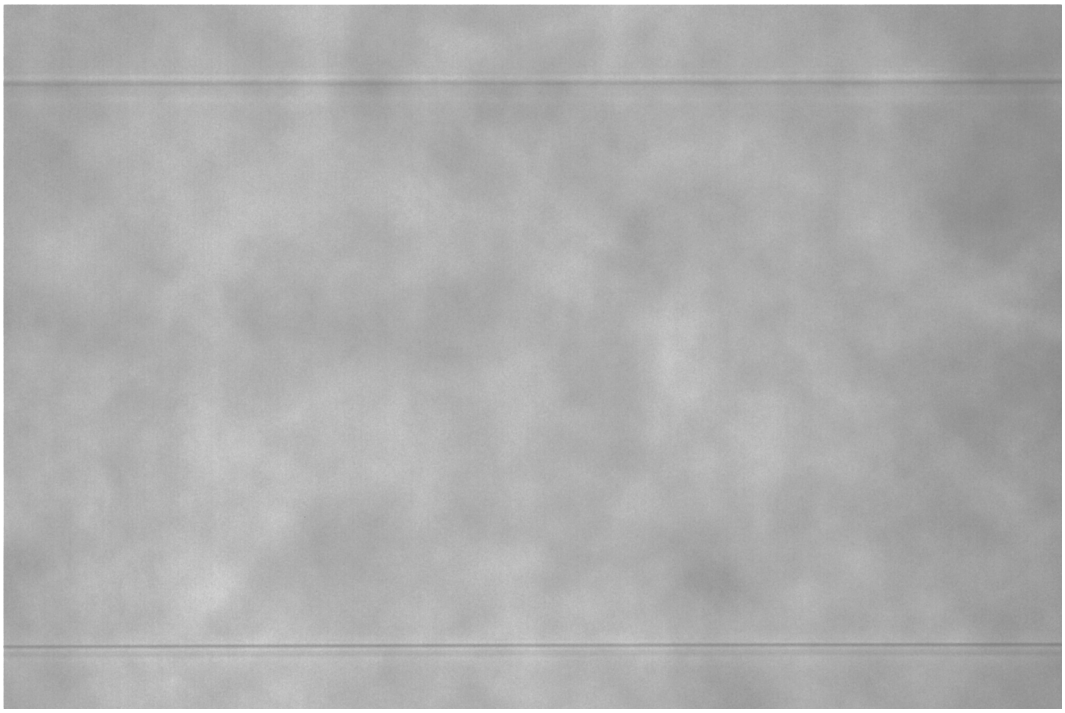

Figure 2: Image taken through phase contrast microscope of waveguides written in fused silica glass by the femtosecond CPA system at the University of Laval in Quebec Canada; experiments performed by author. The laser focus was dragged through the glass parallel to the laser axis with a per pulse energy of $4\mu J$ at $1kHz$ repetition rate and a velocity of $20\mu m/s$.

the scan velocities, beam energy, and spot size, we could set the exposure conditions. In practice, laser induced index change required laser irradiance close to material damage threshold. So that the energy variations in our lasers, generally due to aged systems, spanned the range of energy from non-damaged to damaged material.

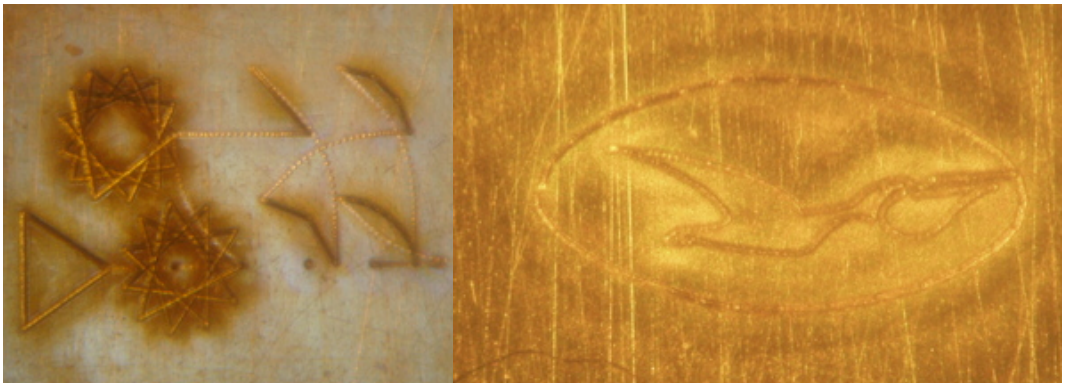

Figure 3: Microscope images of Nd:YAG laser damage on bronze sample demonstrating abilities of stage control program by drawing arbitrary patterns. Damage made with $300\mu J$ per pulse energy, sample velocity of $5\mu m/s$ and a $10Hz$ laser repetition rate. Damage tracks were $20\mu m$ wide.

The problem of laser energy stability was approached from the two sides of the experimental process; preparation and observation. Preparation in this case was to stabilize the laser sources. The laboratory was given several deep cleanings, we reset most of the optical design for better alignment, rebuilding and modifying the multi-pass amplifier (de-la Cruz and Rangel-Rojo, 2006), installing new Ti:Saph crystals, changing Nd:YAG flash lamps, and the installation of a new diode-pumped laser for the Ti:Saph oscillator. At the same time the laser microprocessing system was being redesigned. Observation of cumulative process moved to observation of individual interactions. New cameras and varying types of illumination of the targets were tried, settling to the pump-probe laser flash shadowgraphy; presented in Chapters 3-5. The modifications to the laser sources were evident in the laboratory, while the method of observation, and final results including graphs and images obtained by the microprocessing system are

presented here.

The experiments in this thesis were performed using a pair of nanosecond, Q-switched Nd:YAG lasers at both their fundamental $1064nm$ and frequency doubled $532nm$ wavelengths. The microprocessing system, used throughout the experiments dicussed here, was under constant modification. The system had evolved to accommodate a wide range of experiments; liquid and gelatin, metals, cornea, cell cultures, thin films, glasses, gasses, and plastics, have all found them selves probed and observed by this system. The typical change-over time from one configuration to the other could be completed in less than a day.

I.3 Motivation

Lasers deliver energy with a great deal of control. A laser can be used to deposite heat to a sample with micron resolution while being scanned over centimeters of material. Diffraction of the coherent laser light can be used to control the laser irradiance profile on the material, and the wave nature of the laser can also interact with the electronic states of dielectrics. Examples of frequency mixing and harmonic generation of laser light is common place in a modern optics laboratory. As well as energy, a laser beam carries momentum, and it is both interesting and useful to study how momentum can be transfered from a light beam to a target (as seen in chapter 5.)

There are more efficient ways to deliver energy to a target, but it is in precision that the laser shines [1]. It is the combination of precision, and microprocessing ability of the laser that makes it an ideal tool for ocular surgeries (LASIK), microscopic tools such as optical tweezers and cell lysis (Rau *et al.*, 2006), lab-on-a-chip manufacturing (Sugioka *et al.*, 2004), and in the production of components for the telecom and photonic industry.

[1] pun intended

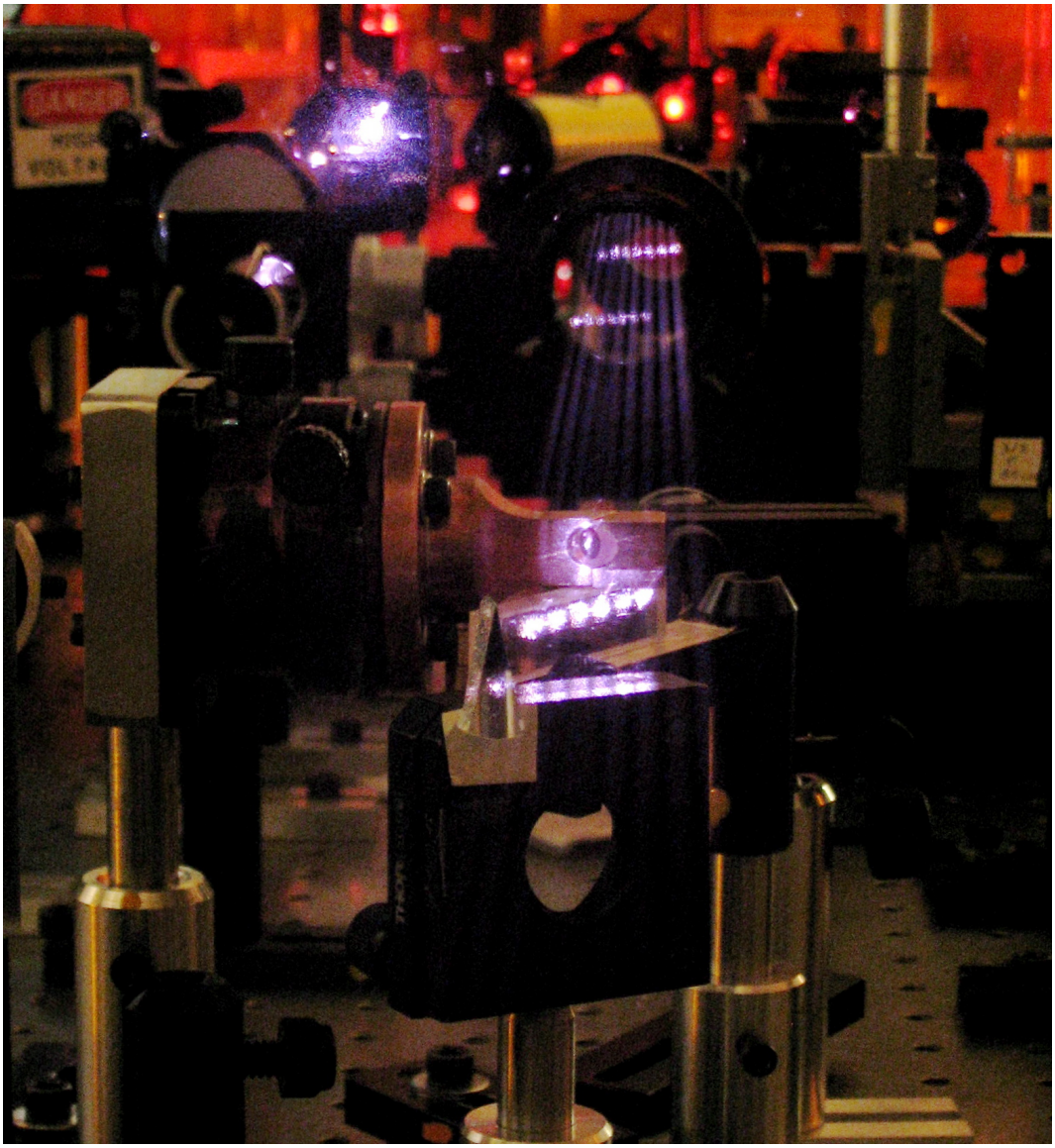

Figure 4: Image of rebuilt multi-pass $Ti : sapphire$ amplifier. The crystal is visible in the center. The laser beams were made visible by a blast of compressed air propellent. The $F2$ glass beam displacer is visible below the crystal. In this image the laser beam was making 14 passes of the laser crystal (a maximum of 16 was achievable up from 8 in the original design.)

A typical table top laser system that is within the means of a typical laboratory, can be from several hundreds of Watts for a continuos laser, to several milijoules at kiloHertz repetition rate for femtosecond lasers. With relative ease, a laser can be focused down to a spot size comparable to the laser wavelength. An ultra-short pulse laser can cause ablation of a material with feature sizes less than the focal spot size; allowing for the nano-processing of sub-cellular targets with a femtosecond laser (Maxwell *et al.*, 2005). Pulses longer than hundreds of picoseconds tend to incur damage spots larger than the beam focus because of interaction with the plasma, and/or the larger pulse energy causes melting through thermal conduction. With a train of ultra-short pulses (the pulse to pulse repetition rate is on the order of nanoseconds) the ablation mechanism can be a mix of short (ns) and ultra short (ps) pulse interactions (Dean *et al.*, 2008; Forrester *et al.*, 2006).

I.4 Background

Since the first demonstration of a working ruby laser by Theodore Maiman in 1960, laser technology has had, from the point of view of high power lasers, four main evolutionary leaps. From the continuos laser (or long microsecond pulses,) the first power jump came from the ability to rapidly release the stored energy in a gain medium into a laser cavity, called Q-switching of the laser oscillator. The Q of a cavity is a measure of the round-trip losses in a cavity, and by opening an optical switch very quickly the laser power increases rapidly and a giant laser pulse is released. This allowed for the build up of energy in the gain medium, and the sudden release of this energy in a nanosecond laser pulse. The first demonstration of a GW laser was in 1965 by John D. Myers, but it was the Nd:YAG Q-switched laser that brought high power lasers to labs in table top systems. The same technology was also used by large government laboratories to provide systems capable of producing terawatts of power, such as the Vulcan laser

from RAL in Britain, and the recently disassembled system at the Lawrence Livermore National Laboratories in the USA. These large systems delivered kiloJoules of energy in several nanoseconds; our modest system could deliver milliJoules per pulse. The newly built NIF (National Ignition Facility) just reported the shining on target of close to two megaJoules from 198 beam lines supplying four nanosecond laser pulses. This massive system was built to study laser driven nuclear fusion and is thought to be able to compress a sample to densities that cause hydrogen atoms to fuse and form helium.

In the 1980's peak power rose with the invention of picosecond lasers and chirped-pulse-apmlification (CPA). These amplifiers allowed the generation of high power ultra-short pulses without damaging the amplifier gain medium. This feat is accomplished by linearly stretching the pulse in time. By stretching a 100 fs pulse to 100ps in duration, the peak irradiance drops to one thousandth its value, so that amplifying the pulse a thousand times will give the same peak irradiance as the unstretched, unamplified pulse. After amplification, the pulse can be recompressed, and a resulting high-energy, ultra-short pulse is created.

It was in the 1990's that CW laser-pumped mode-locked lasers such as the Ti:Saph and Cr:LiSGaF were being constructed by ambitious laboratories. The coming of the new millennium saw the emergence of commercial systems that provided femtosecond laser pulses, amplified to milijoules with a CPA. This provided table top lasers able to produce terawatts of peak power, and to do it at kilohertz repetition rate.

It is no wonder why many labs quickly jumped to ultra-short pulsed lasers. A femtosecond laser (or picosecond) has pulses shorter than the thermal equalization time of electrons and ions in a plasma. This implies that the complicated interaction with plasma, and its plethora of nonlinear interactions that are unsolvable analytically in all but the simplest cases (see chapter 5,) were replaced by the simpler theory of an electron gas with a fixed ion background. Experimentally, the interactions became

much less random; thresholds for ultrashort laser pulse interaction are better defined (Liu *et al.*, 1997).

What the rush to newer technology has done is create areas of investigation that are currently understudied. In the early 1990's when a nanosecond laser was not far behind the cutting edge, images were still being taken with film. Large experimental runs would need a person (usually the least senior student) to take up residence in the dark room. Results came later in the day, hours after the experiment was performed; a closed shutter or blocked beam would go unnoticed, many times until weeks later. In the last chapter of this thesis, data was not only collected and viewed in real time, but could be analyzed and graphed within minutes, this allowed one student to perform and analyze in days, what would have taken a small team in the 1980's a week to perform, and months to analyze.

I.5 Biophotonics: Lasers in surgery

Biophotonics is a huge area of study that has had great success in microscopy, with the development and refinement of the confocal microscope, the fluorescence microscope, and the total internal reflection fluorescence microscope. Specimens can also be manipulated by optical tweezers, and cut by laser micro-scalpels fine enough to carve the mitocondria of a cell (Maxwell *et al.*, 2005).

One of the better known applications of lasers in medicine is in ocular surgeries where the ability to carve with exacting precision is necessary. Laser in situ Keratomileusis (LASIK) involves the use of an excimer ultra violet (UV) laser combined with a microkeratome to help reduce near- or far-sightedness. The microkeratome slices and peals back a thin flap of the cornea and the excimer laser (typically ArF at $198nm$ wavelength) ablates the exposed under layer of the cornea. The cornea has a high absorption in the ultraviolet, and the pulse energy and number are controlled by the

surgeon to accurately change the shape of the cornea (Lerner and Lerner, 2004).

The ability to ablate tissue below the surface without damaging the surface would lend itself to new applications. To study the interaction of a laser in tissue it is common practice to use what is called a *tissue phantom*. A tissue phantom is typically a gelatin, commonly agar, used in place of animal tissue to observe interactions. Agar gels are routinely use to grow cell cultures in many laboratories, and its water content, mechanical response, and optical properties can be adjusted to mimic several types of tissues. Cornea and the fluids within the eye are well represented, optically, chemically, and mechanically by an agar gel. Interactions with skin can also be tested with an agar gel. By using a gel, samples can be made at any time, no animals need to be sacrificed, and sample to sample variations are kept much lower compared to animal tissue.

The Laboratory of Ultra-Short Pulses and Nonlinear Optics at CICESE started research in the ablation of soft tissues with short ($9ns$) and ultra-short ($100fs$) laser pulses; experiments were performed on porcine eye. For the reasons noted above, experiments with agar gel were also performed, and a portion of that work is presented here. Experiments performed with animal tissue were presented in the thesis written by other laboratory alumni (Mina-Rosales, 2007; Romo-Cárdenas, 2007).

I.6 Thin films

Although not a very well known term, thin films are prevalent in society. The electronics industry is dominated by thin film technology used in combination with optical lithographic techniques. Thin films are also used in an optical laboratory, providing coatings on optics which allow for optical frequency dependent reflections. Thin film deposition is predominately made through evaporative coating technologies, but pulsed laser deposition (PLD) is also gaining popularity(Camacho-López; *et al.*, 2004). Once deposited, thin films can be altered through baking and/or exposure to gasses, altering

its composition or structure (Zhuang *et al.*, 2003).

Experiments looking at the ability of lasers to alter a thin film, demonstrate the ability to quickly change the film properties only where the laser was exposed. These interactions have been used for the fabrication of micro batteries (Tang *et al.*, 2006), gas sensors (Korotcenkov, 2007), and other electro-optic devices with both telecommunications and biophotonics applications.

I.7 What follows

The proceeding chapters each investigate a particular case of laser matter interaction that bore interesting results, and when seen as a collection, give a clear idea of how high intensity laser light reacts with matter. The following chapters are more complete when viewed along side with the published works; (Docchio *et al.*, 1988b; Nahen and Vogel, 1996; Noack and Vogel, 1999; Porto *et al.*, 1967; Rau *et al.*, 2004; Vogel *et al.*, 2008; Young *et al.*, 1983; Sipe *et al.*, 1983; del Pino *et al.*, 2004), and the many others cited further on.

The following work is not, however, a complete and systematic outline on the topic of lasers. It is assumed that the reader has a basic understanding of lasers, gaussian beams, and what are atoms, molecules, and electrons. The theory needed is presented along with the experimental observations, if a reference is not given for a stated term it was assumed that the missing information is common knowledge.

The thesis proceeds with chapter 2 which begins with the presentation of laser-induced oxidization of tungsten thin films, and finishes with periodic oxide structures created with an unfocused beam exposure to titanium thin film. Chapter 3 presents laser induced cavitation bubbles formed inside agar gel. Agar gel was used because it is a simple and well understood tissue phantom for cornea and skin. Chapter 4 extends the work done in agar by exposing distilled water with an organic dye which possesses

strong linear absorption similar to that of hemoglobin. The main focus of this section is the interplay of linear, nonlinear, and saturable absorption of the target. Chapter 5 concludes the material presented in chapters 3 and 4 by attempting to explain the formation and interaction of the laser-produced plasma.

Chapter II

Laser processing of thin-films

When the *Laboratory of Ultrashort-Pulse-Lasers for the Study of Nonlinear Optics and Materials* (LU-SNOM) in CICESE was just starting, and the microprocessing system was being built in its first of many incarnations, we were also looking for experiments to test and shape the system. These experiments included the controlled exposure to anything we could get our hands on, and in one case led to collaborations with Sony. It was in 2005 that we were sent metallic thin films to expose to our nanosecond laser.

Thin film technology is found in most photonic and electronic applications. The ability to coat substrates with nanometers to micrometers of metals, dielectrics, or semiconductors has given rise to dielectric mirrors, and optical coatings. With lithographic techniques, patterns on the order of the wave length of light are used for the production of microprocessors and solid state memories. The miniaturization of sensors and detectors is the principal idea behind the *lab-on-a-chip* designs where traditionally large expensive instruments are integrated onto circuits through a combination of microfluidics and thin film electronics (Shuai *et al.*, 2008; Schäfer *et al.*, 2003). The miniaturization of detectors and sensors are in common use now in cell phones that come with a vast array of what use to be hi-tech instruments; global positioning system (GPS), accelerometer, digital cameras, LCD displays, and light sensors.

Of current interest are the properties of metal oxides, which have been observed to display electrochromic properties, where relations between current and colour allow for controllable optical charateristics. Published work on the electrochromic properties of tungsten and titanium oxides have shown great potential for smart window, or chemical and gas sensor technology (Granqvist, 1994; Nishimura *et al.*, 1980; Ozkan, 2001; Korotcenkov, 2007).

Enhancements of the chemical and optical properties have been observed when the

surface is patterned with nanometer size features (Yoshinaga *et al.*, 2009; Yu *et al.*, 2000), which short pulse laser interactions have been observed to be able to accomplish (Evans *et al.*, 2007). Metal oxides have been typically prepared by baking a thin film for several hours in an oven at temperatures above $300°C$. This changes the entire surface, and is reasonably slow. This chapter is a study on the ability for a laser to oxidize and change the lattice state of a metal coating; between different crystalline states and amorphous. A laser heats only under the beam exposure region and oxides can be formed there since high temperatures are reached on the surface, even though the energy content is low and the temperature drops very quickly. The benefit is that the oxide can be written on top of a metal sample where the geometry can be used to enhance the wanted reaction but the substrate is not subject to baking. In addition, the rapid heating and cooling of the surface combined with the high electric field in a typical short pulsed laser cause the formation of nanometer features which have been observed to be randomly or periodically orientated (Zhang *et al.*, 2007; Evans *et al.*, 2007; Camacho-López *et al.*, 2008).

II.1 Nanosecond Pulse Laser-Induced Effects in Tungsten Films

Here is presented evidence of photo-induced effects on crystalline tungsten (W) films. A frequency doubled Nd:YAG ($9ns$) laser was used in our experiments. The tungsten thin films were deposited on silicon substrates by the DC-sputtering technique in an argon atmosphere. The crystalline phase of the deposited tungsten films was determined by X-ray diffraction. Our experimental results show clear evidence that exposure of the tungsten thin films to nanosecond laser pulses resulted in a significant degree of oxidation of the film. As well, the laser exposure proved to be able to change the crystalline structure of the initial tungsten material. Lastly the exposure is shown to make the surface of the initially homogeneous morphology of the film into an unexpected porous material film. A full post exposure analysis of the tungsten thin films included

Energy Dispersive X-ray Spectrometry (EDS) to determine the degree of oxidation of the tungsten film, a micro-Raman system was used to explore and to study the transition of the crystalline tungsten to the amorphous-crystalline WO_3 phase, and images taken with *Scanning Electron Microscope* (SEM) showed a laser-induced porosity which were changes in the initial homogeneous film into a highly porous film with small features in the range from 100 to $300nm$.

II.1.1 Motivation

Several methods have been attempted to nanostructure the surface of the WO_3 to enhance the electrochromic effect in the films (Losier and Ashrit, 2003). Films have been observed to contain sub micron structures of crystalline oxide (Maillé *et al.*, 2003). Further published works outline novel uses of the strong interactions of WO_3 for the detection of ammonia through measurable optical changes in the film (Lazcano-Hernández *et al.*, 2008). Other chemicals have been observed to alter the electronic properties of the film (Krasovec *et al.*, 2001), where morphology and thickness both led to notable changes in the restivity (Liu *et al.*, 2007), and colouration of the film (Georg *et al.*, 2001).

Laser-induced local oxidation in metal films and plates has been reported previously for: titanium (Pèrez *et al.*, 2001), chromium (Lian *et al.*, 2005) and stainless steel (Yang *et al.*, 2005). Using Raman microscopy the pulsed-laser irradiated material was shown to be composed of TiO_2 in its rutile phase. X-ray diffraction has shown the presence of the Cr_2O_3 crystalline phase after a Nd:YAG laser at the fundamental wavelength ($1064nm$) irradiated chromium films (Lian *et al.*, 2005). Several authors had suggested making slab wave guides with thin film coatings, allowing for direct optical measurements of chemical properties, which can be useful in harsh environments where metals and other electronics are not well suited (Lazcano-Hernández *et al.*, 2008; Haydn, 2003). We set out to see what can be done to a tungsten thin film when exposed to focused nanosecond laser light. We made long scans across the surface to see if it was possible to micro-process the film, and what the micro and macro-scopic effects would be.

II.1.2 Growth of the films

Tungsten films were grown by the dc-magnetron sputtering technique using an Argon gas atmosphere. A target three inches in diameter was used (Lesker, 99.95% purity). The deposition parameters were: a DC-Sputtering power of $150W$, the substrate to target distance was fixed at $40mm$, the deposition time was twenty minutes and the substrate temperature was kept at $150°C$. The pre-cleaned silicon and glass substrates were placed in a vacuum chamber which was evacuated to a base pressure of about 1×10^{-6} mbar using a primary mechanical pump and a secondary turbomolecular pump. The working pressure was 1×10^{-3} mbar. A shutter placed between the magnetron and the substrate holder made it possible to clean the target surface before deposition.

II.1.3 Laser processing experimental set-up

The experimental design used to carry out the film laser irradiation is shown in figure 5. The laser source was a Continuum (Minilite II) frequency doubled Nd:YAG laser, which produced pulses with $9ns$ $(FW1/e^2M)$ [1] duration at a $10Hz$ repetition rate, provided a maximum of $20mJ$ of energy per pulse, and had a beam quality measured to be well represented by a $M^2 = 6$ (Maisterrena-Epstein, 2006). The laser energy was attenuated by a polarizer/half-wave-plate pair, and measured with a photo diode cross calibrated to the measured energy at the target focus. We used a spherical $50cm$ lens to focus the beam on target. The laser beam had a HW1/e^2M of $7mm$ at the lens location and was focused to a beam waist with a HW1/e^2M of $220\mu m$; experimentally determined using a CCD array in combination with a graticule grid at the beam waist position.

II.1.4 Laser exposure; thin film processing

Laser exposure of the films was carried out following a computer controlled pattern of laser irradiated segments on the film surface (see figure 6 a). The scan speed was kept

[1] the Full Width at $1/e^2$ of the Maximum value; also $HW1/e^2M$ the Half Width at $1/e^2$ of the Maximum is used

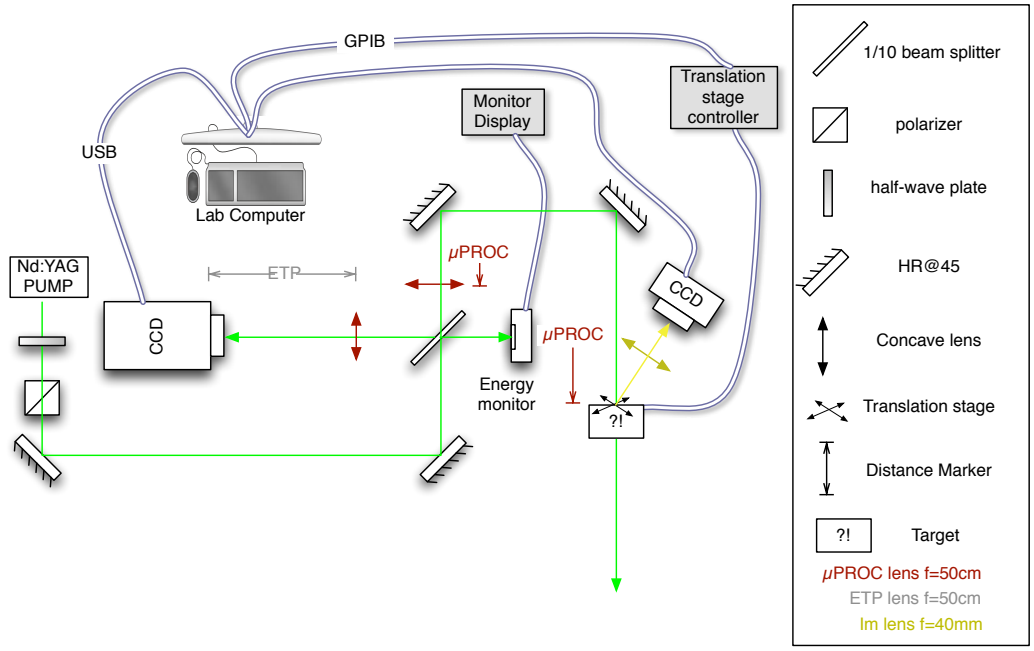

Figure 5: Experimental set-up utilized to carry out the laser irradiation on tungsten thin-film

fixed at $4\mu m/s$ during exposure, while the fluence per pulse delivered to the film was fixed at $161 mJ/cm^2$. Given the scan speed of $4\mu m/s$, the beam waist of $220\mu m$ and the laser repetition rate at 10 Hz, a total number of 550 pulses were delivered at any given spot on the irradiated zone.

II.1.5 Characterization techniques

The as-deposited films were characterized by X-Ray Diffraction (XRD) using a diffractometer (Siemmens, D-5000), Scanning Electron Microscopy (SEM) with a Phillips $XL-30$ microscope and Energy-Dispersive X-ray Spectrometry (EDS)[2]. The pulsed-laser irradiated zones were analyzed by Raman Microscopy (RM) using the micro-Raman system ($HR-800$ LabRam)[3], SEM and EDS.

[2]EDS measures an emitted x-ray from a source bombarded by high energy electrons. The x-ray wavelength and intensity are used to devise the target sample elements

[3]Raman spectra measures slight shifts in the spectrum of an illuminating laser after scattering from a target. These shifts are caused by energy loss to the material lattice when light is scattered off the sample creating a photon-phonon pair. The loss of photon energy is equal to the created phonon

II.1.6 Results and discussion

The $O : W$ ratio for the as-deposited film obtained from EDS measurement was 0.33. The diffractogram (not showed here) of the as-deposited tungsten film indicated that the film material is a mixture of $\alpha - W$ and $\beta - W$ (low oxidized tungsten, W_3O) crystalline phases. A morphological and structural analysis of these phases obtained in films grown by sputtering has been reported in the literature (Maillé *et al.*, 2003).

SEM micrographs of the irradiated tungsten thin film are shown in figure 6. In figure 6(a) a square pattern recorded with a net fluence of $89 J/cm^2$ can be seen. Three magnifications of a linear segment of the irradiated zone are showed in figures 6(b-c). The irradiated surface became porous after the laser exposure. The pore size was 100 to $300nm$ in diameter. The $O : W$ ratio for the irradiated zone increased to 0.48 from 0.33 in the as deposited film.

Raman spectra in the interval $600 - 1200 cm^{-1}$ is shown in figure 7 for the following cases: (a) the as-deposited film, (b) irradiated zone at $89 J/cm^2$ (net fluence) and (c) crystalline monoclinic-WO_3 (Aldrich, 99.99% purity powder). The Raman spectrum in trace (c) in figure 7 is of the commercial WO_3 powder, which contained two peaks located at 715 and $806 cm^{-1}$. These peaks corresponded to $W - O$ stretching vibration modes of a ReO_3 type structure. In contrast, Raman spectrum of the as-deposited film did not show any Raman fine peaks, this is probably due to the metallic feature of the $W - W_3O$ films. Trace (b) in figure 7 was the Raman spectrum corresponding to the pulsed laser irradiated zone at a net fluence of $89 J/cm^2$ (per pulse fluence of $161 mJ/cm^2$.) This spectrum was constituted by three bands centered at $695 cm^{-1}$, $820 cm^{-1}$ and $950 cm^{-1}$. The bands at $820 cm^{-1}$ and $695 cm^{-1}$ can be associated to the vibration modes of the monoclinic phase of WO_3 ($806 cm^{-1}$ and 715 cm^{-1}) (Krasovec *et al.*, 2001). The shift of the bands can be due to the distorted octahedra in the highly sub-stoiquiometric tungsten oxide structure. According to the literature (Cazzanelli *et al.*, 2001), the band at $950 cm^{-1}$ was caused by the $W = O$ stretching modes of terminal oxygen atoms. This laser-induced porous structure in the films was probably allowing for the formation of the oxygen terminal bonds associated to the $950 cm^{-1}$

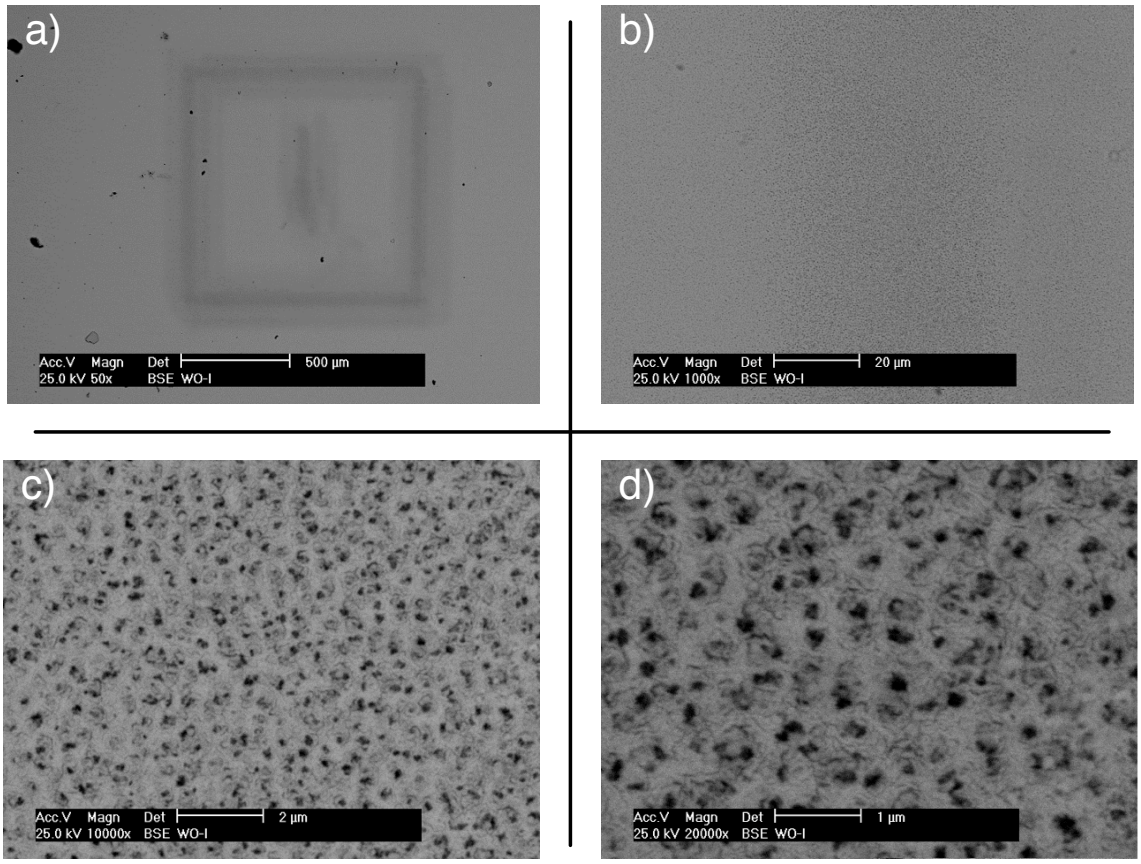

Figure 6: Porosity induced on the irradiated surface of a $W - W_3O$ film. a) Square pattern formed by linear segments irradiated at a net fluence of $89 J/cm^2$; (b), (c) and (d) magnifications of a linear segment showed in (a)

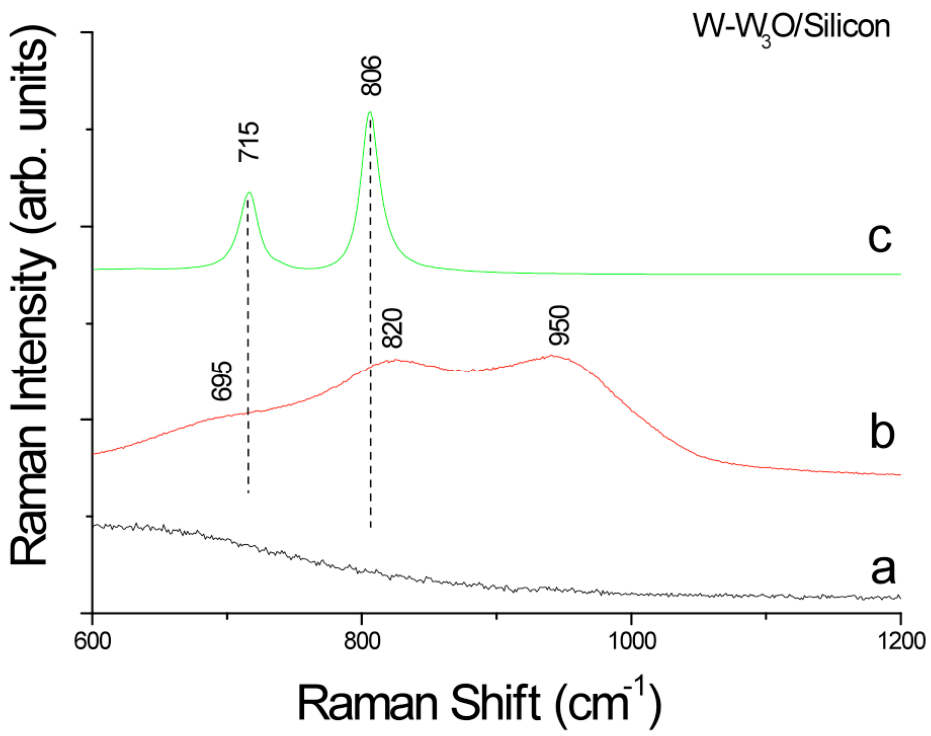

Figure 7: Raman spectrum of tungsten: a) as deposited tungsten thin film; b) tungsten after irradiation of 500 pulses at a fluence of $89 J/cm^2$; c) commercially available crystalline monoclinic-WO_3 powder.

band in the Raman spectrum seen in trace (b) of figure 7.

II.1.7 Conclusion of Tungsten Exposures

Above was shown evidence of three effects that appeared after pulsed laser irradiation of $W - W_3O$ films. A modest increment of the oxygen content in the irradiated zone was identified by EDS measurements. The features of the Raman spectrum of the irradiated zone indicate that the irradiated material is a mixture of a dominant amorphous phase and a crystalline tungsten oxide while the surface obtained a nano-porosity structure; such laser-induced material porosity might be useful for gas sensing applications. This work was presented at the 8^{th} International Conference on Laser Ablation (COLA) and

is published in the conference proceedings (Evans *et al.*, 2007).

Titanium thin films were exposed in the same experimental session as the tungsten thin films presented above. A noticeable change of colour in the titanium thin film was observed, however, when placed into the vacuum chamber for SEM imaging the thin film detached from the substrate. All the information was lost, but the initial results were enticing enough that we quickly obtained new samples of titanium thin films. The next section in this chapter present the resulting observations.

II.2 Polarization Dependent Single-Beam Laser-Induced Grating-Like Effects on Titanium Thin Films

This section presents results on polarization dependent laser-induced effects on titanium (Ti) thin films. Titanium films were irradiated in ambient air, using an unfocused nanosecond Nd:YAG laser with $532nm$ wavelength light in a $9ns$ FW1/e^2M pulse duration operating at $10Hz$ repetition rate. A series of pulses with fluence well below the ablation threshold were able to form grating-like structures, whose grooves ran parallel to the linear polarization of the incident beam. No grating-like structures were obtained when circularly polarized light was used. Our results revealed the remarkable formation of tiny ($100nm$ and even smaller diameter) craters, which self arrange quasi-periodically along the ridges (never on the valleys) of the grating-like structure. Optical and Scanning Electron Microscopy were used to study the laser-induced changes on the surface of the titanium films. Micro-Raman spectroscopy was used to measure the irradiated areas on the titanium films for the formation of crystalline structure. Raman analysis demonstrated that the grooves in the grating-like structure were built up by laser-induced oxidation of the titanium thin film. This published work (Camacho-López *et al.*, 2008), was the first time, to the best of our knowledge, that periodic surface structures were reported to be induced below the ablation threshold regime, with the grooves made of crystalline metal titanium dioxide where the TiO_2 was in

the well known Rutile phase. The laser irradiated areas on the film acquired selective holographic reflectance determined by the laser polarization; the grooves were parallel to the beam polarization, and were not formed when a circularly polarized beam was used.

II.2.1 Motivation

Oxidized metal films are well known for their electro-optical and electro-chemical properties. Titanium dioxide (TiO_2) has been studied for its ability to function as a catalyst for chemical reactions helpful in the decomposition of odors and bacterial. In terms of lasers, work has been published looking at the changing electrical restivity of a laser exposed TiO_2 film (Tsukamoto *et al.*, 2008). Titanium dioxide has been investigated for its use as a gas sensor (Georg *et al.*, 2001). Recently TiO_2 has been in the news for its use in memristors developed by HP (Kanellos, 2008). Titanium has also been widely used in medical devices such as medical implants; studies have been published on the attributes different surface morphologies have on binding of cells to titanium implants (Diniz *et al.*, 2002); as well as other medical uses (Brunette *et al.*, 2001). Using a $Nd:YAG$ laser to change the chemical properties of titanium films has been published (György; *et al.*, 2004) , and periodic structuring of similar films have been induced by femtosecond lasers (Zhang *et al.*, 2007). The ability to make periodic structure in metals was published with theoretical and experimental evidence (Sipe *et al.*, 1983; Young *et al.*, 1983) and continues as an active area of study(Vorobyev and Guo, 2005; Pedraza *et al.*, 2003). But in those experiments, the laser was operating above the damage threshold, and the metal remained chemically unchanged. Discovering the ability to form nano-scale structure on TiO_2 is hoped to combine with the increasing list of electronic and optical properties of this metal oxide, and the myriad of medical applications able to produce useful and interesting lines of investigation.

In the first set of experiments performed on metal thin film, both tungsten (W) and titanium (Ti) were exposed to the $Nd:YAG$ laser. The most notable changes in the film were a series of colour change that varied with increased laser fluence. Figure 8

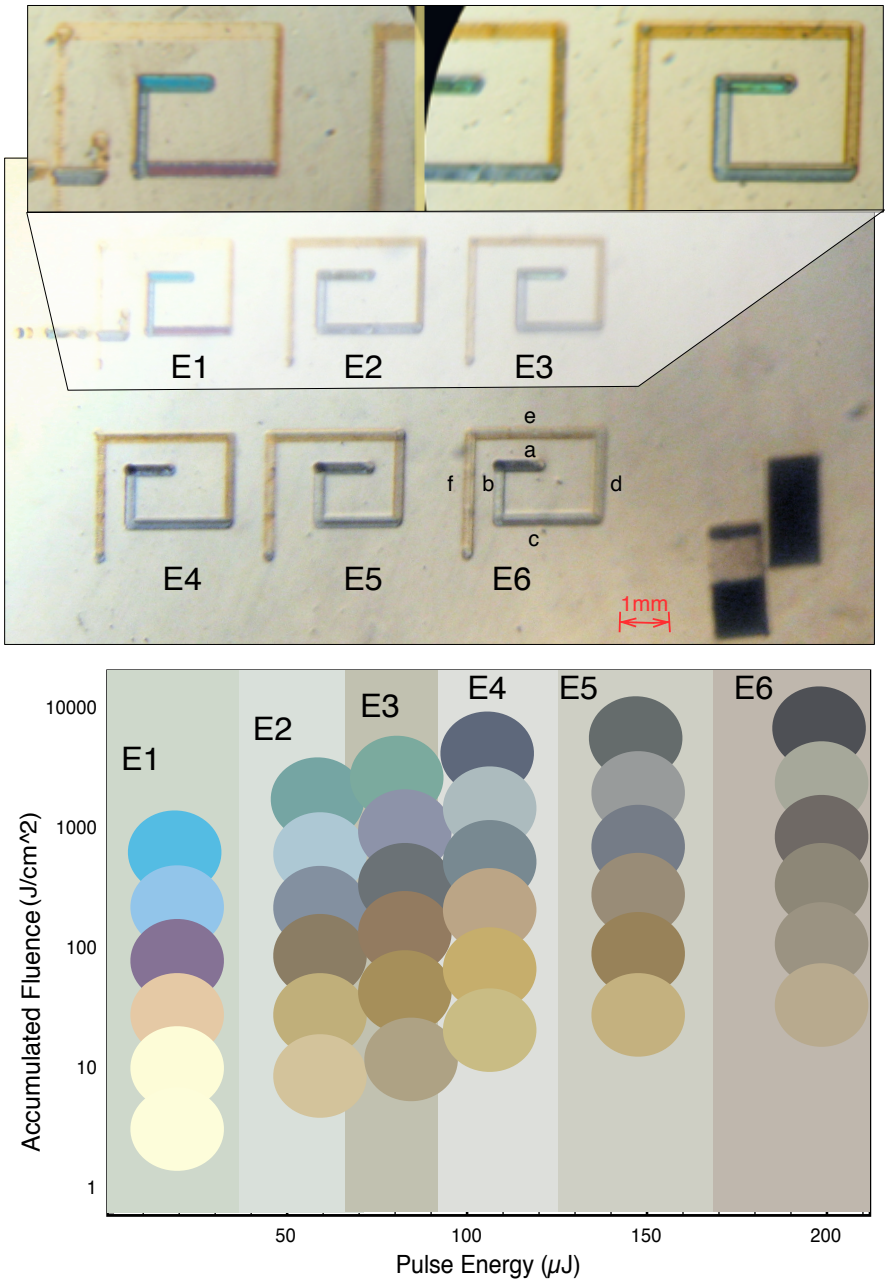

Figure 8: Top:Titanium thin film in fluence scan (swirl) stage pattern. The scan speeds were: $(1, 3, 10, 30, 100, 300)\mu m/s$ for segments (a, b, c, d, e, f) and with energies of $(20, 60, 80, 102, 150, 198)\mu J/pulse$ for respectively E1, E2, E3, E4, E5, E6. Bottom: plot of fluence to pulse energy. The data point is the colour of the line segment, and the background colour is of the unexposed Ti film.

demonstrates the dependance of the laser induced colour change to both single shot and cumulative fluence. Above pulse energies of $100\mu J$, the target began appearing more black/silver which was thought to be the Si substrate visible because the covering film had been ablated with the laser. Where more than ten pulses arrived on target a distinctive change from yellow to blue-green colouring can be seen in the film. So it was not just the energy in the pulse, but how many pulses made it on target that influenced the colour change; speed 'd' for energy $E1$ had the same accumulated fluence as speed 'c' for energy $E4$, but $E4$ was yellow where $E1$ changed violet.

The size of the processed region shown in figure 8 made analysis with an EDS difficult. A larger region was attempted with a raster scan, and is seen on the bottom right of the image in figure 8. Further attempts to expose a large area where to use a cylindrically focused beam scanned over the thin film, and finally an unfocused beam was shone on target. This last, and simplest solution proved the most lucrative.

II.2.2 Film deposition

Titanium thin films were deposited using a pure (99.9%) titanium target that was sputtered in an Ar discharge by means of a DC magnetron operated at a pressure of 1.0×10^{-6} Bar, and at a $30W$ discharge power. The substrates used in these experiments were silicon (100) wafers. The target-substrate separation was kept at $7.0cm$ during deposition. The substrate was kept at room temperature during deposition. The as-deposited titanium thin-film's thickness was measured by profilometry to be $320nm$ thick corresponding to a deposition time of 40 min. The as deposited titanium films were characterized by X-ray diffraction (diffractogram not shown here,) obtaining evidence that the film was in the crystalline hexagonal $\alpha - Ti$ phase.

II.2.3 Pulsed laser irradiation of the film

The microprocessing system, figure 9, was set for the exposure of an unfocused beam on target with $10mJ/pulse$. The frequency doubled Nd:YAG laser was used at $10Hz$ and had an on-target FW1/e^2M beam diameter of $2.4mm$. Up to 4000 pulses were

exposed per site. The per pulse beam fluence was $\sim 0.24 J/cm^2$, which was well below the ablation threshold for pure titanium of $0.8 J/cm^2$ (Vorobyev and Guo, 2007).

Before landing on target the laser pulse passed through a half-wave plate, polarizer, and quarter-wave plate. The three optics were used to control the amount of light, and its polarization on target; linear polarization direction, or circular polarization. Linearly polarized light at two orthogonal directions, and circularly polarized light, were used in the proceeding experiment.

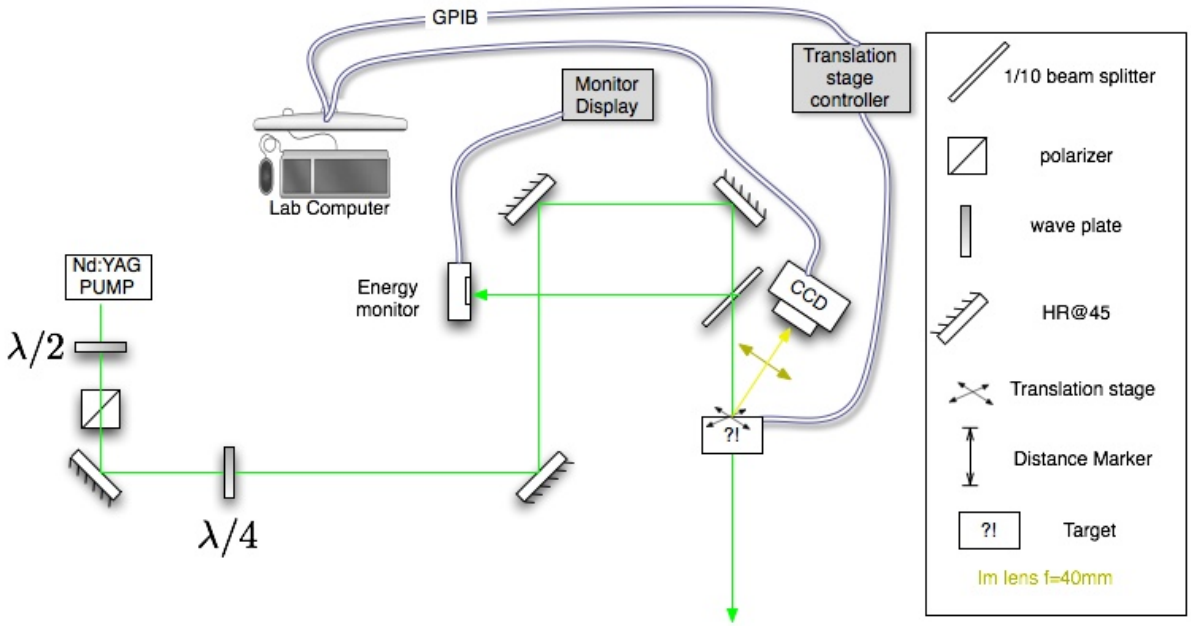

Figure 9: Optics schematic design of the microprocessing system used in the titanium thin film exposures

II.2.4 Selective reflectance of single beam grating-like recording

Under visual examination the exposed regions appeared to have a chromatically disperse reflection, with a small off-angle tolerance of $\pm 10°$. Hypothesizing that the reflection was due a grating like feature, we set out to test the response of the hypothesized grating to the polarization of the writing laser beam. Figure 10 is composed of three images

taken of the exposed thin film where the film is rotated 45° in consecutive images. Noted on the images is the polarization of the laser used in the samples relative to the image axis; the swirls mentioned in section II.2.1 are noticeable in the upper part of the sample. In image *a)* of figure 10, reflection of the light can be seen from locations $2, 3, 4, 7$; the illumination for the image was incident to the target perpendicular to the polarization of the P_{linear} exposure. In image *c)* of figure 10 locations 1, 6 were reflective; in this case the illuminating light was perpendicular to $P_{l-orthogonal}$. Image *b)* was taken when neither laser polarization was perpendicular to the illuminating lamp used for the photo. The region exposed with a circularly polarized laser, Location 5 in figure 10, did not give and diffractive reflection similar to the two linearly polarized cases.

II.2.5 Characterization of the irradiated regions

Directly after each experiment the samples, illuminated by a tungsten bulb powered fiber bundle microscope lamp, were imaged under an optical microscope and by unaided visual inspection. A favorable angle of observation and illumination could be found that displayed a strong coloured reflection from the irradiated regions. The irradiated areas were also imaged by scanning electron microscopy (SEM) using a *Philips XL* microscope and a micro-Raman spectrometer (HR-800-LABRAM, Jobin-Pvon-Horiba). The Raman spectrometer used a linearly polarized He-Ne laser ($632.8nm$) as on excitation source. With a $100\times$ objective lens mounted on a an Olympus XL-41 microscope, the Micro-Raman beam was focused down to a $5\mu m$ diameter spot; giving a laser power density of $\sim 28kW/cm^2$.

II.2.6 Single beam surface grating-like recording

SEM images of the Ti thin-film samples are shown in figure 11. Well defined grating structures were found to occur parallel to the beam polarization; no gratting structure occured when the laser was circularly polarized. The period of the grating was found to be between $400 - 600nm$ with the average value being of the order of the laser

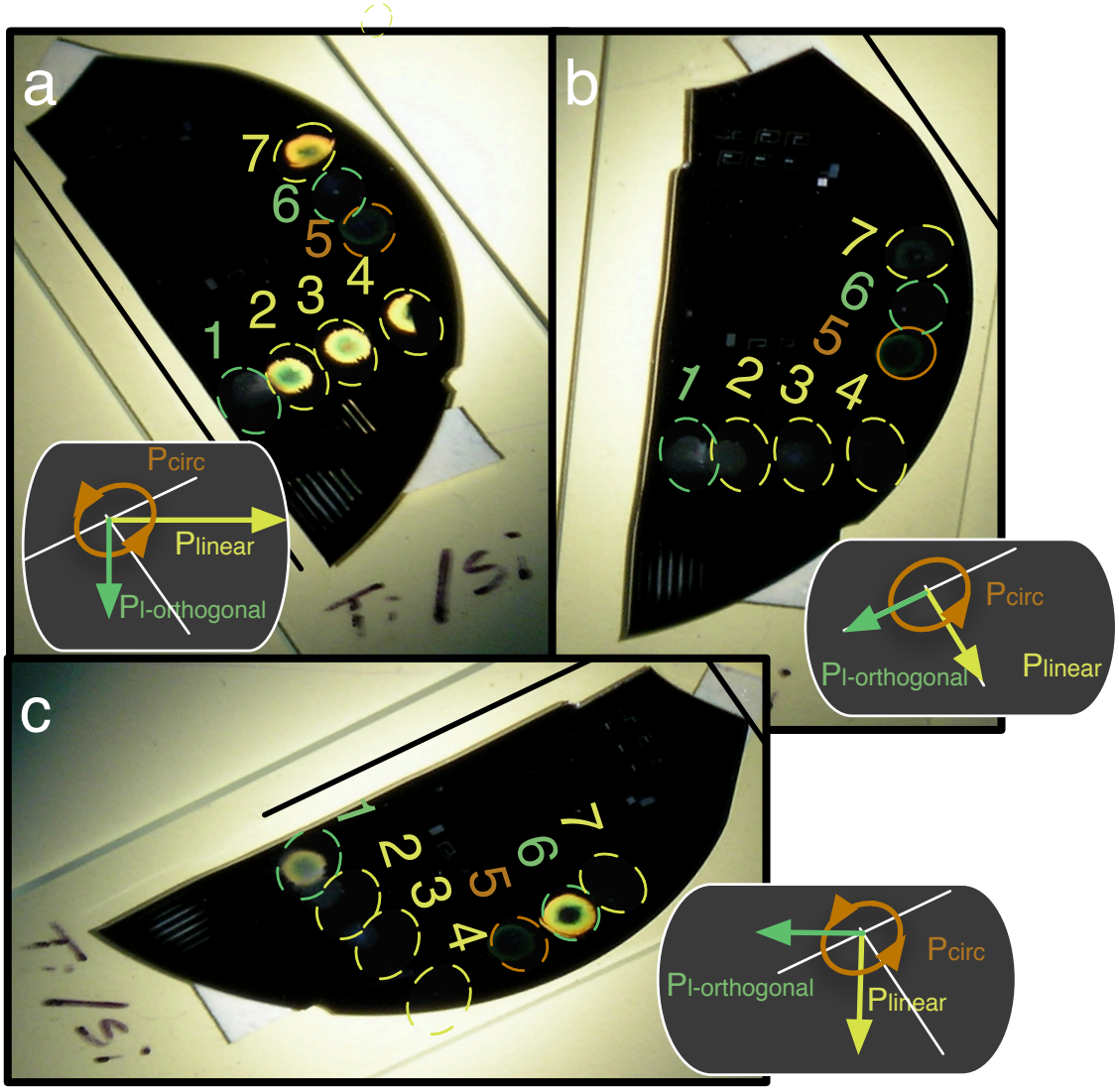

Figure 10: Titanium thin film illuminated with collimated white light. Locations $2, 3, 4, 7$ were exposed with linearly polarized laser light, with the orthogonally polarization on regions $1, 6$; location 5 was exposed with circularly polarized light. The light polarization has been drawn on each image

wavelength of $532nm$. Nano-craters less than $100nm$ in diameter were formed only on the ridges, but never in the valleys; see figures 11 and 12. The nano-craters were also observed in the case of circularly polarized light, but the spacing and location of the craters did not show the same periodicity as seen in the linearly polarized case. In figure 11, the absence of the grating shows the nano-craters and the lightened region confined to a non-periodic pattern around defects in the Ti surface.

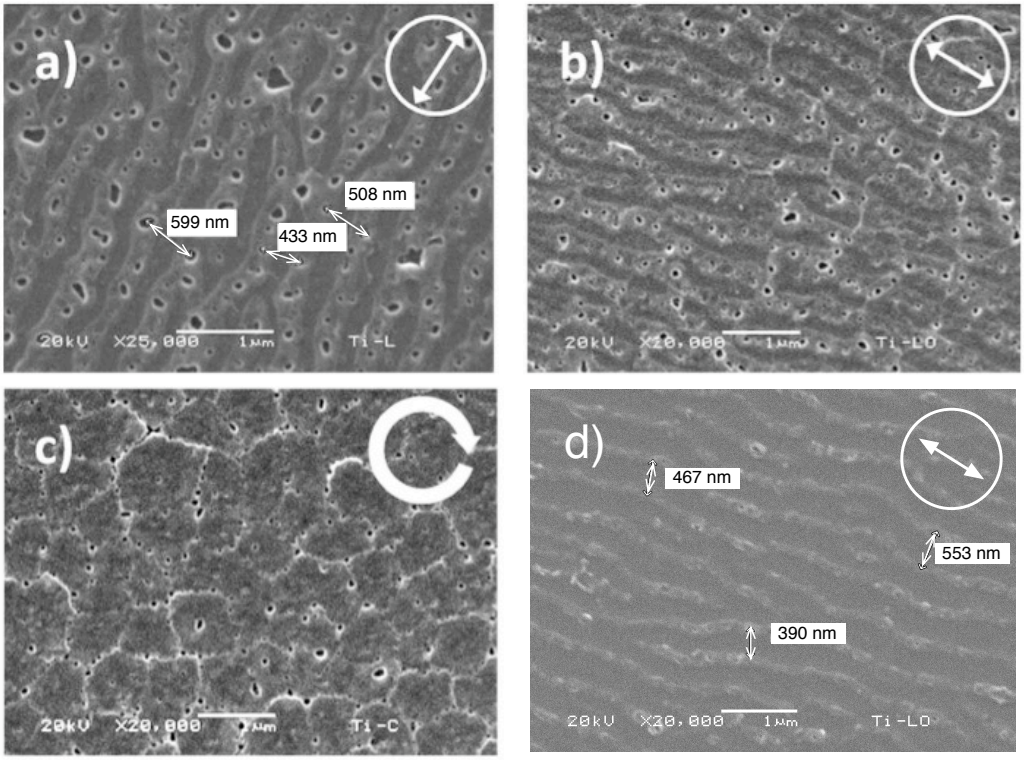

Figure 11: SEM images of laser exposed titanium thin-film coating. All images had the same exposure settings for the laser except for the laser polarization which was a) linear, b) linear orthogonal and c) circular. The laser polarization direction is noted on each image. Notice the hole pattern forming on the lighter imaged fringes with the linear polarization, but randomly distributed when the laser was circularly polarized. d) was taken from the same sample as b) but a location further from the center of the beam where the fluence of the laser was lower.

II.2.7 Surface morphology features

By looking at the sample at an oblique angle, as seen in figure 12, the surface structure of the film could be more easily observed. The lighter regions of the sample were the ridges of the grating. The nano-craters were completely confined to the ridges, and the opening of the craters have nano-spikes reaching away from the sample surface; the ridges were formed by growing films of TiO_2 (see section II.2.8.)

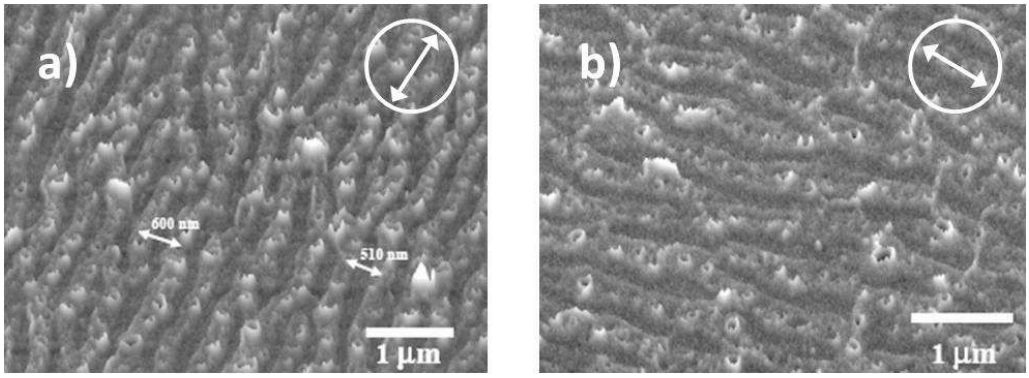

Figure 12: SEM images taken at an angle to the sample surface of the laser exposed titanium thin-film coating. Each region was exposed with linearly polarized light whose polarization direction is marked on the image.

By observing the film at different distances from the beam center, an effective scan of fluences was made. As the fluence decreased (moving further from the center of the beam) the size of the ridges decreased, and so too did the presence of the nano-craters in the ridges; see figure 11 *d).*

II.2.8 Characterization of the induced phase changes on the laser-irradiated region

The Raman spectrum from $400 - 800cm^{-1}$ is shown in figure 13 where trace (a) was recorded with the as deposited titanium film, and (b) was taken by focusing the $HeNe$ laser beam in the center of an exposed region shown in figure 12 (a).

The non-irradiated, as deposited film showed no characteristic spectrum. The Raman spectrum after irradiation had a peak centered at $521cm^{-1}$ which corresponds to

the silicon substrate. Spectrum 13 (b) also contains peaks at 439 and 613cm^{-1}. These peaks were shown by (Porto *et al.*, 1967) and (Beattie and Gilson, 1969) to be from the E_g and A_{1g} active Raman modes for the tetragonal Rutile structure of TiO_2, respectively. From this, it can be concluded that the laser was causing the formation of crystaline TiO_2. The micro Raman did not have the spatial resolution to determine the composition of the ridges relative to the valleys, but in the SEM images the ridges show change while the valley appeared to be composed of unaffected titanium. From this it can be concluded with reasonable probability, that the laser affected changes of the titanium film to grow periodic ridges of TiO_2.

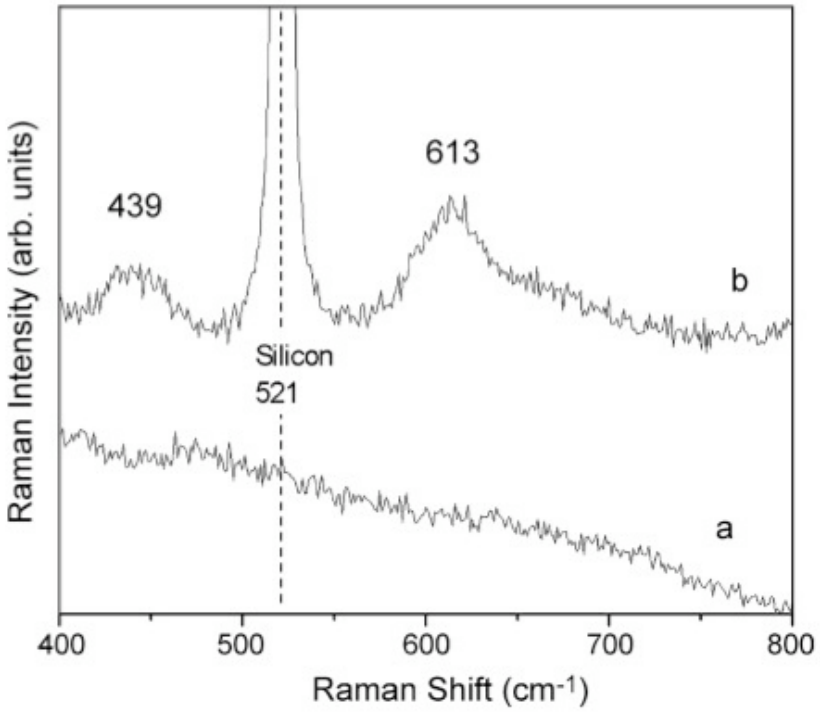

Figure 13: Raman spectrum of the titanium film: a) as deposited (non-irradiated) film and b) irradiated area shown in figure 12a.

II.2.9 Conclusion for Titanium Thin-Film

After exposing a titanium thin film deposited on a silicon substrate to several thousand pulses of an unfocused $Nd:YAG$ laser evidence of the formation of Rutile phase TiO_2

was inferred through raman spectrum and SEM images. A grating with spacing on the order of the laser wavelength, and ridges running parallel to the laser polarization were observed. The ridges were perforated by nano-craters. When the laser was circularly polarized the nano-craters appeared in irregularities of the thin film without any periodicity noticeable. The edges of the nano-craters were spiked away from the surface.

The theoretical treatment of LIPSS (laser induced periodic surface structures) formation in metals and semiconductors offered by Sipe (Sipe *et al.*, 1983) considers the scattering of light from the microscopic surface roughness. His discussion began by looking at the wave vector components parallel to the surface $\bar{\kappa}_i$ and the assumption that the material surface has an inhomogeneous absorption with magnitude $\eta(\bar{\kappa};\bar{\kappa}_i)|b(\bar{\kappa})|$; $b(\bar{\kappa})$ was " the measure of the surface roughness at κ, and $\eta(\bar{\kappa};\bar{\kappa}_i)$ is a response function describing the efficiency with which surface roughness at $\bar{\kappa}$ leads to inhomogeneous absorption just below the selvedge for a given incident field." Sipe broke the interaction into three regions; the vacuum in front of the sample (from which the laser is incident on the sample), the bulk of the material, and what he calls the *selvedge* region, which contains all the surface roughness. The selvedge region is where the LIPSS pattern is formed. The electric field in this region induces a material polarization of

$$\bar{P}(\bar{r}) = \chi(\bar{r})\bar{E}(\bar{r}) \quad (0 < z < l), \tag{3}$$

where l is the thickness of the selvedge region, $\bar{E}(\bar{r})$ is the laser field, and χ accounts for the presence of material in that part of the selvedge region.The material susceptibility becomes,

$$\chi(\bar{r}) = \chi b(\bar{r}), \tag{4}$$

where $b(\bar{r}) = 0, 1$ if $\bar{r}$ region is vacuum or filled by material respectively.

The material polarization is found from the selvedge region was considered by Sipe as the polarization of the areas with material combined with the part of the region occupied by vacuum (or in our case air). Sipe was considering a material that could

be melted or vaporized, but our case includes the formation of titanium dioxide. As well, the selvedge region in a thin film will be proportionately much larger relative to the bulk than the slabs of metals considered. In fact, it appears that the nanocraters made in the sample are holes in the titanium film, and what is seen inside is the silicon substrate. The substrate will also have a different material susceptibility than the thin film. Finally on this point, is that the titanium is being converted to titanium dioxide so that we see that $\chi(\bar{r})$ in the selvedge region becomes;

$$\chi(\bar{r}) = \begin{cases} b(\bar{r})\chi_{Ti} & \text{b=1 for Ti, otherwise 0,} \\ d(\bar{r})\chi_{TiO_2} & \text{d=1 for } TiO_2\text{, otherwise 0,} \\ f(\bar{r})\chi_{air} & \text{f=1 for air, otherwise 0.} \end{cases} \tag{5}$$

To simplify the problem, the material could be considered to be in vacuum, but the χ from the TiO_2 cannot be simplified away. More than this, TiO_2, as was noted in the introduction to this section, has a very rich list of interactions that change its electric and optical properties; including effects of temperature .

After defining χ for the system, Sipe continued by considering the parts of the metal in the selvedge region as dipoles. (It should be noted that Sipe worked through his solutions in spatial frequency space.) The radiation field for the collection of dipoles has no radiative solution because at the metal vacuum interface Maxwell's equations disallow any propagations. But the defects in the material surface do not vanish, and offer significant contribution to the EM wave source term; the component here is both material and polarization dependent. Sipe called these nonradiative field structures radiation remnants. The remnants are dependent both on the material index of refraction, feature size in the selvedge region and the light radiation frequency. Effectively, the laser's electric field experiences random scattering from the surface roughness while the scattered fields interfere with each other. Considered in frequency space, the interference of the scatters lead to energy transfer to the all remnant modes parallel to the surface, and those that constructively interfere become the dominant features.

The energy absorbed by the bulk of the material scales with the intensity of the laser field. The energy taken by the remnant modes on the surface are considered to be

small perturbations on the field. The inhomogeneous part of the field is shown to be

$$A(\bar{\rho}) = 4\pi\,\omega\,l\,Re\left\{b(\bar{\kappa})[\nu(\bar{\kappa}_+) + \nu^*(\bar{\kappa}_-)] \times e^{i\bar{\kappa}\cdot\bar{\rho}}\right\}, \tag{6}$$

where

$$\nu(\bar{\kappa}_\pm) \equiv \bar{E}_t^* \cdot \bar{h}(\kappa_\pm) \cdot \bar{\gamma} \cdot \bar{E}_i. \tag{7}$$

Where $\bar{E}_t$ and $\bar{E}_i$ are the incident and reflected fields, γ represents the fill factor in the selvedge region, and $\bar{h}(\bar{\kappa}_\pm) = \sum_{i,j} h_{ij}\hat{e}_i\hat{e}_j$, for $\hat{e}_i = \hat{s}, \hat{\kappa}$ and $\hat{z}$, are orthogonal directions with $\hat{\kappa}$ parallel to the laser field, and with

$$h_{ss} = 2i\omega(w_0 + w)^{-1}, \tag{8}$$

$$h_{\kappa\kappa} = 2iww_0\omega^{-1}(w_0\epsilon + w)^{-1}, \tag{9}$$

$$h_{zz} = 2i\kappa^2\omega^{-1}(w_0\epsilon + w)^{-1}, \tag{10}$$

$$h_{z\kappa} = 2i\kappa w_0\omega^{-1}(w_0\epsilon + w)^{-1}, \tag{11}$$

$$h_{\kappa z} = 2iw\kappa\omega^{-1}(w_0\epsilon + w)^{-1}, \tag{12}$$

where all other h_{ij} vanish. The field in equation (6) is the largest, material damage will be highest, and as seen in equations 8-12, perodic solutions exist that are perpendicular and parallel to the laser field, and are dependent, as well, on the angle of incidence of the laser (this angle dependance was never tested in our experiments, but would allow for the ability to modify the grating without adjusting the laser beam properties.)

In order to find a similar solution for our system, we would have to reset the discussion by Sipe with the more complex material susceptibility of titanium and titanium dioxide on a silicon substrate in an air atmosphere. To get an exact solution of the size and strength of the LIPPS requires numerical solutions of the induced field perturbations. What is taken away from this discussion is the physical process that appears to be responsible for our observations. Currently we can control the presence and direction of the LIPPS. With the use of the above theory we can predict how the structure may

behave to thicker films, different substrates, and laser angle of incidence. The next set of experiments in this area should focus on those aspects.

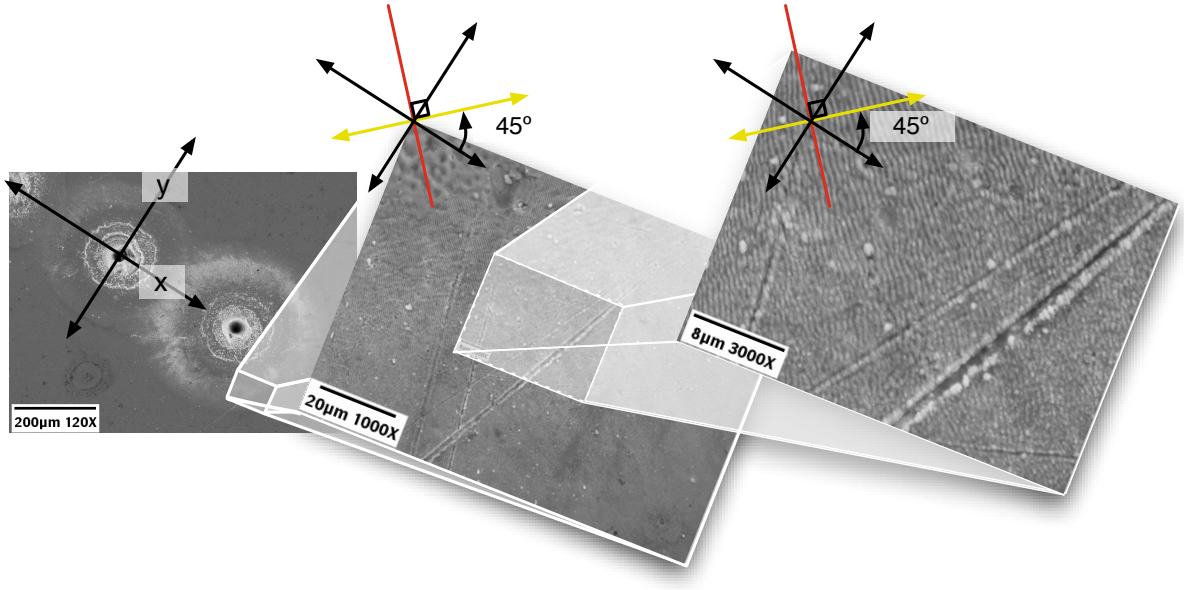

Figure 14: LIPSS pattern created on the outer edge of laser ablation on polished Cu sample. The yellow arrow on the axis was the direction of the laser polarization. The red axis is perpendicular to the laser polarization axis and parallel to the LIPSS pattern.

Lastly, to be assured on what was observed, we decided to duplicate the results reported about LIPSS on bulk metal targets. The targets were polished and exposed to a focused laser pulse. On the edge of the craters drilled by the laser, grating structures were observed, first optically by holographic refection, and later confirmed by the scanning electron microscope. A series of images at increasing magnifications are shown in figure 14. The grating formed in Cu confirmed the results presented by (Young *et al.*, 1983), and ran perpendicular to the laser polarization.

Much work on the laser modifications of thin films remain to be done, but initial results show that we can create and measure new interesting effects. And with current trends in personal computing, medical, and sensing devices, this field is proving to be full of potential applications.

Before moving to the experiments done in liquids and gels, the response of metals to higher power laser pulses has been left open. The author was involved in a series of experiments in the bulk of metals and glasses that are all very well covered in the master's report by Rodrigo Maisterrena-Epstein (Maisterrena-Epstein, 2006), but are not included in this report.

Chapter III

Laser-induced cavitation bubbles in agar gel

Through a UCMEXUS collaboration that existed with UC Riverside and Dr. Guillermo Aguilar and my supervisor Dr. Santiago Camacho-López, the laser microprocessing system started to be used to perform exposures on samples with biological applications. The initial set of experiments were interested in nanosecond laser pulses focused inside of animal tissue; skin and eyes. As a starting point, agar gel was used to mimic properties of animal tissue by mixing in substances to better simulate tissue's optical properties; red colour dye:blood, milk: tissue scattering, agar density: tissue elastic properties. The interaction of the laser and the gel or liquid samples became difficult to understand by only observing the sample after exposure; we had no idea as to how the energy was transfered to the sample and affecting the final results. This work was started by Alejandra Mina-Rosales, Gerardo Romo-Cárdenas, and Francisco Pérez-Gutiérrez. I had assisted in the first experiments, but it was not till the second year, after the publication of the work by A. Mina (Mina-Rosales, 2007), that I began to design and perform experiments. The next three chapters all deal with the basic question of what physical process were taking place when a laser is focused in biological tissues.

III.1 Pump-probe imaging of nanosecond laser-induced cavitation bubbles in agar gel

In this chapter the results of Nd:YAG laser-induced cavitation bubbles formed in a $1mm$ thick agar gel slab are presented. The nine nanosecond duration laser pulses at a wavelength of $532nm$ were tightly focused inside the bulk of the gel sample. With

our pump-probe system we measured the bubble formation and shock wave speed with nanosecond temporal resolution and up to nine seconds temporal range. The shock waves generated by the laser were shown to begin at earlier times within the laser pulse as the pulse energy was increased. After the shock wave was produced and propagated away from the beam focus, a bubble formed and grew at subsonic speeds. The bubble grew to a maximum size related to the laser pulse energy and then quickly collapsed, forming another shock wave and a new bubble. Several oscillations could be observed before the laser-produced bubbles settled to a quasi-stable size that had a linear relation to the maximum bubble size. The energy stored in a bubble is shown to increase nonlinearly with applied laser energy. It was demonstrated that these observations point to the role laser produced plasma had in the production of the observed cavitation bubbles and shock waves.

III.1.1 Motivation

The use of lasers in biological applications has been growing steadly as the technology becomes more stable and afordable. While the laser is not necessarily an efficient method to deliver energy, it is one of the most precise, and can allow for the greatest finesse. The studies that we present here are aimed at the control of laser tissue microprocessing and measuring the secondary effects caused by the use of short pulse lasers; mainly the strong shock waves that are the precursor to the eventual laser-induced bubble expansion.

We use agar gel because it presents a simple tissue phantom. The melting point of agar gel is $80 - 100^{\circ}C$; close to the point of cellular damage in animal tissue (Vogel and Venugopalan, 2003). It has been well documented that a nanosecond laser focused inside of liquids and gels will cause the formation of a bubble (Brujan and Vogel, 2006; Rau *et al.*, 2006). These studies have also presented an analysis of the growth and collapse of the bubble. The study presented here adds to the literature by giving nanosecond time resolution and seconds of range in a single optical setup, allowing for a precise measure of the bubble growth, collapse, and associated shock wave.

Several authors have done experiments with very high numerical apertures up to NA=1.3 (Rau *et al.*, 2004; Vogel *et al.*, 2005); where their target materials were water, liquids or *in vivo*, with laser pulse durations ranging from femtoseconds to nanoseconds. Vogel has done several experiments in gels with focusing angles up to 22° (Brujan and Vogel, 2006). In our experiments we wanted to try and avoid the elongated, and conical plasma region that occurs with weak focusing. We used a focusing lens with an NA greater than 0.5 ($f = 6mm$, beam diameter $= 8mm$.) This lens allowed for tight focusing with an air interface, and a long enough working distance so that the agar could be behind a glass slide; maintaining all interfaces optically smooth, and with the freedom to move the beam focus inside the agar slab. The tight focus of the laser, and working close to the agar's damage threshold implied a small initial diameter plasma to seed the proceeding bubble formation .

The laser produced plasma preceded the bubble in the gel, which continued to grow long after the laser pulse has finished, which implies that the initial conditions set by the laser completely define (along with the material parameters) the life time of the bubble. Several papers have shown, with picosecond resolution (Schaffer *et al.*, 2002), the beginning of bubble formation in liquids and solids, and other papers were forced to rely on simulations and assumptions for the initial hundreds of nanoseconds (Brujan and Vogel, 2006; Vogel and Venugopalan, 2003); Rau had nanosecond to millisecond time scales, but their probe delay was made with fiber delay for short time scales, and changed to an electronically delayed flash for long times. We wanted a simple system that, without changing any optical components, could image the entire lifetime of the bubble. By using an electronically delayed second laser we achieved over nine orders of magnitude of temporal range; the electronic delay had picosecond resolution making the nanosecond pulse duration of the probe beam the limiting factor for temporal resolution.

The drawback of our system was that one exposure could give only one image at a given time delay. However, the repeatability of our experimental results is seen in figure 15 which shows the bubble diameter for varying energies at a $300ns$ delay; each point was a separate exposure on a fresh sample. Other forms of data collection are the use of high speed cameras (limited minimum time delay of 20 μs) (Brujan *et al.*, 2001), beam

deflection methods which trades off spatial resolution for temporal, and thus require multiple exposures to gain spatial information (Gojani and Takayama, 2008; Doukas *et al.*, 1991), and streak cameras which are limited in temporal range (Noack *et al.*, 1998).

This chapter presents the experimental setup, results and finally a brief discussion to both interpret and place into current literature our observations.

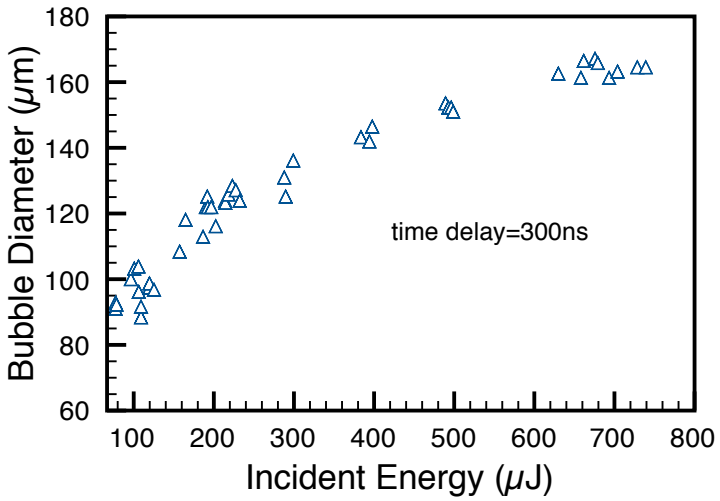

Figure 15: Pulse-pulse repeatability of the experimental system shown by the measured bubble size at 300ns. Each data point was from a fresh exposure site.

III.1.2 Experimental system

Laser sources

Our optical system, figure 16, consisted of two frequency doubled Continuum Minilite, Q-switched Nd:YAG lasers. One of the two lasers had a half-wave plate-polarizer pair to control the power onto the doubling crystal; the laser had been modified to permit the rejected IR beam from the polarizer to be extracted. We used the green 532 nm beam from the unmodified laser as our pump beam, and the IR 1064 nm beam as the probe. Agar gel has a flat absorption spectrum from 500-1400 nm with an absorption coefficient of less than 4 cm^{-1}. The IR probe beam typically had less than 1 μJ of energy per pulse.

The two beams were brought onto the sample in a co-linear geometry. The green pump beam was roughly collimated before it fell onto the 6mm focal length (NA=0.5) aspherical microprocessing lens ($\mu PROC$); the pump beam, which over-filled the lens, was reduced in size by a diaphragm placed before the lens. The IR probe beam was focused by a 35 cm focal length lens ($PROBE$) to a point before the microprocessing lens such that it was collimated as it propagated through the sample. After the sample we used a 25 mm lens (COL) followed by a 40 cm lens (ETP) to image relay the IR beam onto the CCD placed in the transmitted beam line. The image relay was focused for the IR beam, and the green pump was removed with a red (low pass) coloured filter.

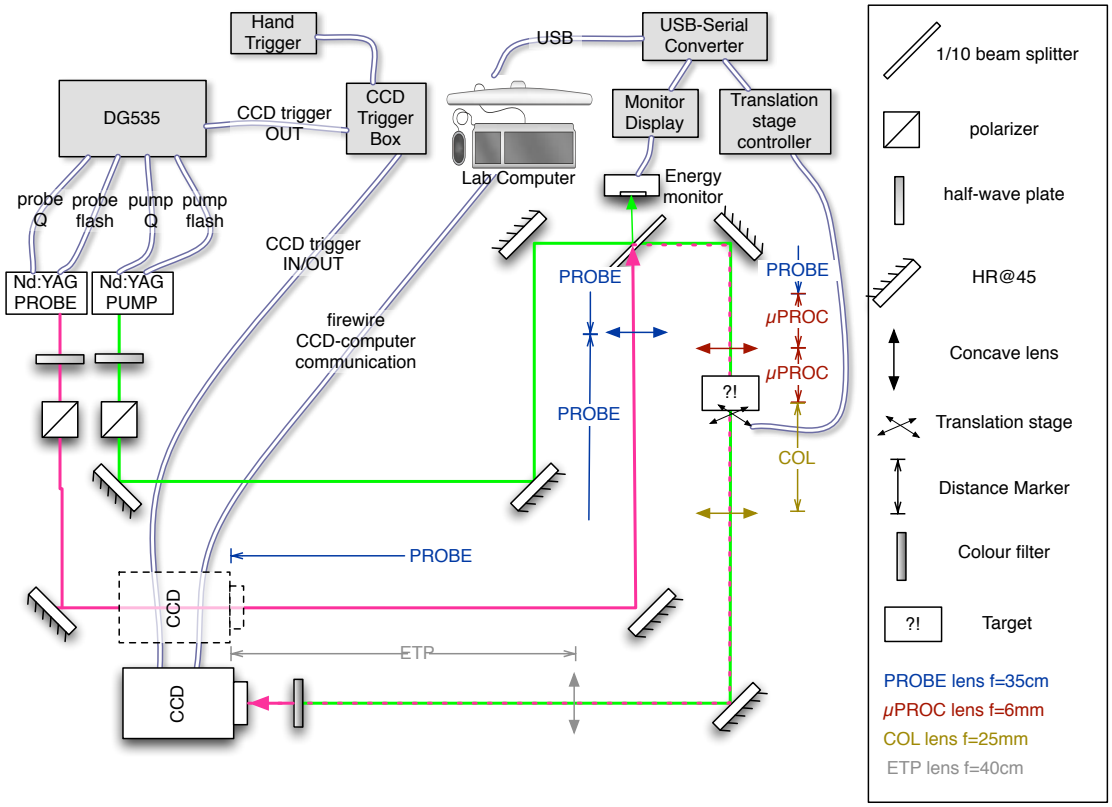

Figure 16: Optical schematic of the microprocessing system. Two Nd:YAG lasers, one of which is frequency doubled, delivered pulses on target with a delay controlled by a DG535. The 532 nm pump beam was focused on target while the 1064 nm beam passed the target collimated. The two locations of the CCD are used to image the sample in transmission and reflection. The system can be triggered by either a hand-held trigger or through the computer; both of which control the CCD which then sent a trigger to the DG535.

The 35 cm lens (*PROBE*) in the IR beam line also served a second purpose. The CCD could be placed to have the pump beam retro-reflected from the target (usually the surfaces of the glass slides in the agar target) onto the CCD in another image relay; this setup is commonly refereed to as an *equivalent target plane* (E.T.P.) system. The E.T.P. was used to set the location of the beam focus in the sample when each new sample was placed in the microprocessing system. The pump beam energy was monitored with a cross-calibrated pyroelectric energy monitor (Ophir) placed on the green reflection of the IR input beam splitter (the calibration was done with a second energy monitor placed after the microprocessing lens ($\mu PROC$); the IR probe beam was filtered out before the energy monitor. The pulse energy was acquired by the energy monitor display, then imported and stored in a computer. The energies measured were exact and not averages.

The pump laser used had a $FW1/e^2M$ pulse duration of $9ns$ and was focused to a beam waist $HW1/e^2M$ radius of $1.3\mu m$; measured with the ETP system. The probe laser passed the sample with a $HW1/e^2M$ radius of 175 μm and a pulse energy close to 1 μJ.

Timing

The timing of the pump to probe delays was controlled with a Stanford Research Instruments DG535 delay generator. The DG535 was triggered by the flash output of the CCD camera which was triggered by either the computer or a hand-held button. The DG535 sent triggers to the flash lamp and Q-switch inputs of both lasers. The pump-probe zero time delay was set with a photodiode placed after the sample holder and read on an oscilloscope; this allowed us to set the zero time delay within 2 ns. The DG535 allowed for delays up to nine seconds with picosecond time resolution. The CCD camera had a shutter time of typically $400ms$, and was set to open about $10ms$ before the arrival of the pump pulse.

Target alignment and preparation

The image relay systems above was used in conjunction with a three axis (x, y, z) computer controlled translation stages; one micron step size. The samples of agar were mixed with a concentration of $1g$ agar powder in $50ml$ of distilled water. Once heated to melting point in a double boiler (to avoid burning) the agar was poured between two microscope slides separated by $1mm$ spacers. The sample was left to cool before placement onto its gimbaled target holder in the microprocessing system. The target holder allowed for adjustment of the surface to beam angle from which we attained a vertical change of less than $50\mu m$ over a horizontal slide of 4 cm. This allowed us to set the beam focus to the center of the $1mm$ thick sample and to take hundreds of data points quickly (less than 20 min) with no overlap or change of focal depth.

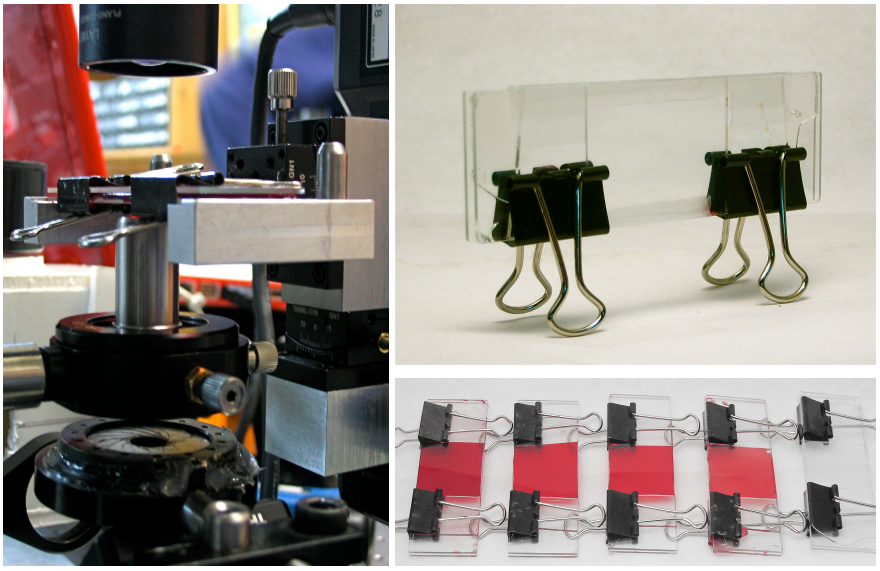

Figure 17: Agar target holder. *left*; agar in microprocessing system, laser was from below, and upper lens captured the image for the CCD. *right* agar sample holders, glass spacer are visible under folder clips. Red colour dye was direct red and is presented in Ch. 4.

III.1.3 Results

The laser was focused in the center of the 1 mm agar sample. One pulse was delivered per site. The time delays were set to observe four distinct regimes of interest;

- 0 to 20 ns : Rapidly slowing plasma expansion and coupling to shock wave
- 20 ns to 100 ns with $\Delta t = 20\ ns$: Linear shock wave propagation
- 200 ns to 1 μs with $\Delta t = 200\ ns$: Bubble maximum size
- 1 μs to 100 μs with $\Delta t = 3\ \mu s$: Bubble collapse
- 100 μs to 1 ms with $\Delta t = 30\ \mu s$: Far field bubble size

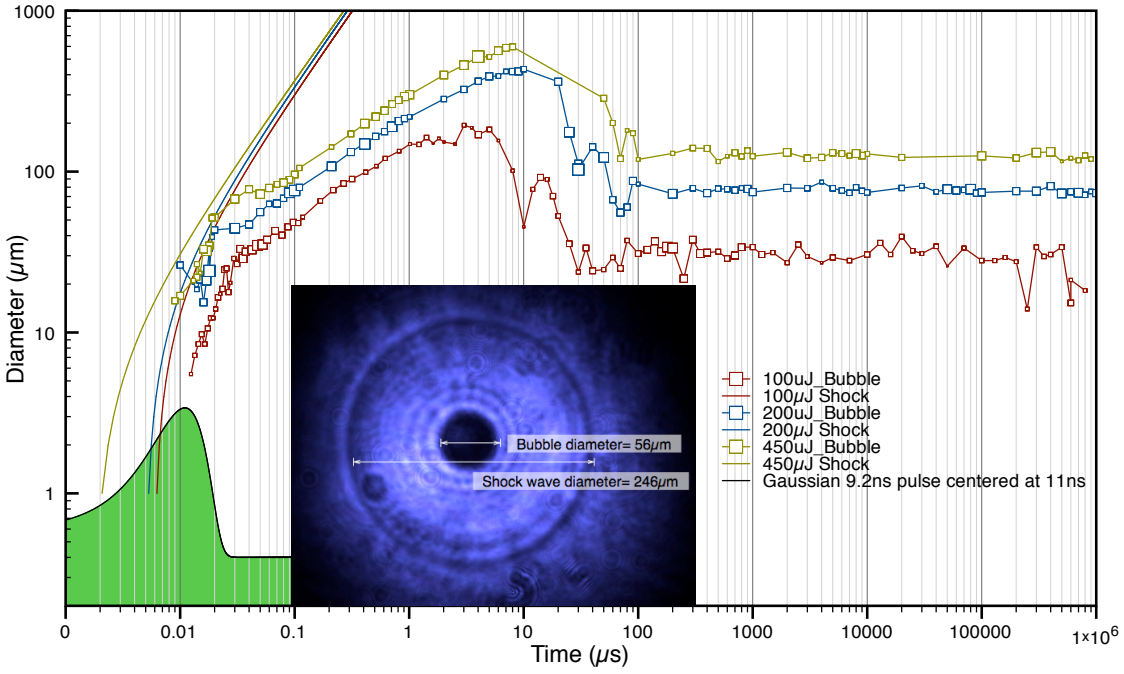

Figure 18: Log-log plot of the formation of a bubble. The shock wave diameters are from linear fits to the measured points; the points are not on the plot to reduce cluttering. The laser pulse drawn is found from a fit to the pulse location as discussed below and shown in figure 20. *Picture insert*; image captured by the CCD camera taken 60 ns after the arrival of a 250 μJ laser pulse into the agar sample. The bubble and shock wave fronts are noted.

Other time delays such as those in figure 18 were used to probe a variety of times; figure 18 displays the results in a log-log plot of the bubble size vs. time for several typical pulse energies. In the example image shown in the insert of figure 18 both the bubble formation and shock wave are visible. The field of view of the CCD camera and the size of the probe beam limit the maximum bubble size that could be measured to be about 450 μm in diameter[1] (data in figure 18 was made with slightly different imaging lens after the sample *(COL)* allowing for a slightly larger field of view.)

Shock wave origin

Rau (Rau *et al.*, 2006) has shown evidence that bubble formation is linked to the presence of laser produced plasma in the focal volume of the laser pulse. Deemed *plasma-mediated ablation*, the topic has been well covered in the area of laser matter interaction and it has recently been applied to medical uses (Niemz *et al.*, 1991). With plasma mediated ablation, the laser light is not directly absorbed by the agar gel, but it's energy is absorbed by a plasma that the pulse created through laser-induced ionization. The laser ionizes the material through a combination of multiphoton absorption, and avalanche ionization (Docchio *et al.*, 1988b; Vogel *et al.*, 1996b). Both of these ionization processes imply the presence of a threshold irradiance above which plasma will form. Plasma has a much higher absorption of laser light than the low absorption agar gel, so the sooner in the laser pulse that threshold irradiance is reached, the proportionally more laser energy the ionized volume will absorb. Laser energy is mainly coupled into the low mass electrons in the plasma and from there into the positive ions; the thermalization of the electrons and ions happens in the order of picoseconds. It has been suggested that it is the hot dense plasma exploding at supersonic speeds into the cold surrounding material that is the source of the shock wave and latter cavitation bubble (Oraevsky *et al.*, 1996; Vogel and Venugopalan, 2003).

If the time for the generation of a shock wave is shorter than the laser pulse producing

[1] A Gaussian beam can be used to illuminate objects greater then its' $FW1/e^2M$ diameter since there is still sufficient light arriving to the CCD to form an image; the imaging software needed its contrast enhanced in some cases.

it, we can look for the time origin of the shock wave and use it to infer when in the laser pulse the plasma was formed. At short times the shock wave front could not be defined in the image. It was not until 10-20 ns after the exposure that a defined shock wave could be extracted. At a delay of 20 ns, the shock wave front expands linearly. This was seen as well by Zysset (Zysset *et al.*, 1989) and was further alluded to by Vogel (Vogel *et al.*, 1996a). Our system could measure the beginning of the shock wave with radii starting close to $20\mu m$ and up to a maximum of $225\mu m$; the first data point was taken at 20 ns, which corresponded to a radius of $40 - 60\mu m$. The shock wave front appeared to travel at a constant velocity. From a linear fit of the shock wave front location, the time origin of the shock was calculated; strictly speaking a shock wave should have been losing energy though shock heating, but a fit of the veloctiy to $1/r^c$ gave a value of $c = 0$. In figure 19 the location of the shock front for varying times and energies is plotted; the insert shows the shock velocity versus the pulse energy.

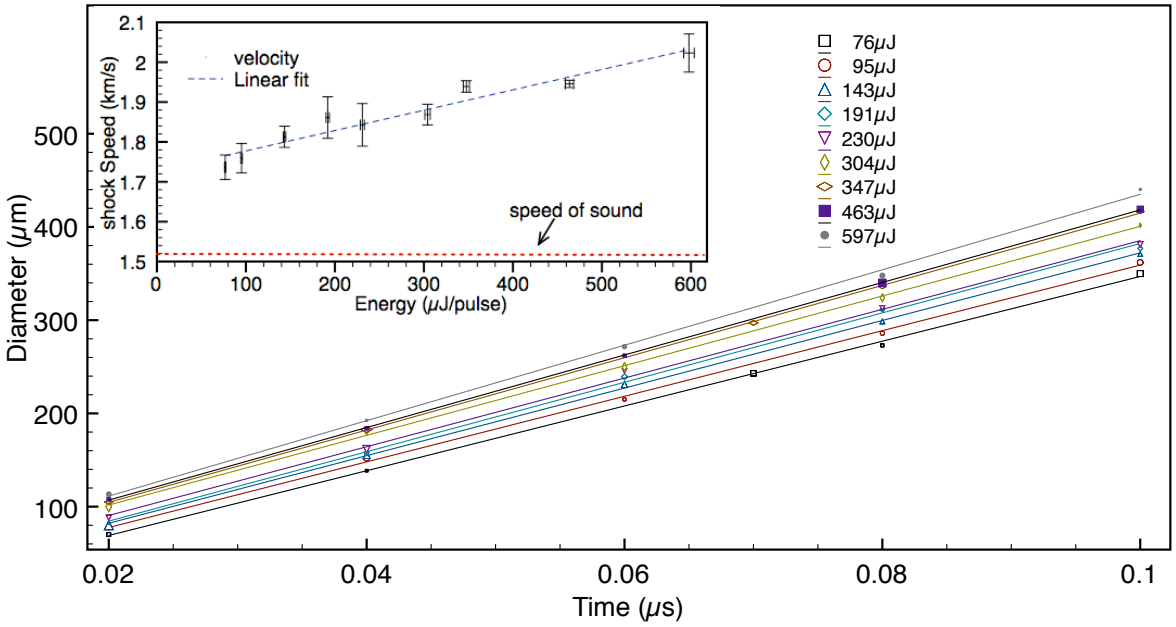

Figure 19: The shock wave front position vs time, Insert: Shock velocity vs. pulse energy extracted from the shock position vs. time linear fit.

Assuming that there was a threshold laser irradiance at which a plasma was formed, a fit of the data gave the probe pulse to pump pulse zero delay and shock wave formation

threshold energy. For a laser pulse with a gaussian temporal profile:

$$I_n(t) = I_{0,n} exp\left[-2\frac{(t_0 - t)^2}{\tau^2}\right]. \tag{13}$$

Each pulse had energy E_n with peak irradiance $I_{0,n}$. According to the above assumption of a plasma threshold, there existed a threshold irradiance $I_{threshold}$ that caused the formation of a plasma. Equation 13 was solved for t_n; the time at which a laser pulse with peak irradiance, I_n, reached the threshold irradiance for plasma formation; $I_n(t_n) = I_{threshold}$:

$$t_n = t_0 - \frac{\tau}{\sqrt{2}}\sqrt{Log\frac{I_{0,n}}{I_{threshold}}}. \tag{14}$$

In a Gaussian pulse shape the total energy and peak irradiance have a linear relation, implying that;

$$\frac{I_{threshold}}{I_{0,n}} = \frac{E_{threshold}}{E_n}. \tag{15}$$

Equation 15 placed into equation 14 gave;

$$t_n = t_0 - \frac{\tau}{\sqrt{2}}\sqrt{Log\frac{E_n}{E_{threshold}}}. \tag{16}$$

Equation 16 was then used as a fit function to the x-intercept found in figure 19 to solve for the location of the probe to pump zero time delay, $t_0 = 11ns$, and the shock wave formation threshold energy $E_{threshold} = 71\ \mu J$; shown in figure 20. Visual observations noted that bubbles were formed for pulse energies above 55 $\mu J/pulse$. A similar phenomenological derivation was performed on laser plasmas by Docchio in his treatment of the moving breakdown model (Docchio *et al.*, 1988a).

Shockwave velocity

An explosion in water or a solid will produce a shock wave. The shock wave leaves at supersonic speeds from the excited region, and carries with it information about the explosion and its resulting pressure differential. The velocity of the shock wave

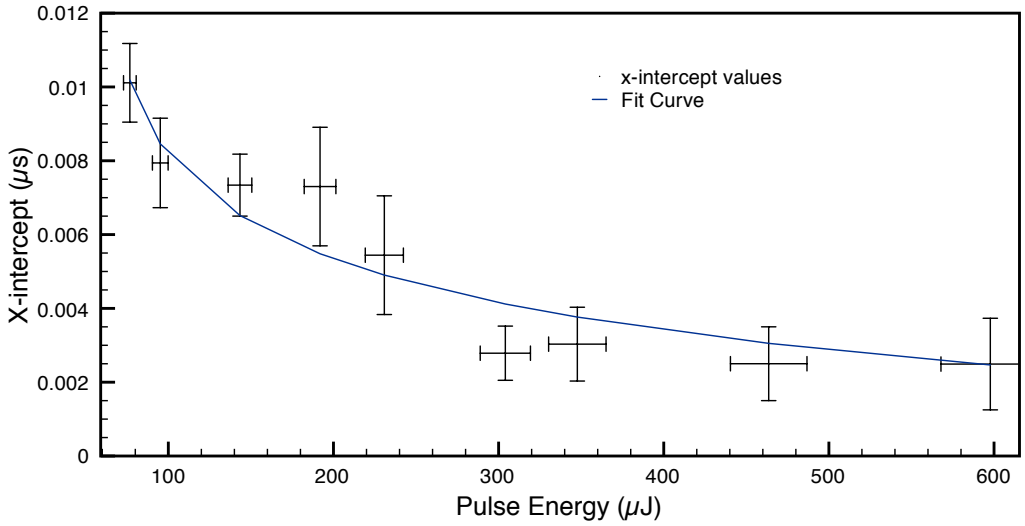

Figure 20: Shock wave positions' x-intercept vs pulse power as found in figure 19 fit to equation 16. The fit gave a shock wave threshold energy of 71 $\mu J/pulse$, and a pump to probe zero delay time of 11 ns.

can be used to determine the pressure difference inside and outside the explosion region. Consider the conservation of momentum equation across the shock wave front where region 1 is inside the shocked region (behind the front) and region 2 is the surrounding unaffected region (in front of the front.) The conservation of momentum and conservation of mass can be stated as;

$$P_1 + \rho_1 u_1^2 = P_2 + \rho_2 u_2^2, \tag{17}$$

and

$$\rho_1 u_1 = \rho_2 u_2, \tag{18}$$

where u_i, ρ_i, and P_i are for region 'i' the velocity of the particles, density, and pressure respectively. If we move the frame of reference to the shock wave moving at speed U, and assuming that the particles in the unaffected region are stationary we can then combine equation 18 and Eqn.17 to get

$$\rho_1 = \frac{U}{U - u_1}\rho_2, \tag{19}$$

$$P_1 - P_2 = \rho_2 U u_1. \tag{20}$$

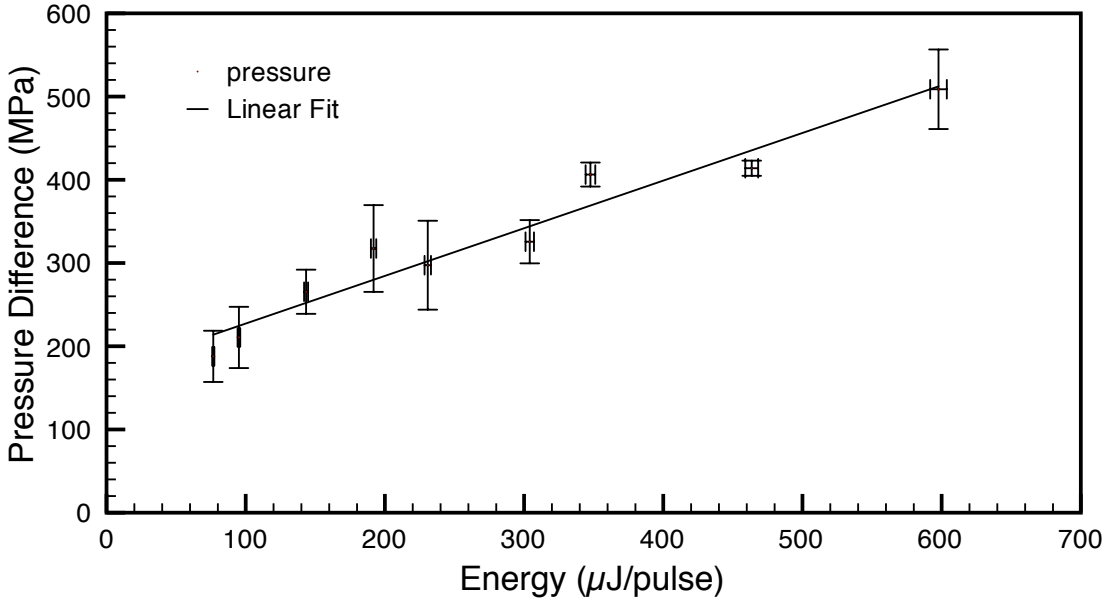

Figure 21: Pressure difference between the shocked and unshocked regions. Pressure was obtained by the shock wave velocity and equation 22

There is still the unknown particle velocity for the shocked region u_i, but for this we can use the Hugoniot equation (Nagayama *et al.*, 2006) to relate the shock velocity, particle velocity and sound velocity C_0 as:

$$U = C_0 + S u_1, \tag{21}$$

where the constant S, and sound speed C_0, in 10% gel were found by Nagayama (Nagayama *et al.*, 2006) to be 2.0 and $1.52 km/s$, respectively. Equation 21 and equation 20 can be combined to give the pressure differential between regions 1 and 2 as a function of the density and the speed of the shock wave propagation:

$$P_1 - P_2 = \rho_2 U \left(\frac{U - C_0}{S} \right). \tag{22}$$

Using the data from figure 19 and equation 22, the pressure difference as a function

of per pulse laser energy can be encountered, and is shown in figure 21 where pressures up to 500 MPa were achieved.

Bubble energy

If the laser produced plasma transfers energy to the cavitation bubble, then an analysis of the energy in the bubble should be able to make comment on the efficiency of this process. The energy in a cavitation bubble was first explored by Lord Rayleigh for an inertially controlled bubble growth, but here the discussion follows publications aimed at laser-induced cavitation bubbles (Rau *et al.*, 2006; Vogel *et al.*, 1996a). The energy in the bubble can be expressed as a function of the maxium radius and the time of the first collapse of the bubble;

$$E_B = \frac{4}{3}\pi\rho\left(\frac{0.915}{T_{col}}\right)^2 R_{max}^5 \tag{23}$$

where E_B is the energy in the bubble, T_{col} is the time for the first collapse, and R_{max} is the maximum bubble radius. These values were measured from data such as that shown in figure 22 which displays several typical bubble evolutions. From the measurements the energy in the bubble was extracted.

In figure 23 the ratio of the energy in the bubble to the energy in the laser pulse is shown. The energy in the bubble reached 0.9% of the laser pulse energy at pulse energies of $300\mu J$. The trend in the plot leads to a zero energy bubble at pulse energies $55\mu J/pulse$ which agrees with the our visual observations of the onset laser-produced plasma, and within error of the fit performed in figure 20. The maximum ratio measured was for energies up to 240 $\mu J/pulse$, limited by the ability to measure the maxium bubble size at high energies. The transmission of the pump laser was also measured and is shown with the energy in the bubble in figure 23, where a drop in transmission corresponds to a rise in the bubble energy. Vogel published an energy absorption up to 76% (Vogel *et al.*, 1996a); this absorption is almost twice the maximum absorption that we measured; scattering of the laser from the plasma was also observed so that the energy absorption would be even lower.

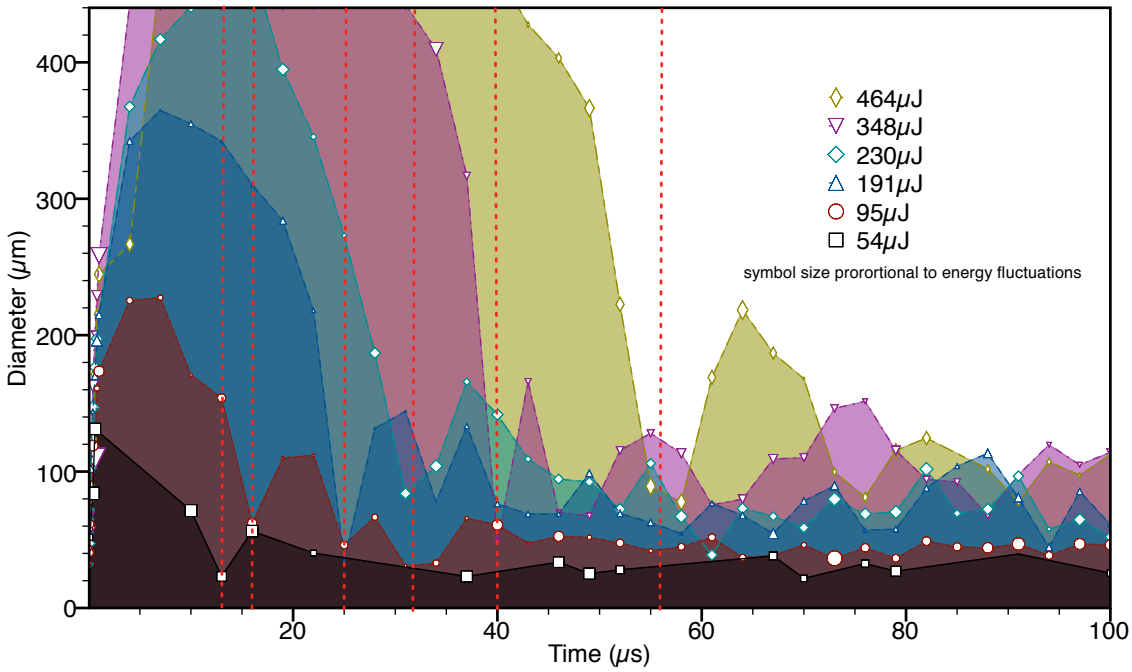

Figure 22: Size evolution of bubbles formed by laser pulses of increasing energy. The time that marks the first collapse of the bubble is noted by a red dotted line. The maximum bubble sizes for per-pulse energies larger than $250\mu J$ were bigger then the CCD-probe-beam field of view.

It should be noted that this is not a complete treatment of the energy in the system as equation 23 uses water coefficients, and does not account for the elastic modulus of the agar. As well, the energy in the shock wave is not accounted for. Determination of these factors is part of ongoing work. It should also be noted that above equation for the bubble energy differs from one used by Vogel (Vogel *et al.*, 1996a), which defined the bubble energy in terms of maximum achieved bubble radius with the vapor and ambient pressure. We used equation 23 because we were able to measure all the parameters it contains (aside from the Hugonoit constants.)

The size of the agar slab used may have affected the bubble growth. It has been shown by Brujan (Brujan *et al.*, 2001) that a rigid boundary does have an effect on the bubble oscillation frequency. If our sample were water, then T_{col} for the larger maximum bubble diameters (above $500\mu m$) could be affected by up to 10%. It is reasonable to assume this as an upper limit for our error in the largest energies used in the agar gel. In our case this error was within the measurement error of T_{col}. In any event, the effect of the rigid glass boundary on the sample was considered a source of systematic error for the larger pulse energies; the more erroneous data for bubble closing time was not used because its' respective R_{max} was too big to be imaged onto the CCD. The transmission and shock wave data were not affected because they happen on a time scale too small for any interaction with the boundary.

Far field bubble size

The bubble diameter varied less than 10% from $100\mu s$ to hundreds of seconds (measured by illumination of the sample with a microscope fiber light that is not shown); we labeled the quasi-stable diameter the *farfield bubble diameter*, and measured it at $1ms$. This size had a near linear relation to the maximum bubble size as seen in figure 24. It should also be noted that the bubble did not always collapse to the same center location, and was seen many times to collapse to the side, but its edge never extended further than the edge of the maximum bubble diameter, and the bubble always retained its proportional size.

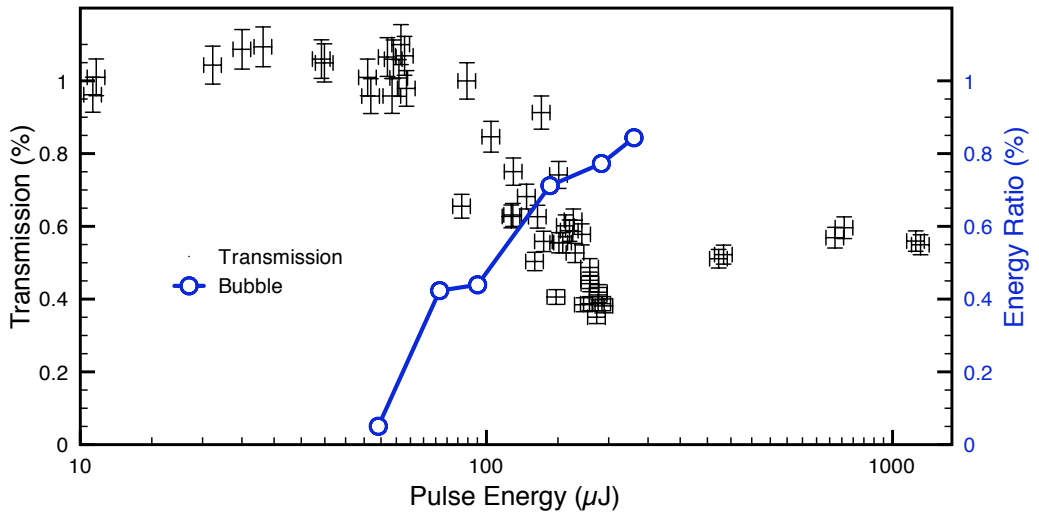

Figure 23: Ratio of energy in the bubble to energy in the laser pulse, and transmission of laser pulse energy. Bubble energy was inferred from equation 23. Energies above $250\mu J/pulse$ formed bubbles whose maximum size was bigger than the field of view of the CCD.

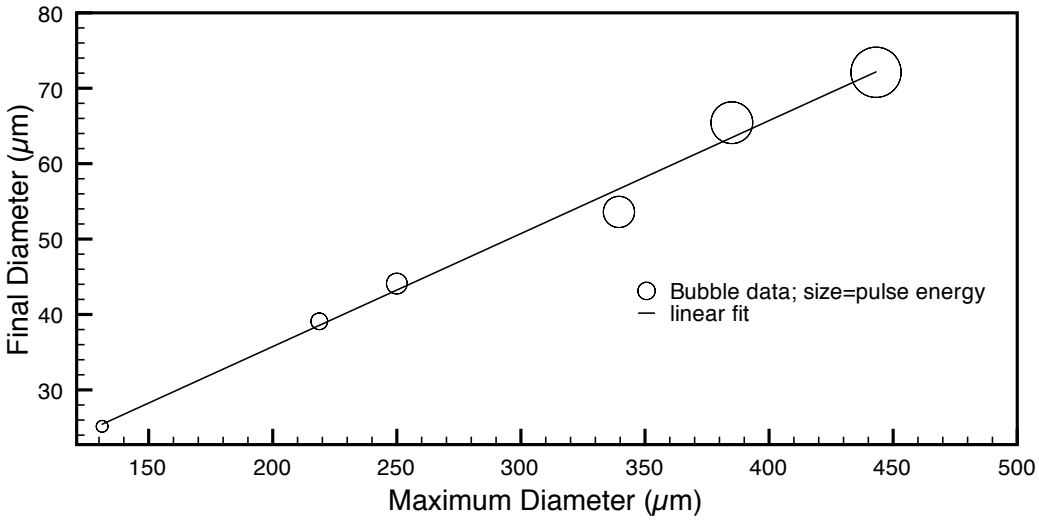

Figure 24: A linear dependance of the bubble size at 1 ms to its' maxium size. The size of the data point is proportional to the per pulse laser energy.

III.1.4 Conclusion: Agar exposures

A pair of Nd:YAG lasers were used, where the pump laser was frequency doubled to $532nm$ and the probe laser was used in the fundamental $1064nm$ for the creation and imaging of laser-induced cavitation bubbles in agar gel. Timing delays were synchronized to a CCD and controlled by a DG535 delay generator. With this system the life cycle of a laser generated bubble in agar gel was shown. The formation of the bubble is marked first by the generation of a shock wave, and then the growth, collapse and formation of quasi-stable (far field) bubble which lasted for more than a second; the maximum and farfield bubble sizes were shown to be linearly related.

The shock wave has been shown to have been generated before the nine nanosecond laser pulse had finished, and originated at earlier times as the laser pulse energy increased. Using a simplified model to associate the shock wave generation time with an irradiance threshold gave an energy threshold for the formation of a shock wave of 71 $\mu J/pulse$. Moreover, the shock wave velocity had been measured and used to find a pressure difference between the shocked and unshocked regions of $200MPa$ at the laser damage threshold, and up to $500MPa$ for $600\mu J$ pulse energies. The pressure appeared to scale with a near linear dependance on the laser pulse energy.

Using equation 23 the energy in the bubble was inferred and an approximate threshold of bubble formation of $55\mu J/pulse$ was determined which corresponded well to other observations. The energy in the bubble increased with increasing energy in the laser pulse, and was consistent with an increased absorption of laser power as seen in the measured transmittance of the laser pulse versus incident energy. There is sufficient evidence to suggest, in conjunction with several above mentioned authors, that the formation of bubbles in agar was a plasma mediated interaction, and that the plasma absorption, and shock wave production were an integral part of the interaction. Our system, because of its high spatial and temporal resolution (nanoseconds and micrometers), allowed us to measure with accuracy the plasma induced shock wave and use this data to model the interaction of laser light with the agar gel tissue-phantom. This was the first time, to our knowledge, that two electronically synchronized lasers have

been used in this type of configuration to measure laser-induced cavitation bubbles and shock waves.

Chapter IV

Linear absorption in laser produced cavitation bubbles

When the experiments with agar were performed, the gelatin was held between two glass slides seperated by a spacer making a slab shaped cavity. The sides of the slab were not of high optical quality so that a laser could be sent through the sample from only one direction. The images taken of the sample were looking down the pump laser beam. This let us observe that the interaction was cylindrically symmetric. Taking an image perpendicular to the pump beam would allow the formulation of a three-dimensional geometry the interaction area. A new mounting system was designed and constructed to make laser exposures inside of liquids, and image the interaction region looking down the focusing laser, or from the side so that the laser was propagating across the image plane and coming to a focus in the center of the image.

Several glass cuvettes with 5 polished surfaces (all but the entrance), were fit into a custom made holder and mounted in the newly rebuilt micro-processing system (mounted cuvette in figure 25.) The following two chapters, while extensions of chapter 3, are based on the work done with the perpendicular imaging configuration.

IV.1 Laser produced bubbles in water with direct red dye

In the following section are the details of experiments of Nd:YAG laser-induced cavitation bubbles in solutions of distilled water and direct red dye; with comparisons made to water-salt and water-salt-glucose solutions commonly used in ocular surgeries. As laser energy was increased, the transmission of the laser through the dye-water solution showed evidence of bleaching at the beam focus. As the per-pulse laser energy increased

further, the threshold for laser induced plasma was achieved, resulting in a lowered laser transmission and the formation of a cavitation bubble. Quick analysis of the exposure images was used to determine the probability for plasma formation. The resulting probability curve's shape was used to determine the pulse energy to give a 50% probability for plasma formation, or the *probable plasma formation threshold* (PPFT). The PPFT was measured for distilled water, and the ocular solutions. The PPFT was measured for various of depth of focus in water with a dye solution. The curves encountered were used to determine the absorption coefficient of the dye as well as the threshold for plasma formation at zero depth (essentially the energy needed to be in the pulse where it came to a focus); this threshold decreases with higher dye concentration. In the exposures of the dye solution in water, where no plasma was created, short lived (less then $1\mu s$) micro-bubbles ($1 - 5\mu m$) were formed in the focal region of the laser; these micro-bubbles were the result of the laser heating of the solution through linear absorption of the dye.

IV.2 Introduction

The previous chapter's work was published as observations of laser produced cavitation bubbles in agar gel using a novel electronically delayed pump-probe (laser flash shadowgraph) imaging system (Evans *et al.*, 2008). It was shown that the bubble formation was plasma-mediated and that the time in the laser pulse when the material became ionized could be determined by using the shock wave launch time. Thus the threshold irradiance required to start ionization was found from the shock wave time origin.

In biological application animal tissues such as skin and eye tissue are diffuse or transparent, but in general have a low linear absorption for green laser light. But, blood present in the tissue is a high linear absorber. The influence of linear absorption on the plasma and formed cavitation bubble is not well understood; thus the motivation for the experiments presented below.

IV.3 Microprocessing system; Experimental setup

To perform experiments in liquids a different target holder was made to place in the beam focus a glass cuvette; figure 25. The cuvette gave us the ability to see the interaction side on. It was not surprising that the on-axis images in the previous chapter displayed circular symmetry, and that fact validates the paraxial approximations that will be employed in the chapter to follow.

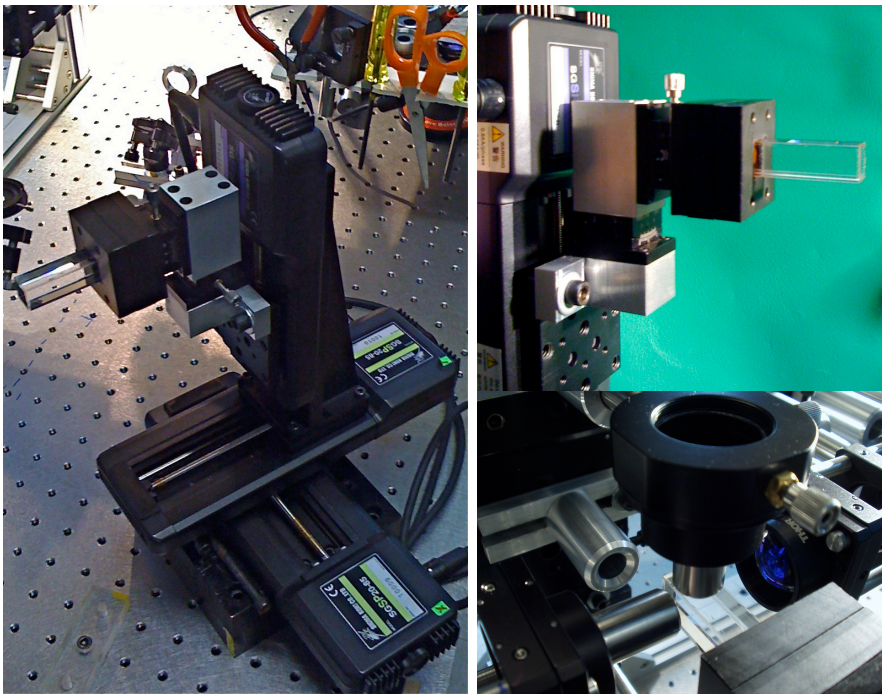

Figure 25: Mounting of glass cuvette target holder. Computer controlled x,y,z, and mechanical θ and ϕ. Bottom right image is the cuvette in place with focusing optics. The pump beam was from above and the probe beam from the left.

Shown in figure 25, the microprocessing system positioned a $1 \times 1 \times 4cm$ glass cuvette with a 2-axis mechanical gimbaled mount, attached to a 3-axis computer-controlled translation stage. As mentioned, the laser configuration could have the probe and pump beam lines on axis with each other, as in (Evans *et al.*, 2008), or crossing perpendicular to one another, as used in the experiment outlined here.

Two frequency doubled (Continuum Minilite,) Q-switched Nd:YAG lasers were used;

the flash lamp and Q-switch of both lasers were controlled directly by a Stanford Research Instruments DG-535 electronic delay generator; the DG-535 was triggered from the flash trigger on the CCD. This gave us picosecond temporal resolution and up to nine seconds of temporal range in pulse to pulse delay.

The laser used for the probe beam was at the fundamental wavelength of $1064nm$ (the beam selected out before the frequency doubling crystal), while the pump beam was frequency doubled to $532nm$. A high reflectivity, zero degree dielectric mirror centered at $535nm$ was placed in front of the CCD to block scattered pump light.

The green laser was chosen for the pump beam because of the high absorption of green light in *direct red* dye; figure 27. The IR light was not absorbed by the dye, so that less than $1\mu J/pulse$ gave a bright image on the CCD.

The probe beam was sent through the sample collimated, then image relayed onto the imaging CCD; this configuration was used so that the probe beam would be passing the same optics for both the parallel and perpendicular imaging systems. The pump beam was focusing and probe beam collimation were done with a 6mm aspherical lens ($N.A. = 0.5$). To find the location of the beam focus we used a retro-reflected image relay system; equivalent target plane (ETP.) This allowed us to locate the focal plane to within $2\mu m$.

IV.4 Plasma formation threshold

When an intense laser pulse is tightly focused inside a material, the electromagnetic field is strong enough to cause ionization of the material forming a plasma; the plasma is a strong absorber of the laser light leading to more energy coupling into the material (Noack and Vogel, 1999). Energy is deposited into the material within the duration of the laser pulse (typically $4-10ns$.) The energized region, surrounded by cold material, violently expands, emitting a shock wave, and causing an oscillating cavitation bubble (Evans *et al.*, 2008).

There are two main mechanisms primarily responsible for the ionization of a medium with very low linear absorption at the laser wavelength; multiphoton absorption, and

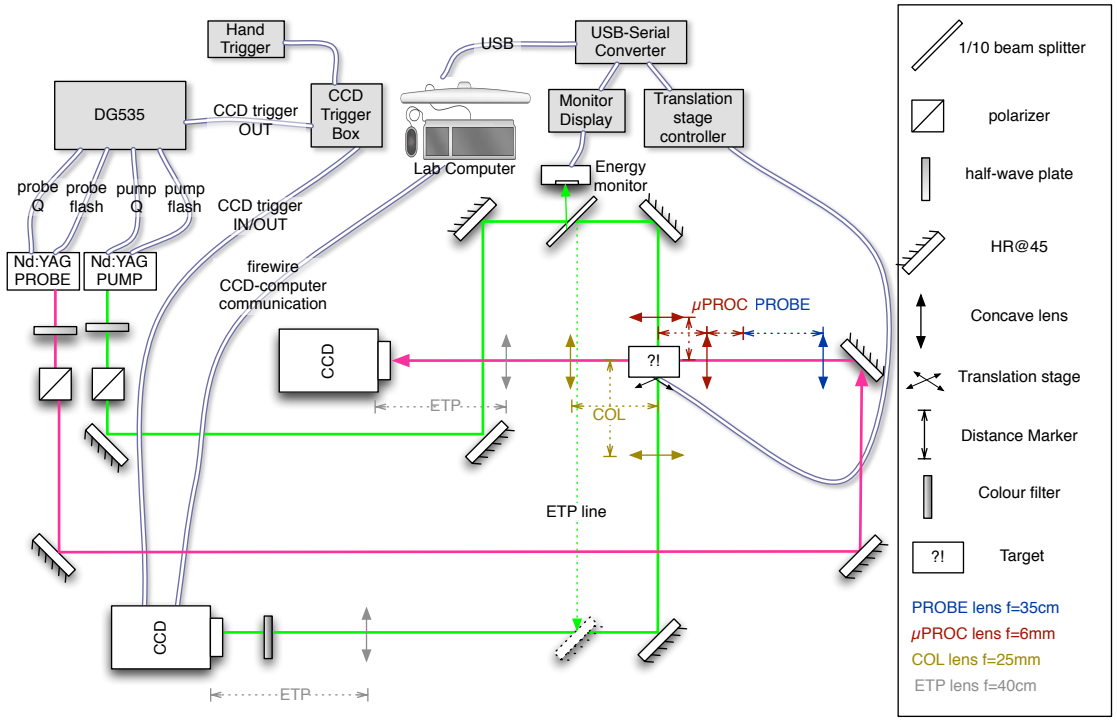

Figure 26: Microprocessing system; side looking, with pump and probe beam perpendicular to one another.

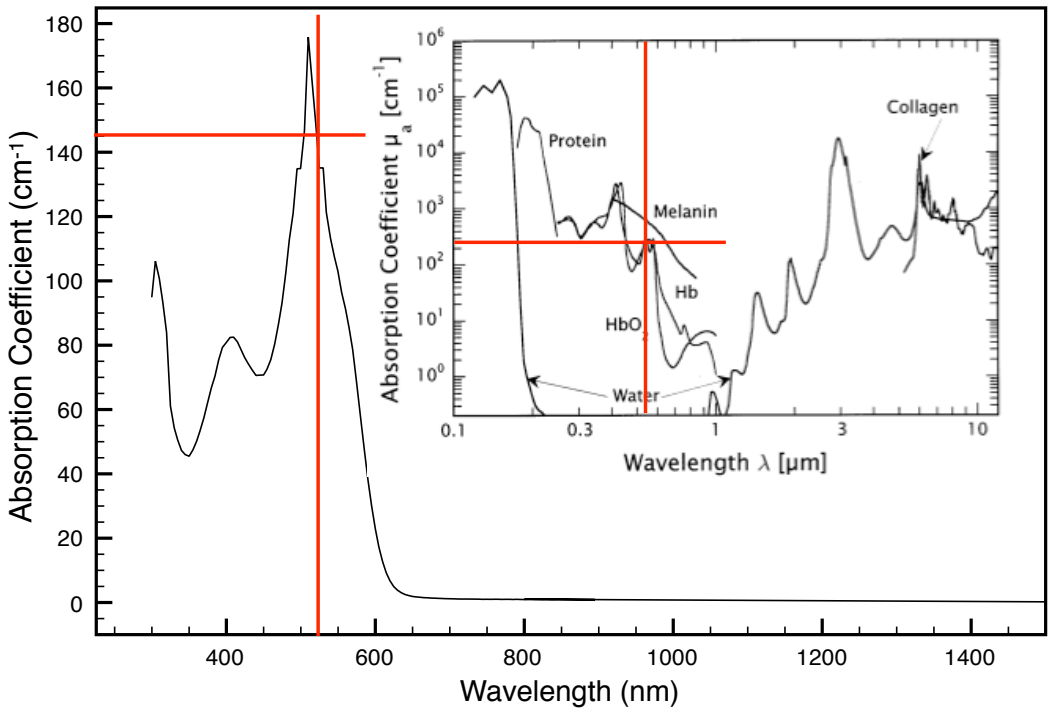

Figure 27: Absorption spectrum of *direct red* colour dye. Spectrum was obtained with a 10% dye concentration with agar gel; the agar spectrum was subtracted to give just the dye spectrum. The insert spectrum is of hemoglobin in human blood taken from (Vogel and Venugopalan, 2003). The red lines mark the same absorption and wavelength in both spectrums.

avalanche ionization. Avalanche ionization requires the presence of free electrons to act as seeds that absorb light energy, and while being accelerated by the applied electric field collide with neighboring molecules which cause the release of more free electrons. The seed electrons for avalanche ionization are generated through multiphoton ionization. To find the number of photons needed to ionize, water can be treated as an amorphous semiconductor (Noack and Vogel, 1999) with a bandgap of $\Delta E = 6.5eV$. For $532nm$ laser beam in distilled water, up to three photons are needed to lift an electron into the conduction band.

The threshold mentioned above is the lowest energy for plasma formation, but defects, impurities, and density flucuations all affect strongly the probability for electron production.[1] As the laser energy increases the probability that a plasma will be formed follows a Gaussian error function. The percentage of laser pulses that produced plasma can be plotted versus the per-pulse laser energy. The resulting curve resembles a rounded heavy-side function going from zero to one. By plotting the derivative of this curve and fitting to a standard Gaussian distribution, the energy at which the laser has a 50% probability of producing a plasma corresponds to the center of the Gaussian fit. This energy, the probable plasma formation threshold (PPFT), is not the same as what most authors call the damage threshold. The damage threshold is commonly referred to as the minimun energy needed to make a plasma. The PPFT is used here because measuring the percentage of times that a laser beam generates a plasma can be automated, and so can finding the point in the center of a distribution. Where as the minimum energy to ionize is in the tail of the distribution, so is not a well defined measurement.

IV.5 Results and Discussion

IV.5.1 PPFT to find dye linear absorption

The glass cuvette was filled with distilled water and up to one thousand separate exposures at varying energies were performed taking images of the focal region with the

[1] In chapter 2, the spikes on the nano-craters rims acted as absorption centers because of the focusing of the electric field

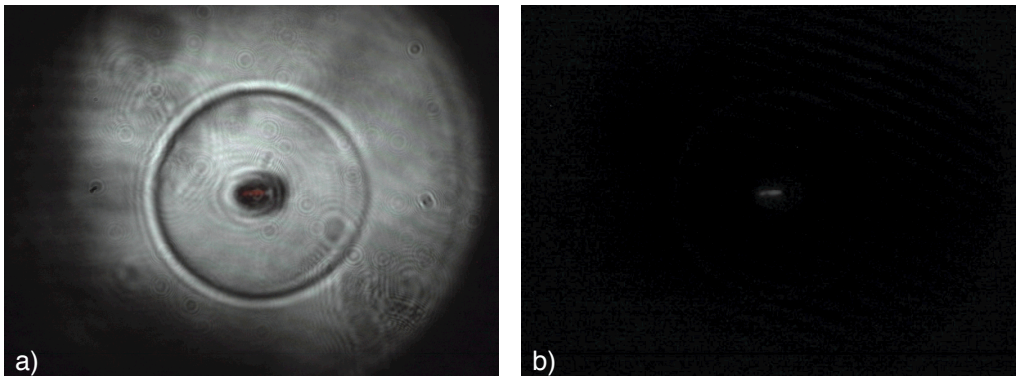

Figure 28: Images of cavitation bubble taken with the probe pulse arrival $100ns$ after the pump laser pulse delivery. a) IR probe beam and plasma (RGB), b) greyscale image of the value of the blue pixels subtracted from the red value (R-B).

low energy IR probe beam as the illumination source. The images of the focal region captured both the IR probe beam, seen as white on the colour CCD, and the plasma, seen as red. To obtain images of just the plasma a program was written in MatLab that subtracted the blue pixel values from the red values, leaving just the image of the plasma; see figure 28. The green pixels also did no see any plasma, but the use of a dielectric mirror centered at $532nm$ as a green filter, implied that the green signal would more complicated to use for photometry; the IR beam had over a 95% transmission of the optic. The program then summed the pixel values in the region of the plasma, and could determine the existence of the plasma in the image. This process was used to obtain the PPFT for distilled water at $400\mu J/pulse$.

'Direct red' dye was added to the distilled water in two different concentrations, $1\mu g$ and $10\mu g$ dye into $20mg$ distilled water. At several distinct energies, images of the focal region were taken at varying depths of focus. The dye attenuated the laser energy so that the depth scan functioned as an energy scan. The decrease in energy in the beam as a function of depth is found through the Beer-Lambert law to be;

$$E(z) = E_{in}e^{-\alpha z}. \tag{24}$$

At the depth z_i the energy transmitted is $E_i = E_{in}e^{-\alpha z_i}$.

If the assumption is made that I_{ppft} is the irradiance necessary for plasma formation, then by finding the depth z_i at which energy $E_{in,i}e^{-\alpha z_i} = E_{ppft}$, ($E_{ppft}$ is the energy in the pulse the give a peak irradiance of I_{ppft}) the breakdown energy E_{ppft}, is found to be;

$$E_{in,i} = e^{\alpha z_i} E_{ppft}. \tag{25}$$

E_{ppft} is also thought of as the PPFT at zero depth in side the water with dye. The values of $\{E_{in,i}, z_i\}$ are found in figure 29. In figure 30 the values $E_{in,i}$ versus z_i are fit to equation 25 where the PPFT at a zero depth E_{ppft}, and the absorption coefficient α, can be determined. Resulting, the PPFT at zero depth for the dye concentrations of $1\mu g/20mL$ and $10\mu g/20mL$ were $147\mu J/pulse$ and $86\mu J/pulse$ respectively. The propagation of an unfocused beam through the sample was also used to measure the absorption coefficient. The absorption coefficient from the fit matched values measured by the unfocused laser beam propagating through the sample. Interestingly, the breakdown intensity appeared to have decreased with an increase in dye concentration.

IV.5.2 Transmission; nonlinear absorption and dye saturation

The response of the dye to the laser was observed by measuring the transmission of the laser through the dye as a function of input energy. Placing a photodiode after the sample and determining the area under the curve of the detected signal, gave values relative to the transmitted laser energy; the transmission of distilled water at the lowest energy was used as the normalization value. Figure 31 displays the transmission of both distilled water, and distilled water with dye in solution ($\alpha = 3.8cm^{-1}$). Because of the ability to image plasma formation, we were able to show the transmission with and without plasma; automatic filtering of data has not been published for these type of interactions. The decrease of transmission in distilled water as energy increases is similar to work presented by (Nahen and Vogel, 1996) but their measured transmission of the plasma created by a $6ns$ pulse was much lower than what we measured; our transmission curve is similar to the $30ps$ pulses of Nahen. Possibly it is the tighter focusing of our laser causing the difference between our transmission and that measured by Nahen and

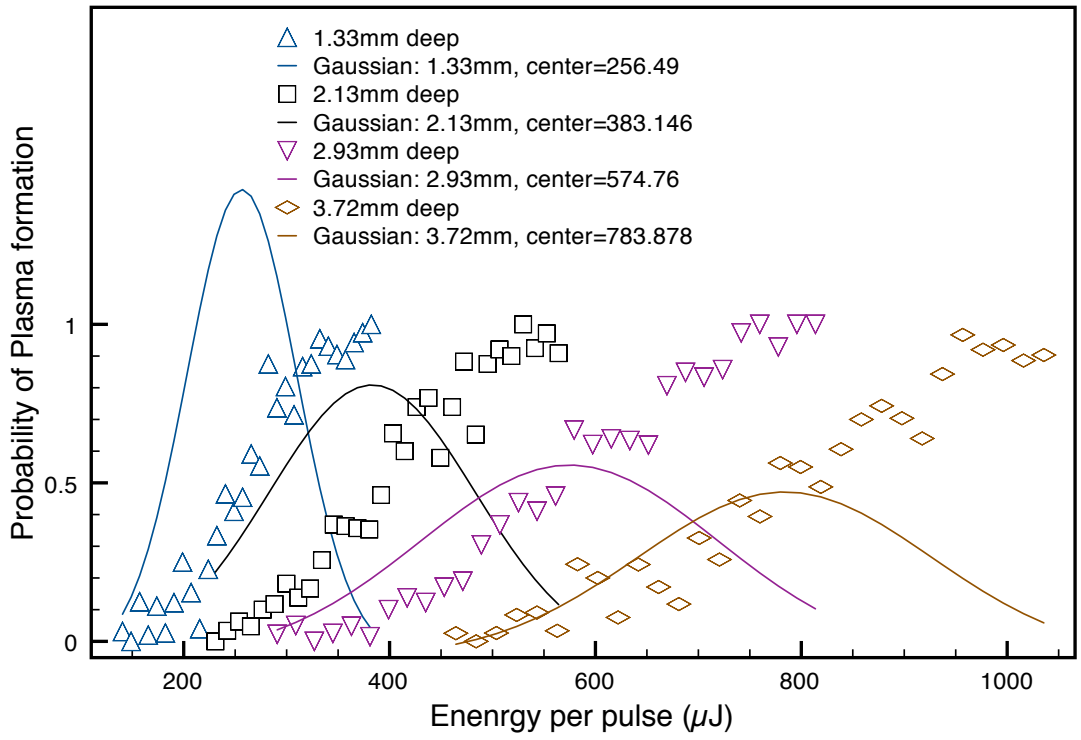

Figure 29: Normalized probability for the formation of plasma at given energy and at several depths. The Gaussians curves are the fits to the derivatives of the measured probabilities.

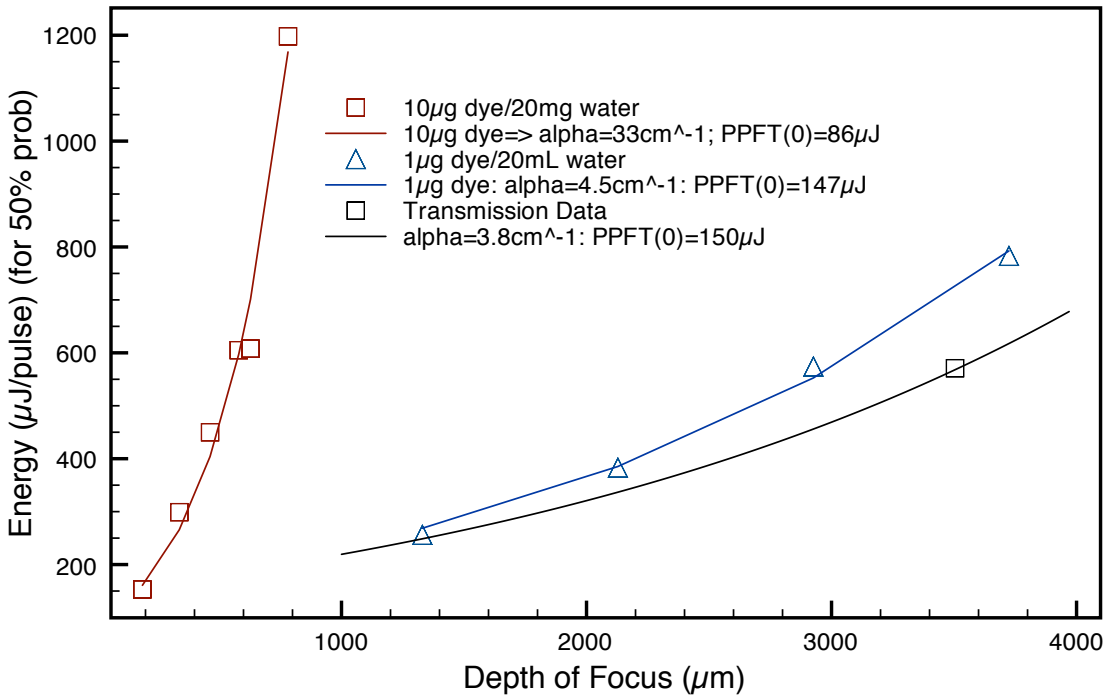

Figure 30: Plot of the energy per pulse to acheive 50% plasma formation fit to equation 25. The single point in black was the concentration used in the transmission experiments shown in figure 31

Vogel. The images of the laser induced plasma we observed was of a filament of plasma growing down the optic-axis which is contrasted to a cone of plasma growing up the optics axis (Nahen and Vogel, 1996).

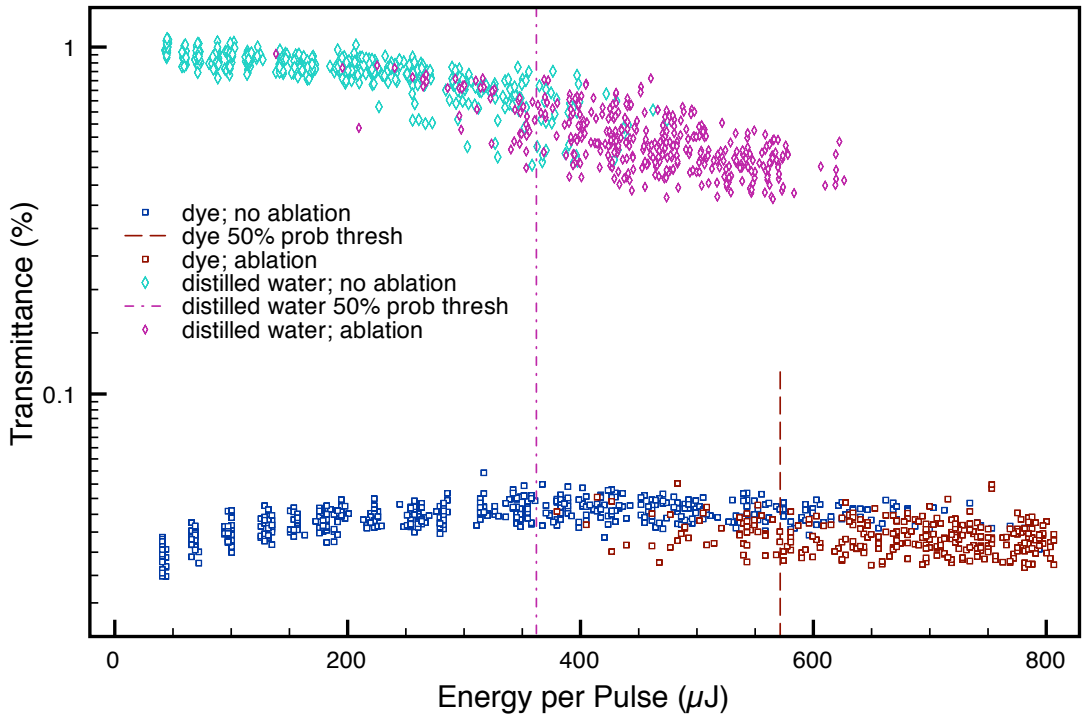

Figure 31: Transmittance of the pump laser for distilled water, and distilled water with dye concentration whose transmission at low energy had an $\alpha_{dye} = 3.55cm^{-1}$. The values for transmission with and without plasma are shown.

The decrease in the transmission in the water can be accounted for by the nonlinear absorption of the water. The source of the absorption is the material polarization which can written as a power expansion of the electric field as;

$$\bar{P} = \bar{P}_0 + \epsilon_0\chi^{(1)}\bar{E} + \epsilon_0\chi^{(2)}\bar{E}\bar{E} + \epsilon_0\chi^{(3)}\bar{E}\bar{E}\bar{E} + \ldots, \tag{26}$$

where we are interested in the third order component of this field $\bar{P}_{NL} = \epsilon_0\chi^{(3)}|E|^2\bar{E}$. Taking the electric field as a typical electromagnetic wave with wave number k;

$$\bar{E}(r,t) = \frac{1}{2}\left(\mathcal{E}(\bar{r},t)e^{i(kz-\omega t)} + c.c.\right), \tag{27}$$

and combining Maxwell's equation with the material response gives a wave equation, (Rangel-Rojo, 2004);

$$\nabla^2 \bar{E}(\bar{r},t) - \frac{n_0^2}{c^2}\frac{\partial^2 \bar{E}}{\partial t^2}(\bar{r},t) = \mu_0 \frac{\partial^2 \bar{P}}{\partial t^2}(\bar{r},t). \tag{28}$$

Using equation 27 in equation 28, with the slowly varying wave approximation ($\omega\frac{\partial \epsilon}{\partial t} \ll \omega^2|\mathcal{E}|$), the evolution of the electric field as it propagates into the sample is found to be;

$$\frac{\partial \mathcal{E}}{\partial z} = \frac{\alpha}{2}\mathcal{E} + i\,\chi^{(3)}|\mathcal{E}|^2\mathcal{E}. \tag{29}$$

The electric field $\mathcal{E}$ can be represented by a vector and phase by $\mathcal{E} = \bar{A}e^{i\phi}$, and this can be placed into equation 29, where the real and imaginary parts can be written separately as;

$$\frac{\partial \bar{A}}{\partial z} = \frac{\alpha \bar{A}}{2} - \frac{\omega}{2cn} Im\chi^{(3)} A^3, \tag{30}$$

$$\bar{A}\frac{\partial \phi}{\partial z} = \frac{\omega}{2cn} Re\chi^{(3)} \bar{A}^3. \tag{31}$$

Taking the imaginary solution, the equation for the irradianced can be written as;

$$\frac{dI}{dz} = -\alpha I - \frac{2k}{n^3\epsilon_0 c} Im\chi^{(3)} I^2 \tag{32}$$

$$= -I\left(\alpha + \beta I\right). \tag{33}$$

Equation 33 can be integrated to give the solution for the intensity as the beam propagates through the sample as;

$$I(z=L) = \frac{I_0 e^{-\alpha L}}{1 + \beta I_0 L_{eff}}, \tag{34}$$

where $L_{eff} = \frac{1-e^{-\alpha L}}{\alpha}$. To measure the value of the nonlinear absorption in water equation 34 can be used by plotting the inverse of the transmission, $1/T = \frac{I_0}{I(z=L)}$ versus the input intensity I_0. If a straight line is formed, its slope is equal to $\beta L_{eff} e^{\alpha L}$.

This fit is shown in figure 32 where both sides of equation 34 have been multiplied by the spot area to give the equation for $1/T$:

$$\frac{1}{T}(z = L) = e^{\alpha L}(1 + \beta I_0 L_{eff}). \tag{35}$$

The total energy in a Gaussian beam in both space and time is related to the peak energy;

$$E = \int_0^{\infty}\int_{-\infty}^{\infty} I(r,t)drdt = I_0 \int_{-\infty}^{+\infty} e^{-2\left(\frac{t}{\tau}\right)^2} dt \int_0^{\infty} 2\pi r e^{-2\left(\frac{r}{w}\right)^2} dr = I_0 \frac{w^2}{4}\frac{\tau}{2}\sqrt{\frac{\pi}{2}}, \tag{36}$$

where the slope of $1/T$ versus E_0 is equal to $\beta L_{eff} e^{\alpha L}$. The value of L_{eff} is dependant on the length of propagation in the nonlinear material. Since our beam was focusing the interaction region was simplified to be a uniform intensity distribution inside of a clyinder as long as the raleigh range, a radius the size of the $1/e^2$ beam waist, and a constant irradiance chosen to be just over the irradiance at the $1/e^2$ radius; $I = I_0 \times 0.14$. The Raleigh range for a Gaussian beam is $z_R = \frac{\pi w_0^2 M^2}{\lambda}$, where w is the beam waist size, and λ the wavelength. The nonlinear absorption measured for water was found to be $\beta_w = 2.3 \times 10^{-14} \frac{cm^2}{W}$, agreeing well with published data (Vogel *et al.*, 1996b; Boyd, 2003).

The linear dye can become saturated if the light irradiance exceeds a threshold value. The absorption coefficient for a saturable absorber can be written as;

$$\alpha_{dye}(I) = \frac{\alpha_{dye}}{1 + I/I_s}. \tag{37}$$

Equation 34 can then be modified to model water with dye by setting $\alpha = \alpha_{water} + \alpha_{dye}(I)$ and $\beta = \beta_{water} + \beta_{dye}$. The saturation irradiance in the dye's linear absorption now becomes a problem. To resolve this analytical problem a computation model was devised to solve the system numerically. Figure 33 shows the idea behind the model. The main concept is to separate the focusing beam into a series of slices, where the irradiance through each slice is considered a constant value that is related to the peak irradiance and laser spot size. The energy in and out of each face of the slice is found

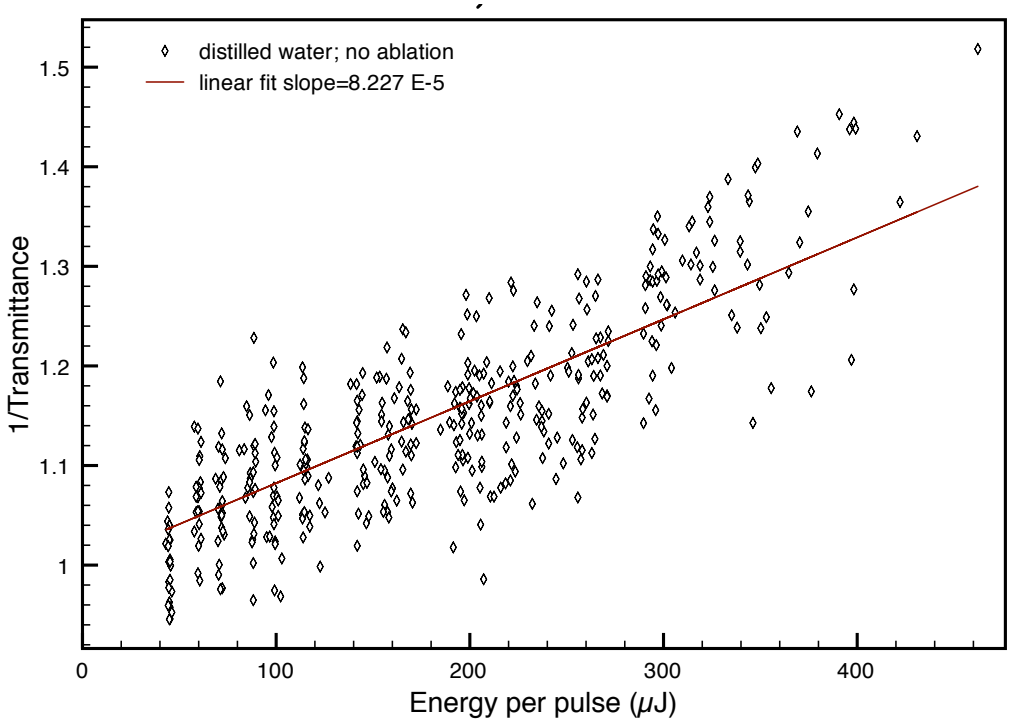

Figure 32: 1/transmittance for distilled water. The slope of the line gives the nonlinear absorption of water as $\beta_{water} = 2.3 \times 10^{-14} \frac{cm^2}{W}$

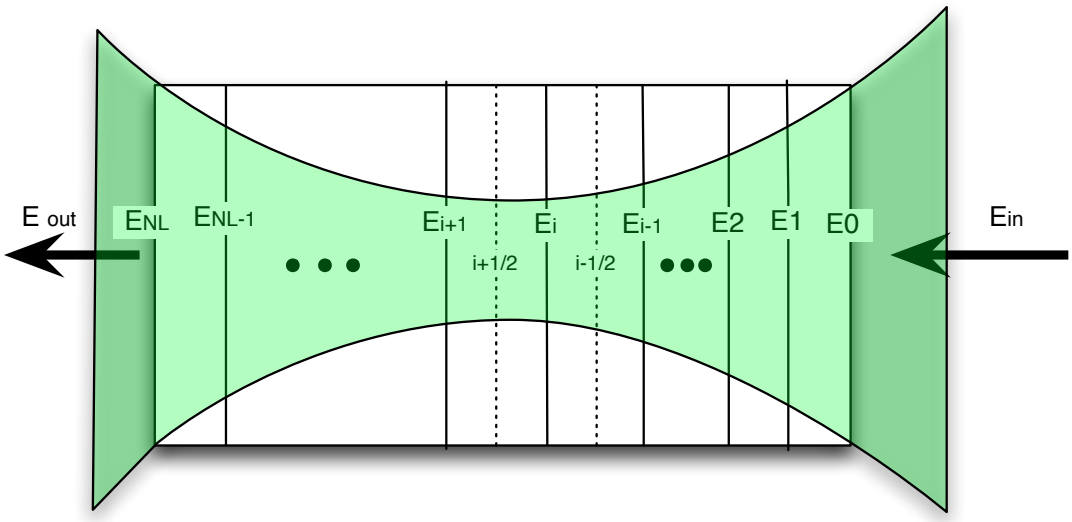

Figure 33: Schematic of computer model used to simulate absorption of laser light for a focusing beam

using the energy entering the input face, with the spot size at the half-way location of the slice; mathematically;

$$E_i = \frac{E_{i-1}e^{-\delta z \alpha_{tot}}}{1 + \beta_{tot} L_{eff} I_{i-1/2}}, \tag{38}$$

$$I_{i-\frac{1}{2}} = \frac{8E_{i-1}}{\sqrt{\frac{\pi}{2}}\tau \left\{w\left[(i-\frac{1}{2})\Delta z\right]\right\}^2}. \tag{39}$$

The values used were $\beta_{water} = 2.3 \times 10^{-14} \frac{cm^{-1}}{W}$, $\alpha_{water} = 3.0 \times 10^{-4} cm^{-1}$ (Hale and Querry, 1973), and $\alpha_{dye} = 3.8 cm^{-1}$ as measured in figure 30. The simulation was run to duplicate the experiment shown in figure 31. The values of I_s and β_{dye} were adjusted to fit the measured experimental data. The final values to give the fit in figure 34 were $\beta_{dye} = 2.7 \times 10^{-14} \frac{cm^{-1}}{W}$ and $I_s = 4.9 \times 10^7 \frac{W}{cm^2}$

It is important to note the relevance of the nonlinear absorption of the dye as it would be impossible to fit the simulation output to the experimental data for the transmission of water, and transmission of water with dye, without the contribution of the dye to the nonlinear absorption. This is to say, that while the linear absorption of the dye is saturated, the nonlinear absorption plays a dominant role. The linear absorption of the dye can be seen to be saturated for the region of the beam focus by $400 \mu J/pulse$. At this point the gain in transmission from saturated dye is compensated as the increase in nonlinear absorption begins to reduce the transmission of the sample.

To observe better the difference between the linear and nonlinear absorption in the water with dye, figure 35 is presented. The upper three images show the interaction region for the first three nanoseconds of the pump laser pulse. The blue lines were drawn afterward, and are the $1/e^2$ radius of the beam. The green in the focus has a linear relation to the calculated irradiance of the beam; irradiance= I_0 implies a green value= 255. The lower rows show the sample at later times with and without plasma production. In both cases the laser beam path was seen by a change in the IR probe propagation (most likely due to a change in the index of refraction). The plasma production correspond to the formation of a bubble, while the images without plasma production show the formation of micro-bubbles in the beam focal region from $30ns$

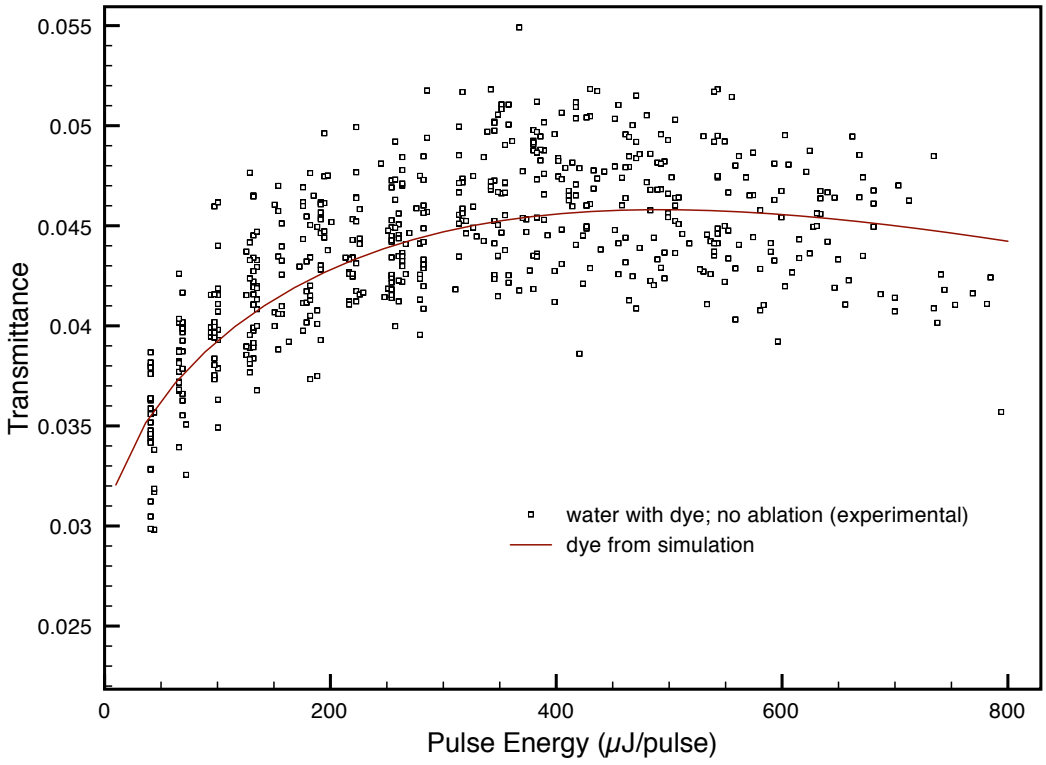

Figure 34: Transmittance of pump laser through dye with $\alpha_{dye} = 35.5cm^{-1}$; experimental data are the points and the line is the output of the computer model.

till $3000ns$. The micro-bubbles were observed for pulse energies below the threshold for plasma formation.

IV.5.3 PPFT of ocular fluids

It was hypothesized that the lowered PPFT measured in the dye-water solution was due to the formation of impurities that increased with the dye concentration in water. This implies that an increase in dye concentration will lead to a decrease in PPFT. In this experiment we used two different solutions commonly used in laser eye surgeries; *Ocular irrigation fluid*, 100mL of fluid contained $0.640g$ sodium chloride, 0.075 potassium chloride, $0.048g$ calcium chloride (as the most abundant additives), and *Solucion DX-CS*, an injectable ocular fluid with $100mL$ of water contained $5.0g$ of glucose, and $0.9g$ sodium chloride. Both of the ocular solutions are clear, colourless liquids. If the hypothesis is correct, then this implies that the ocular concentrations should show a decrease in the PPFT from measurements made in pure water, even though the linear absorption of the fluid has not changed.

The laser was focused $3.6mm$ into the cuvette for samples of distilled water, distilled water with $1\mu g$ of direct red dye per $20mg$ of water ($\alpha = 3.8cm^{-1}$), ocular irrigation fluid, and Sol DX (injectable ocular fluid). The PPFT of all the fluids were found, as shown in figure 36. The ocular solutions both measured a PPFT of $295\mu J/pulse$ as opposed to a PPFT of $362\mu J/pulse$ for pure distilled water. The important point to note is that a solution of water and salts causes a lowering of the PPFT, which gives weight to the idea that the addition of dye to water lowers the PPFT of the water, regardless of the linear absorption of the dye.

IV.6 Conclusion

It is obvious that the presence of plasma is necessary for the production of a laser produced cavitation bubble. In distilled water, which is effectively transparent to the $\lambda = 532nm$ wavelength laser light used, the nonlinear absorption can be determined by measuring the transmission of a focused laser pulse. Through the use of several

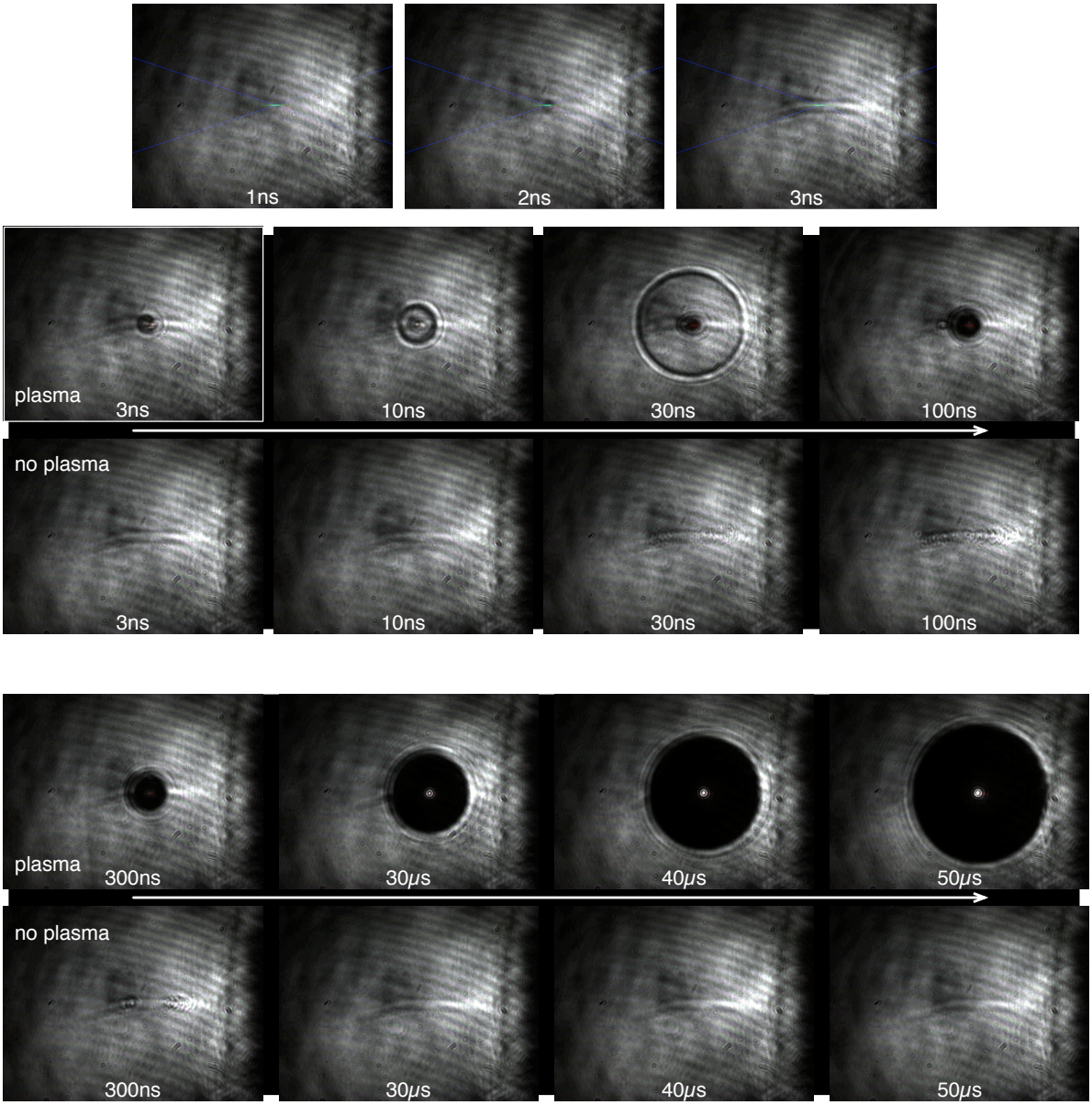

Figure 35: Images of laser exposure in water with dye. Bottom rows show the interaction region with and without the presence of plasma.

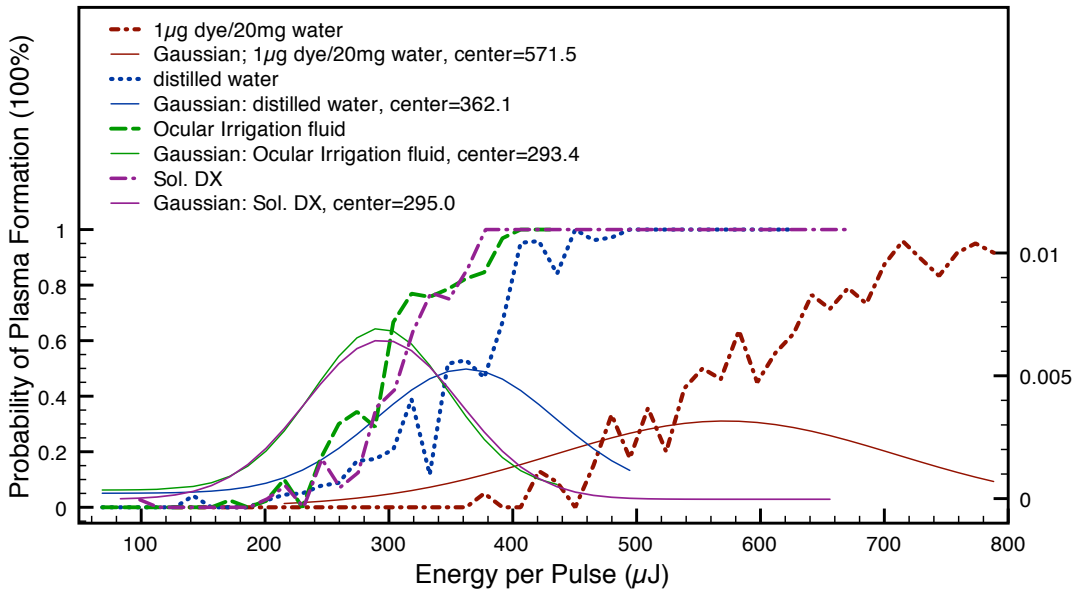

Figure 36: Probability of plasma formation for distilled water, direct red dye with ($\alpha = 3.8cm^{-1}$), ocular irrigation fluid, and Sol DX (injectable ocular fluid).

approximations the nonlinear absorption of water was inferred to be $\beta_{water} = 2.3 \times 10^{-14} \frac{cm^2}{W}$. When a dye with a high linear absorption was added to the water the linear absorption of the dye could be measured by finding the PPFT as a function of depth of beam focus. From these measurements the irradiance at the beam focus could be determined, and a noticeable decrease in the inferred irradiance threshold for plasma formation was observed as the dye concentration was increased. With the help of a numeric simulation of the absorption of the dye to a focusing laser, in comparison to experimental data, the linear absorption was shown to become saturated for irradances above $4.9 \times 10^7 \frac{W}{cm^2}$. The nonlinear absorption of the dye was also shown to be larger than that of water, so that the total nonlinear absorption with the addition of dye was more than twice that of pure distilled water. For a dye concentration of $1\mu g$ dye in $20mL$ water, the PPFT was just under half of the threshold for pure water. A similar decrease in the PPFT was also observed for several salt water fluids (low linear absorption) commonly used during eye surgery. This agrees well with the material presented in the following chapter where the threshold for plasma formation is found by the multi-photon ionization rate which is proportional to the nonlinear absorption.

The experimental images of the interaction region demonstrated the difference between the linear and nonlinear absorption through the altering of the index of refraction and the formation of short lived micro-bubbles; both were responses to energy absorbed through linear absorption. But at energies above the saturation level of the linear absorption, where nonlinear absorption became dominant, plasma formation started to occur.

Chapter V

Analysis of laser-produced-plasma in water

The work from chapters 2 and 3 led to the conclusion that the interaction that we were observing in the water and gel, the shock wave and cavitation bubble, were directly related to the plasma formed by the focused laser pulse. In one short laboratory session we had the ability run thousands of laser exposures. With a fluid in the beam focus the work became simplified because the sample did not have to be moved between exposures. During each exposure we could record CCD images of the plasma, IR probe light, input energy, and a photo diode trace of the pump beam transmission. The vast amount of captured data made analysis difficult since hand measurements become riddled with coping and human errors. Throughout my time in CICESE one goal was sought, automization of the experiment; the running theme in this thesis was to design experimental and analysis systems where the experimenter would literally write a computer program that would perform and analyze the entire experiment. The material presented in this section is a good example of the automated analysis system. The majority of the data presented in this and the preceding chapter were taken in the month of August of 2008, and is a data set of up to eighteen thousand images, combined with ten thousand photo diode traces, and text files with the input energy of each and every shot. Not just the data collection was considered, but labeling, folders locations, and structure had to be designed to allow easy access in the future by software. The list of experiments, analysis routines, and output graphics (plots, image manipulation) were kept on the experimenter's and laboratory computers along with a digital lab book; an export of the lab book was a web page that could be read or posted on any other computer. The last chapter comes down to not what was seen directly, but inferring the unknown. Going down to the pure form of modern optics, to a model that

causally relates interactions from atoms, electrons, and photons, to sounds and light experienced by an unaided observer. It was shown that a cavitation bubble and shock wave could be created by a focused laser pulse of sufficient energy. The shock wave was related to the irradiance of the input laser pulse which means that its origin was related to the laser produced plasma. A high linear absorber in the water only enhanced the nonlinear aspect of the interaction where the presence of saturable absorption and nonlinear absorption were the dominant mechanisms involved in energy transfer. But through what forces were these transfers taking place remains to be formally addressed in this chapter.

V.1 Pump-probe imaging of nanosecond laser-induced bubbles in distilled water solutions; observations of laser-produced-plasma

This chapter presents the analysis of the laser-produced-plasma (LPP) formed by the focusing of a $9ns$ laser pulse, $\lambda = 532nm$, with a $NA = 0.5$ aspherical lens, into distilled water in varying solutions of table salt. Observations of a plasma filament were made, which are explained by self-focusing of the laser pulse by the LPP through ponderomotive cavitation of the electron plasma in the center of the beam. The filamentation of the beam through a low density plasma wave guide explains why the transmission of the pump laser through the interaction region was notable higher, as mentioned in the last chapter, than other published works investigating similar effects.

V.2 Introduction

In a clear liquid, the delivery of energy can be controlled since absorption only occurs where the laser irradiance is high enough to form a LPP. The mechanical effects of the cavitation bubble have been well demonstrated through its use in cell lysis, (Rau *et al.*, 2004), ablation of cornea, (Niemz *et al.*, 1991), and bilogical tissue (Oraevsky *et al.*, 1996).

Variations in the material properties, elasticity and density, affect both bubble radius

and shock wave propagation; this material response has been modeled (Brujan and Vogel, 2006), and observed, (Vogel *et al.*, 1996a).

When bubble formation was performed in vivo, a lowered threshold for LPP formation was observed and explained to be caused by a higher presence of seed electrons, (Hutson and Ma, 2007). Where the cavitation bubble is well modeled through hydrodynamic modeling, (Rau *et al.*, 2006), the LPP formation requires an understanding of the process of laser-induced ionization, and once ionized, the interactions of electromagnetic field of the laser and the ionized, hot, dense, plasma.

By analyzing the plasma formation and inferring with an accurate model of laser plasma interaction, the electron density and resulting shock wave can be further controlled. A shock wave can be used in laser-shock peening where the shock wave impinging on a surface subjects the surface to extremely high pressures and stresses (Wu and Shin, 2006). Much has been published about picosecond and femtosecond interactions; short pulses have relatively low energy (nJ to μJ) but with very high focused irradiance of 1×10^{15} to $10^{18} \frac{W}{cm^2}$ easily achievable by a table top system, (Vogel *et al.*, 2008).

In the nanosecond regime the interactions are more complicated than pico and femtosecond duration laser pulses because the laser and plasma have more time to interact. The thermalization of electrons and ions occur on the picosecond time scale, energy deposited into the electrons is absorbed into the entire material; electrons and ion lattice (Vogel *et al.*, 1996b). The massive ions can store more heat energy than the tiny electrons. This implies that a nanosecond laser produced plasma, that heats the electrons and ions, would be more energetic than an ultra-fast laser produced plasma which transfers energy to just the electrons.

V.2.1 Laser ionized material

In the absence of linear absorption in the focus of a laser, the material is thought to ionize through the production of seed electrons by multiphoton ionization (Noack and Vogel, 1999), with further ionization caused by acceleration of those electrons in the laser field, causing an avalanch of free electrons.

Oraevsky showed, (Oraevsky *et al.*, 1996), the rate of change of the free electron

density 'n' varies as;

$$\frac{\partial n}{\partial t} = -\beta I n + P(I), \tag{40}$$

where β is the avalanch ionization rate (Stuart *et al.*, 1996), and where $P(I)$ is the multiphoton ionization rate; found through Keldysh formulas. The irradiance is related to the electric field $\mathcal{E}$ by;

$$I = \frac{nc}{2\pi\hbar\omega}|\mathcal{E}|^2, \tag{41}$$

where n is the index of refraction, c is the speed of light, $\hbar$ is Plank's constant, and ω is the laser frequency. As was shown, (Feng *et al.*, 1997), the Drude model for electron density 'ρ', including electron recombination is;

$$\frac{\partial \rho}{\partial t} = \frac{1}{n_b^2}\frac{\sigma}{E_y}\rho I^2 + \frac{\beta^{(k)} I^k}{K\hbar\omega} - a\rho^2 - PlasmaDiffusion. \tag{42}$$

The first term on the right hand side is the avalanch ionization, dependent on the density of electrons ρ and the constant $'a'$. While the second is the multiphoton ionization. The multi-photon absorption coefficient for K-photon absorption β^K, and the laser intensity I. The third term is the electron recombination.

The multiphoton ionization threshold can be written as

$$I_m = \frac{2}{B}\left(\frac{\rho_{0,min}}{\Delta t A}\right)^{1/k}, \tag{43}$$

where A and B are constants given as, (Vogel *et al.*, 1996b), $A = 7.305\times10^{41} s^{-1} m^{-3}$ and $B = 10^{-18}\frac{m^2}{W}$ for our case of $\lambda = 532nm$, and $\rho_{0,min}$ is the minimal initial density of free electrons required to start an avalanche ionization cascade. The avalanche ionization (cascade) threshold is given as;

$$I_c = \left(\frac{mcn_0\epsilon_0 E_{ion}}{e^2}\frac{1+4\pi^2\nu^2 t_{mft}^2}{t_{mft}}\right)\left[g + \frac{2}{\tau} ln\left(\frac{\rho_{cr}}{\rho_0}\right)\right] + \frac{m^2 E_{ion} 4\pi^2\nu^2 c n_0\epsilon_0}{e^2 M}. \tag{44}$$

Where $E_{ion} = 6.5eV$ is the energy to lift an electron to the conduction band, m and e are the electron mass and charge. M is the mass of the water molecule, n_0 is the

index of refraction of the material at frequency ν , ϵ_0 is the permittivity of free space, and g is the rate of electron loss to recombination and trapping.

Short pulsed lasers (nanosecond and longer) generate the majority of the free electrons for the plasma through cascade than multi-photon ionization because of the relation of threshold irradiance for the two processes $I_c > I_m$. The initial electron density ρ_0 is supplied through multiphoton ionization, but the generation of free electrons, while dominated by cascade ionization, is a combination of cascade and multi-photon ionization.

As the beam power increases during the laser pulse, the irradiance of the beam that is equal to, or above the threshold for plasma formation moves up into the focal region of the beam. This model of brekdown where the plasma front moves up the focusing laser beam was well treated by Docchio (Docchio *et al.*, 1988b; Vogel *et al.*, 1996b) who called it the *moving breakdown model*. At high enough energies, this plasma will shield the geometric focus of the beam as shown by Docchio with streak images of the plasma during laser exposure. The time integrated images of these experiments show a plasma in the shape of a cone, pointing in the direction of laser propagation, where the plasma started at the tip and moved to the base.

The time t_B at which the laser irradiance reaches the breakdown threshold at a position z is shown to be, (Fan *et al.*, 2002)

$$t_B(z)_{\pm} = \pm\tau \left\{ \beta \, exp \left[-4ln2 \left(\frac{t}{\tau} \right)^2 \right] - 1 \right\}^{1/2}. \tag{45}$$

If we consider the plasma as a combination of N_T total atoms, where N_e is the number of free electrons, and N_i free ions, then the rate equations can be set as, (Boyd, 2003);

$$\frac{dN_e}{dt} = \frac{dN_i}{dt} = (N_T - N_i)\sigma^{(N)} I^{(N)} - rN_e N_i. \tag{46}$$

Furthermore, the plasma's polarizability is, $P = \alpha(\omega)E$ where;

$$\alpha(\omega) = -\frac{e^2}{m\omega^2}, \tag{47}$$

which gives the dielectric function for plasma as;

$$\epsilon = 1 + 4\pi N\alpha(\omega) = 1 - \frac{\omega_p^2}{\omega^2}, \tag{48}$$

where the plasma frequency $\omega_p = \sqrt{\frac{4\pi N_e e^2}{m_e}}$, and m_e is the electron mass. The plasma frequency is the natural oscillation frequency of the plasma and is approximately given as $\omega_p = 5.64 \times 10^4 \sqrt{N_e}\ \ Rad/s$. As the electron density increases the plasma frequency increases until it is equal to the pump laser frequency, at which point the plasma becomes resonant with the pump laser. The dielectric constant becomes zero, and the plasma acts as a mirror to the laser light. The critical density where the plasma is resonant with a laser of wavelength λ_μ (μm) is $n_c = \frac{m_e \omega^2}{4\pi e^2} = \frac{1.1 \times 10^{21}}{\lambda_\mu^2 cm^{-3}}$.

The presence of free electrons in a dielectric does not directly imply that damage will occur. Damage will be noticed if the density of free electrons can exceed a material determined threshold; this threshold will be close to the value given by Boyde as $N_{th} \approxeq 10^{18} cm^{-3}$ (Boyd, 2003).

As was seen in the previous chapter the formation of plasma in water can be lowered by dissolving dye in the water, but where the dye's nonlinear component is the important addition.

V.3 Experimental system

The experiments presented here used the same system outlined in Chapter 4. Considering the hypothesis that the addition of impurities into the water lowered the PPFT, experiments were performed using solutions of table salt ($NaCl$) in distilled water. Four concentrations of table salt and distilled water were used in the ratios of $100mL$ of water to $10g$, $1.0g$, $0.1g$ and $0.01g$ of common table salt.

For each laser exposure in the liquid, the input pump energy was measured and stored along with an image of the focal region of the laser. The IR probe laser was sent through the target perpendicular to the pump beam. A dielectric mirror (high reflectivity at $532nm$ for $0°$) in front of the CCD was used to filter out any scattered pump light, leaving the image of the LPP and the IR probe beam.

V.3.1 Image analysis

The PPFT was measured in the same manner as the previous chapter. Every CCD image was analyzed by a computer. As shown in figure 37, the red and blue pixel values were used to separate the image of the plasma, and the IR probe beam. This was possible because the IR beam gave equal values on all the colours of pixels, where the plasma was predominantly a red image.

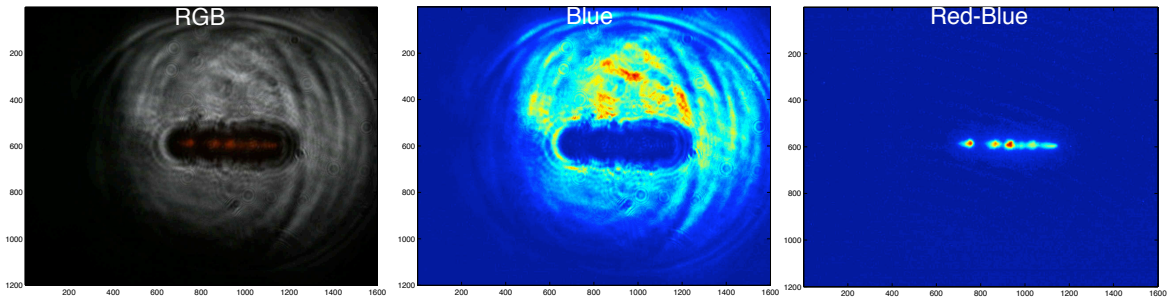

Figure 37: Image of LPP and induced bubble with IR illumination. *Left*: full red-green-blue (RGB), *Middle*: Blue pixel values; IR beam, *Right*: blue pixel values subtracted from red values; plasma

The percentage of laser exposures that created a plasma for a given pulse energy range was plotted with respect to the center energy for that range. The curve then had its derivative taken and fit to a Gaussian. The center of the Gaussian fit corresponded to the pulse energy necessary for a 50% probability for the formation of LPP and has been called the 50% *Probable Plasma Formation Threshold*; PPFT.

V.3.2 PPFT and salt concentration

Seen in chapter 4, solutions of water and predominatly salt displayed a lowered PPFT to pure water. To better understand this relation several water-salt solutions were mixed, and their PPFT measured. As the salt concentration increased, the observed PPFT decreased; figure 38. Both the ocular irrigation fluid and the injectable $DX-CS$ fluid from chapter 4 had PPFT measurements within error of each other, and fell at $295\mu J/pulse$ which was inside the range spanned by the salt solutions of $1.0g$ and $0.1g$.

Both solutions had salt contents between $1g$ and $0.1g$. The only difference was the type of salt, and in the case of the $DX - CS$ solution, the presence of glucose.

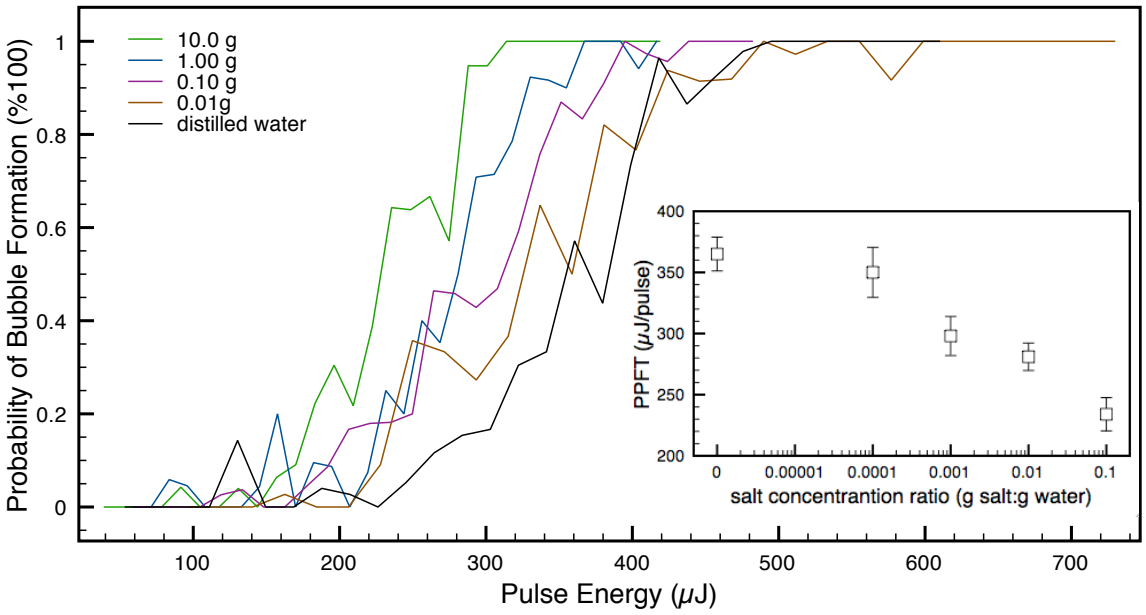

Figure 38: Measured probability of plasma formation curves for water, and water-salt solutions. The inferred PPFT's measured are shown in the insert as a function of salt concentration.

V.3.3 Plasma image

To measure the PPFT, the images of the LPP are made. After extracting the image of the plasma, further analysis concerned with the geometry and intensity of the plasma was performed. The intensity of the plasma was found by assuming that the emission of the plasma radiation comes primarily from black body radiation; a reasonable assumption since the recombination energy should give photons with $6.5eV$ of energy which is soft x-ray light around $100nm$ wavelength. Assuming a uniform electron number density the classical result (non quantum) for the radiation power is

$$P_e = \frac{q_i^2 e^4 N_i N_e}{24\pi^2 \epsilon_0^3 c^3 m_e \hbar \left(\frac{k_B T_e}{m_e}\right)^{\frac{1}{2}}}, \tag{49}$$

where q_i is the charge of the positive ions, and k_B is the Boltzmann constant. If the radiation was blackbody, then that implies that the radiation was not directional, and that what the CCD captured was directly proportional to the total intensity of the plasma. The length of the filament can be shown in two different ways. The first is method is graphical. All the images within the same energy ranges used for the PPFT, and with plasma formation detected were then added together and averaged to give the probable distribution for plasma formation. The resulting averaged image of the plasma formation was sliced out by the computer, and placed in a larger canvas in order of center energy value. Figure 39 is the resulting image, shown with the probability curve used to measure the PPFT overlaid.

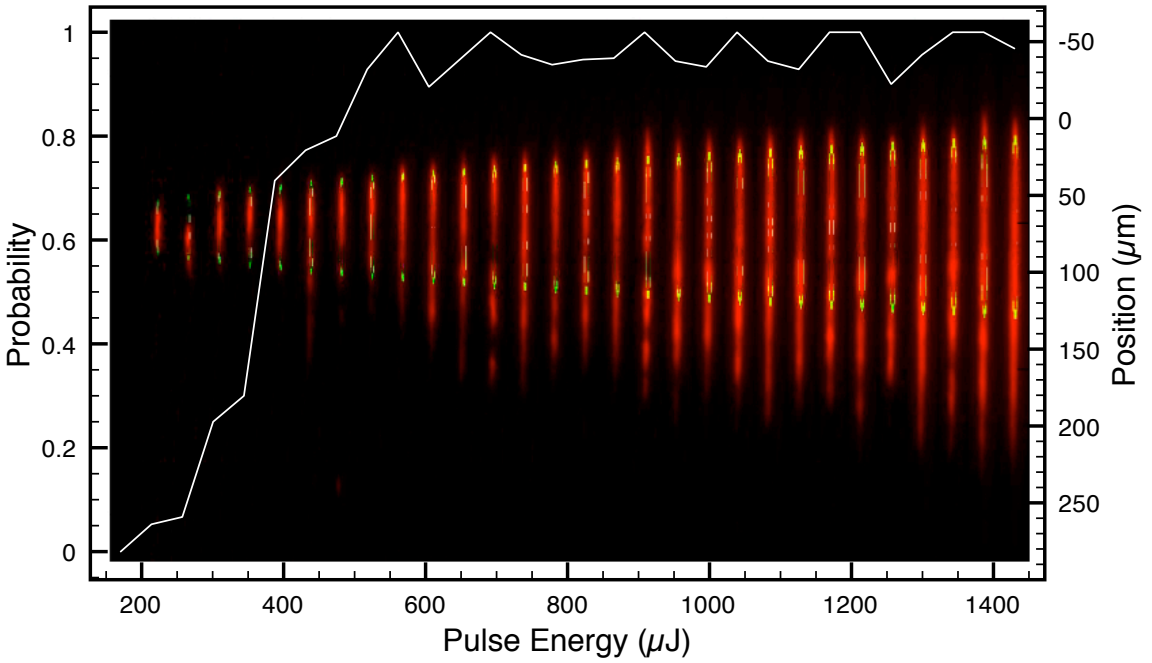

Figure 39: *White line*; increasing energy in the pump laser and the probability of plasma formation. Images of the plasma at the beam focus. Averages of all images with presence of plasma formation within each energy range where the beam was from above. The green line represents a contour of constant irradiance.

For quantitative relations the amount of plasma measured was sought after. A computer program was written that took a threshold intensity of the plasma image, and found the total length of the channel with brightness above the defined threshold. If a

gap occurred in the plasma image, this gap would not be included in the length calculation. By summing the total pixel values in the plasma image a measure proportional to the total intensity of the plasma was obtained. Figure 40 shows the measured relation between the length of the plasma column and the total light emitted.

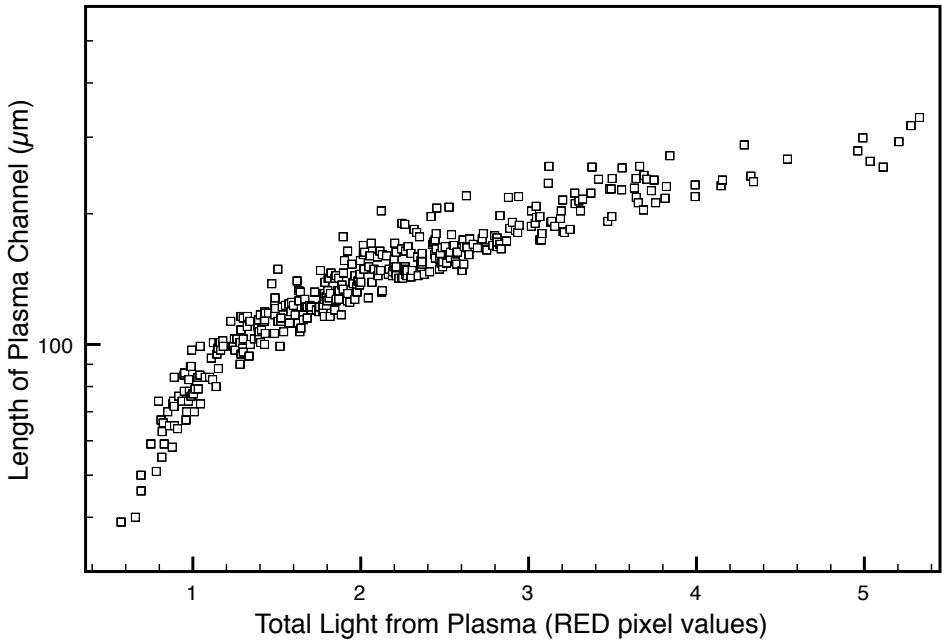

Figure 40: Plot of the length of the plasma column formed by the focused laser versus the total pixel count on the imaging CCD.

V.3.4 Ponderomotive self-focusing and cavitation

The relevance and interest in the material presented so far is when the results are compaired to current literture. Similar experiments using nanosecond, picosecond and recently femtosecond lasers, in water, and at similar wavelength have been performed by Vogel in the 1990's till present. But a slight difference between our experiments and those of Vogel, Noack, Brujan, (Vogel *et al.*, 1996a; Noack and Vogel, 1999; Brujan and Vogel, 2006; Vogel *et al.*, 1996b; Noack *et al.*, 1998) appeared to lead to an insight on the physical mechanisms that are responsible for our observations, and a prediction that may give an accurate understanding of shock wave induced damage.

Measured transmission values were consistently less than those stated in the literature. As well, the observed plasma possessed a different geometrical form; a cylinder as opposed to a cone (figure 41.) During experiments, the laser beam appeared to be making a filament of plasma in the material; the plasma was being created at distances away from the focus where the unaltered beam irradiance was below the threshold for ionization. The laser beam must then have been wave guiding in the plasma. But as shown in equation 48, the dielectric function for plasma is less than unity, so that a beam would want to defocus.

The ability of a laser pulse to selffocus is a well know phenomenon caused by nonlinear material whose real component of $\chi^{(3)}$ alters the index of refraction when high irradiance light is present.

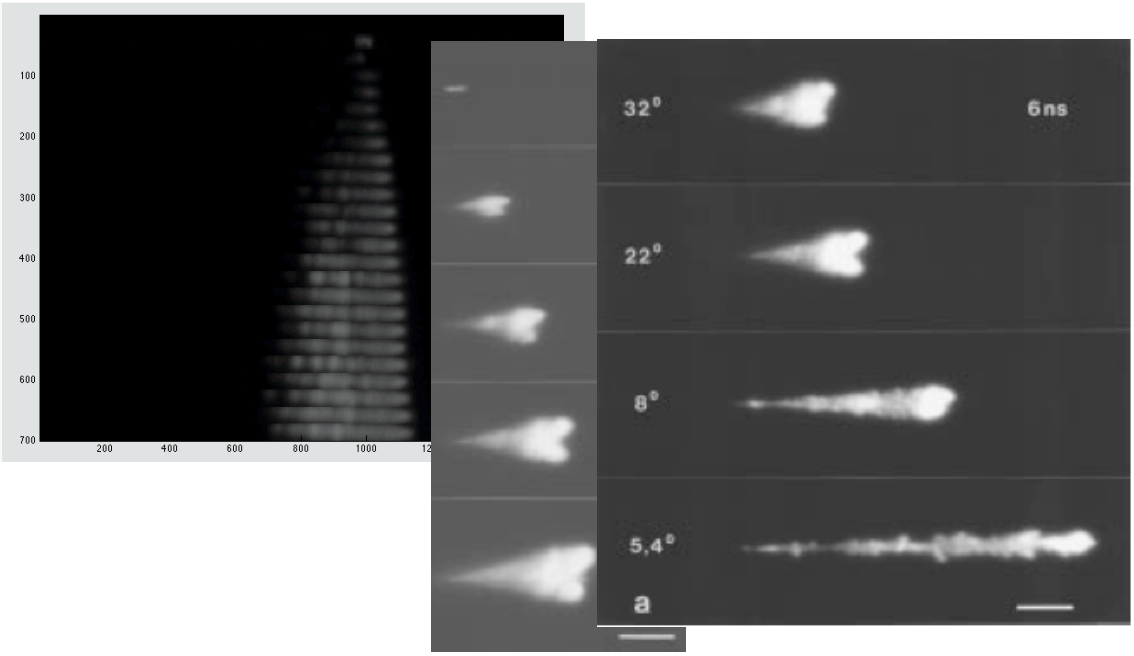

Figure 41: A comparision of images taken of the LPP by Vogel (Vogel *et al.*, 1996b) on the right, and ours on the left. The image magnification is about equal, and images of the same energy are close to alignment.

Nonlinear self-focusing in nonlinear optical material has been widely studied, and a good discussion was written by Marburger in the seventies (Marburger, 1975). For the discussion, the nonlinear response of the material polarization can be represented by

$$P_j^{NL} = \eta|\mathcal{E}|^2\mathcal{E}_j, \tag{50}$$

where the subscript 'j' is a Cartesian coordinate direction. This is a special case for the material response where

$$\eta = 2\chi^3_{jjjj}(-\omega, \omega, -\omega, \omega). \tag{51}$$

In our case, self-focusing is a combination of light diffraction, plasma dispersion, and the n_2 of the material causing a lensing effect. A solution can be made for the critical power necessary for self-focusing. The 'critical' power for wave guiding is

$$P_{cN} = \frac{\sigma_N c\lambda_0^2}{16\pi^2 n_2}, \tag{52}$$

where N is the optical mode that the waveguide traps. The lowest power, and the smallest mode is given by $\sigma_N = 1.86$. Self-focusing of this type was observed and published in 1977 by Smith: (Smith *et al.*, 1977).

When used for a $9ns$ laser pulse with $\lambda = 532nm$, the critical power would require tens of milijouls of pulse energy, or for the pulse duration to be less than a picosecond. This agrees well with the findings of Vogel, (Vogel *et al.*, 1996b) but only for energies above $20mJ$; several orders of magnitude higher than our values.

It is possible for a plasma to wave guide a laser beam. When a very intense laser interacts with an underdense plasma (the critical density is not acheived) the free electrons move in the laser's electric field. As field intensities reach $10^{18}\frac{W}{cm^2}$ the electrons are accelerated to relativistic velocities. Their mass increases, and this affects the dielectric function by the addition of the relativistic mass γm, where γ is

$$\gamma = \frac{1}{\sqrt{1 - \nu^2/c^2}}. \tag{53}$$

The result is a change in the plasma frequency to

$$\omega_p^2 = \frac{4\pi n_e}{\gamma m}. \tag{54}$$

Thus the index of refraction in equation 48 increases and a beam can become guided. A critical power can be derived, (Siegrist, 1976), above which a laser beam will self-focus in a plasma due to relativistic effects

$$P_c r = \frac{\pi \epsilon_0^2 c^5 m_e^3 \omega^2}{n_e e^4}; \tag{55}$$

this gives a critical power of $10^{11} W$. [1] This would require a $10 ns$ pulse to have over $10 J$ of energy; far higher power than what our system was able to provide. Which implies that relativistic focusing, normally visible in pico and femto-second pulsed laser interactions, cannot be the mechanism that affected the observations in this study.

An interesting momentum transfer process occurs in the oscillating electrons in an electric field with a strong time averaged field gradient. Consider, (Fitzpatrick, 1998), an oscillating electromagnetic field that is inhomogeneous in r,

$$\bar{E}(\bar{r}, t) = \bar{E_0}(\bar{r}) cos\omega t, \tag{56}$$

then through the equation of motion of a charged particle in the field

$$m \ = e \left[\bar{E_0}(\bar{r}) cos\omega t + \nu \times \bar{B_0}(\bar{r}) sin\omega t \right], \tag{57}$$

where

$$\bar{B_0} = \omega^{-1} \bigtriangledown \bar{E_0}. \tag{58}$$

Concentrating on the non-oscillating effect a time average is performed by separating oscillating and constant terms from each other. The particle must not move much in an oscillation, such that

$$(\nu \centerdot \bigtriangledown) \bar{E} \ll \omega \bar{E}. \tag{59}$$

A potential can be defined for an electron in this field and is given as;

$$m \frac{d\bar{U}}{dt} = -e \bigtriangledown \phi_{pond}, \tag{60}$$

[1] This corresponds to beam irradiance of $10^{17} \frac{W}{cm^2}$

where

$$\phi_{pond} = \frac{1}{4}\frac{e}{m\omega^2}|\bar{E_0}|^2. \tag{61}$$

The force that causes the potential in equation 60 is called the ponderomotive force, and with plane waves on a target of $10^{21}\frac{W}{cm^2}$, electrons can be sent into the material with up to GeV of kinetic energy (Pukhov, 2003); this scheme has been used as the source for table top particle accelerators. The index of refraction can again be modified to take account for the density of the electron plasma (keeping the relativistic term for completeness) (Esarey *et al.*, 1997);

$$\eta_r(r) = 1 - \frac{\omega_p^2}{2\omega^2}\frac{n(r)}{n_0\gamma(r)}. \tag{62}$$

The plasma frequency ω_p is found with the ambient plasma density n_0. Where both the plasma density $n(r)$ and the relativistic factor $\gamma(r)$ vary with respect to radius.

There is a balance of the ponderomotive force with the plasma pressure. Neglecting plasma heating, the plasma density has been shown to be; (Osman *et al.*, 1999)

$$n_{eo} = n_e exp\left(-\frac{E^2}{8\pi n_{ec}T}\right), \tag{63}$$

where n_{eo} and n_e are the modified and unmodified electron densities. T is temperature in energy units.

Young published results in 1995, (Young, 1995b) where the change in the index of refraction due to ponderomotive focusing was found to be

$$\frac{\delta n}{n_0} = 1 - exp\left[-\frac{3}{8}\frac{\nu_0}{\nu_e}\right], \tag{64}$$

where $\nu_0 = eE_0/m\omega$ is the electron quiver velocity, and $\nu_e = (T_e/m)^{1/2}$ is the electron thermal velocity. The experiment that Young was trying to model was a large (weakly focused, several hundred micrometers in diameter) beam propagating into a larger plasma created by a second heater beam. What he and several other authors have published is that distortions, or irregularities in the beam irradiance or phase become amplified, and turn into filaments of light probing the plasma: (Young, 1995a).

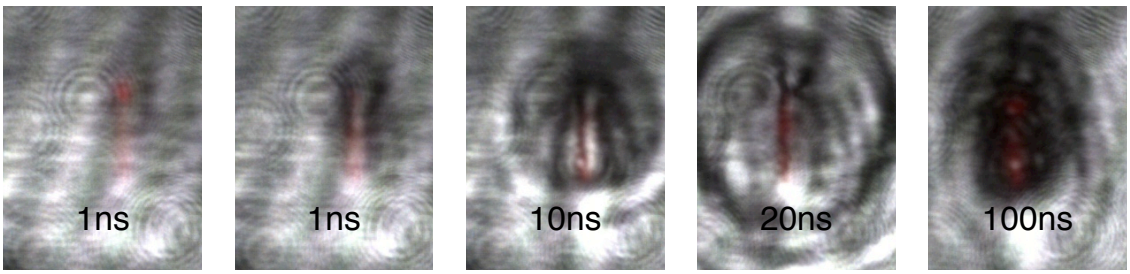

Figure 42: Images showing the formation of a filament in water with direct red dye; $\alpha = 3.8cm^{-1}$. The laser was incident from the bottom. At the images taken with a delay of 10 and 20 ns show the channel in the middle of the plasma (seen as red). The exit of the channel can be seen as well by the cone in the water caused by heating and saturation of the linear absorption of the dye.

At this point solutions to the size of the wave guide, plasma densities, and beam irradiance are highly nonlinear. The system is governed by a complex set of nonlinear differential equations whose solutions must be solved numerically. The system can also be numerically modeled through Particle in Cell (PIC) models of the plasma, from which beam propagation simulations can be solved for the propagating electric field in the LPP (Chiron *et al.*, 1996). Much excellent analytic work has be published as well, but is not directly applicable to our case (Brandi *et al.*, 1993).

Without a calculated plasma density for our experiments to prove that electron cavitation occurs in the center of the beam filament, published experimental evidence of this type of filamentation has been used in comparison with our work. Work with a laser focused into a hydrogen gas jet has been published with results very similar to what we observe, (Gibbon and Forster, 1996). But as with the many other more recent papers, (Jukna *et al.*, 2008; Vogel *et al.*, 2008; Hutson and Ma, 2007; Yu *et al.*, 2007), the lasers had shorter pulse durations, and the filamentation would be caused through relativistic and ponderomotive effects. But still important are the images in figure42, where evidence of the channel in water with dye can be seen to form. The images are similar to what has been published with shorter laser pulses.

Figure 43 shows the analysis of the images from figure 39. The left image is a surface plot of the plasma image; line-out versus pulse energy. The right image is a plot of the plasma column length as a function of the input energy. The data points are

proportional to the light from the plasma divided by the plasma column length; light density.

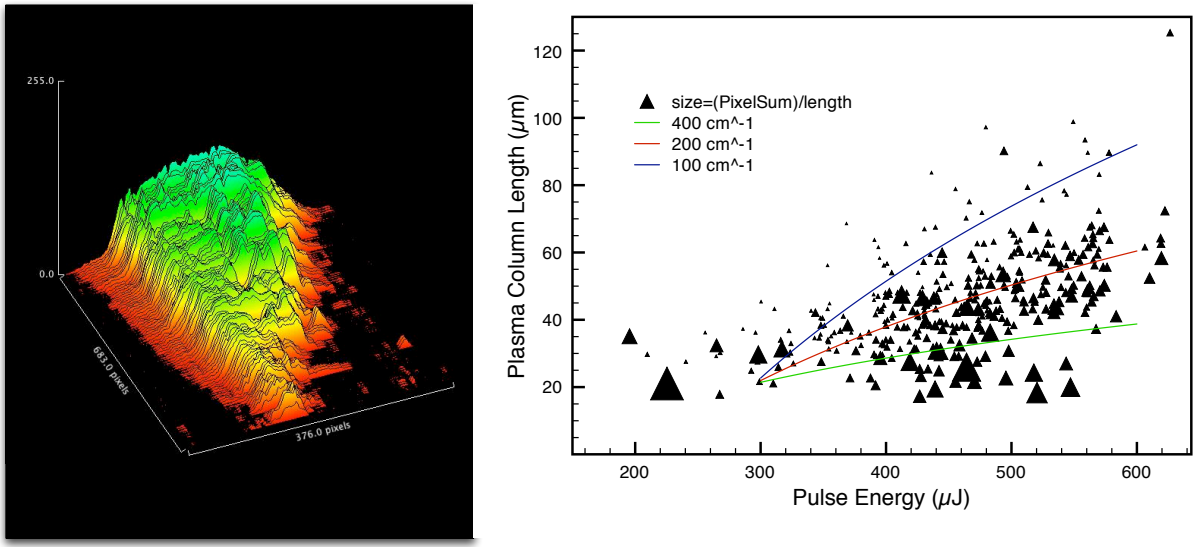

Figure 43: Variation of plasma column length with increasing pump pulse energy. Each data point represents one laser pulse. The size of the data point is proportional to the length of the plasma column to the total brightness of the plasma. The amount of light from a plasma increase with density and temperature, so the smaller the data point, the denser hotter the plasma was. Shown are plots for distance of propagation before laser power falls below a threshold peak power, through loss of an absorptive medium. The damage threshold set at $300\mu J/pulse$ and the plasma absorption at $100cm^{-1}$, $200cm^{-1}$, and $400cm^{-1}$ for blue, red, and green traces respectively.

The fit shown in figure 43 came from the assumption that a plasma was formed whenever the laser irradiance was above the threshold for material ionization. A maximum length of the plasma channel can be hypothized by asumming the laser was wave guided and that energy loss was caused by absorption and random scattering, so that the Berr-Lambert law relates the critical energy for plasma formation E_{crit} to the filament length z_p as,

$$E_{crit} = E_{in}e^{-\alpha z_p}. \tag{65}$$

Where E_{in} is the input pump pulse energy. Solving for z_p gives,

$$z_p = -\frac{1}{\alpha}\left(log(E_{crit}) - log(E_{in})\right). \tag{66}$$

Equation 66 is used as a fit function for the plasma length versus energy in figure 43, to give a threshold energy for plasma formation and guiding of $300\mu J/pulse$ and a plasma absorption coefficient of $200cm^{-1}$, agreeing well with published results: (Niemz *et al.*, 1991; Vogel *et al.*, 1996b; Gamaly *et al.*, 2006).

This result is interesting since it implies that at energies below our PPFT we still find the possibility for filamentation of the laser beam. Figure 44 plots the vertically binned pixel values for the LPP that were formed in water. Even for the lowest energy shown, equal to the measured PPFT, there was evidence of a slightly elongated plasma channel. The rest of the images in figure 44 agree well with simulations that have attempted to solve the beam width of a ponderomotive self-focusing laser beam, where oscillations of the beam diameter occur about a stable beam radius (Osman *et al.*, 1999; Chiron *et al.*, 1996). That beam radius was shown by those authors to grow with increasing energy. Figure 44 has oscillations of the plasma radius on the same length scale as the publications, and if there was a linear absorption in the plasma, the energy would be dropping, and so too would the center of the radius oscillations decrease; this is well pronounced for the energies above $1mJ/pulse$.

More than just making a channel for the laser to propagate, which does account well for the increase in laser transmission that we observed (Evans *et al.*, 2008), the sudden movement of electrons away from the beam focus acts as a momentum transfer from the laser beam to the electrons. Through collisions with the material lattice and coloumb explosion of the positively charged ions left in the beam path, a cavitation bubble originates in the plasma defined region. A simulation looking for electron cavitation was published which showed that every time the beam width collapsed, an electron cavitation was created in the plasma (Yu *et al.*, 2007). Figure 45 shows an image of the laser produced bubble and shock wave in water. The center of the bubbles were found to lye a the collapse point of the laser plasma that could be extracted from the image. So a direct relation to the bubble center, and the location of the possible electron cavitation coincide.

The remaining question is why our observed results do not mimic those of Vogel.

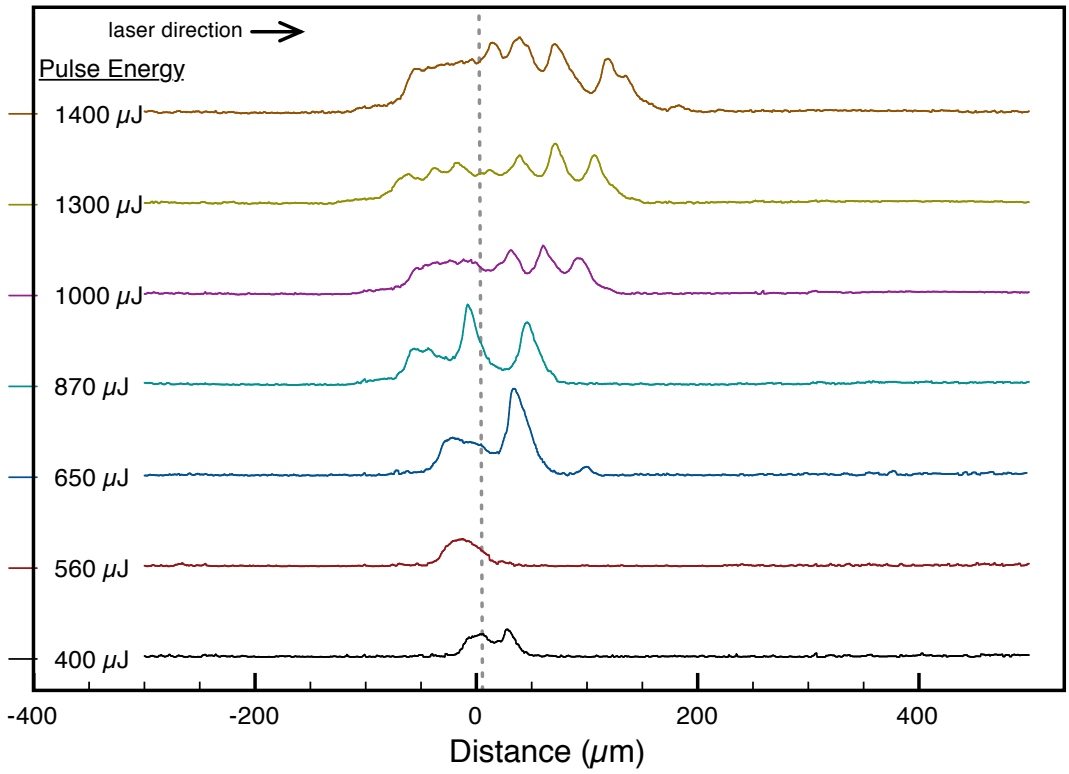

Figure 44: Plasma intensity plots. A plot of the vertical summation of CCD pixel values from images taken at energies throughout the range of exposures. The horizontal axis is centered close to the beam waist. These line outs are single exposures, so no averaging exists, as opposed to figure 39

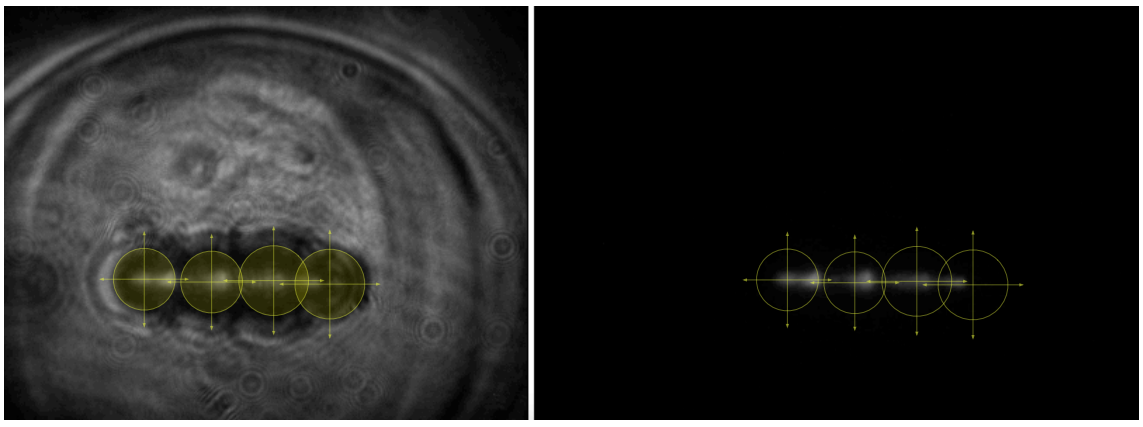

Figure 45: Center of bubble formation inferred (left image), and compared to plasma location (right image)

Figure 46 is the output of the simulation used in chapter 4, where the material considered is water with linear and nonlinear absorption. The family of curves are the transmission of the focused beam in a $1cm$ cuvette of water. Each curve represents a beam with a different beam waist. The single curve in black is the transmission for a $1mJ$ pulse versus beam waist size. The beam waist size listed are the ideal size found using the Gaussian equations with numerical aperture or focusing angle; the simulation considered all beams to have a $M^2 = 6$ so that the real beam waist would be six times the upper x-axis. The maximum focusing presented by Vogel with accompanying plasma images or transmission was 33° which corresponds to the points in the minimum of transmission. The experiments presented had an ideal beam waist of $0.2\mu m$. The transmission curve demonstrates the balance between more material with lowered irradiance to the increased absorption. At the tight focus that was used for our experiments, the beam only began to become absorbed close to the beam waist, so that at the beam waist, almost the full beam energy was present to give the irradiance necessary to drive the ponderomotive force to make a filament and therefore creating a ponderomotive wave guide for laser light in the pump pulse to pass through. In the case of Vogel, the plasma was generated far enough from the beam focus that by the time the spot size had collapsed up to half its energy had been absorbed, and filamentation was not possible. It should be noted that while the ponderomotive force was not able to make a wave guide in the plasma, it would still be present for Vogel; even stronger than our case since the momentum transfer would be stronger due to a hotter, denser plasma.

V.4 Conclusion

This chapter presented a thorough image and data analysis of LPP in water by a tightly focused ($> NA = 0.5$) nanosecond laser pulse. The high transmission of our laser beam in the plasma has been shown to be accounted for by a low density plasma channel made through ponderomotive self-focusing of the laser beam. The ponderomotive focusing of the beam created not just a lower density plasma channel, but also the resulting

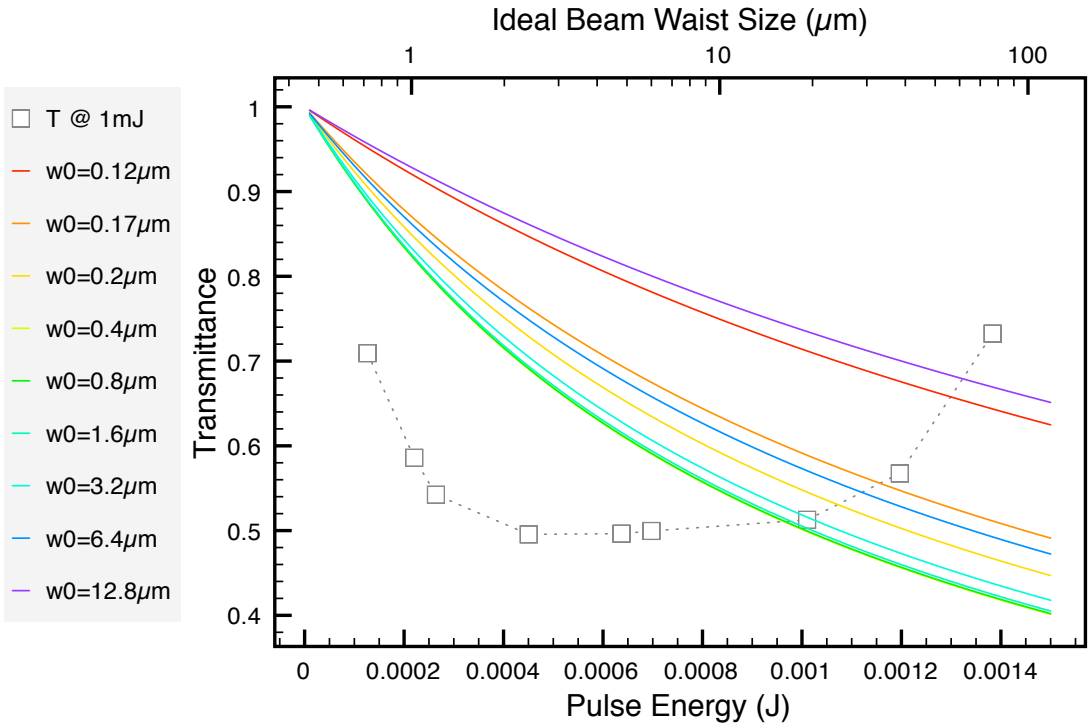

Figure 46: Calculated laser transmission for varying beam waist sizes. The beam waist size are the ideal sizes, all beams were considered to have a $M^2 = 6$.

electron cavitation which appeared to have had a causal relation to the later formed cavitation bubbles.

It is possible to say that the form of the cavitation bubbles were defined by the electron cavitation, and thus directly related to the LPP and laser beam. This picture is in contrast to all published works that believe that the bubbles and shock waves come about due to an explosive expansion of hot gas formed by the LPP. Most probably, both processes exist.

This hypothesis is directly testable since the ponderomotive force does not produce a waveguide in the plasma if the laser is circularly polarized (Sprangle *et al.*, 1996). Further simulation is also required to model our system exactly, and could be best done by the used of a PIC code.

Chapter VI

Conclusion and further work

After the above chapters what conclusions can be drawn? As high irradiance laser light impinges on a surface the strong electric field accelerates electrons, heating the irradiated material. It is the response of those electrons, how they radiate light and couple into sound waves that give the full extent of interactions. Even for pulse energies less than the damage threshold for a metal, these interactions can cause the formation of periodic surface structures. Originating from a random fluctuation in the surface shape, the electric field, combined with a feed back mechanism, can encode its wave length in periodic surface structuring. In solid copper the feedback mechanism is the melting and resolidifcation of the surface. In titanium and tungsten in air, the laser can cause the metals to oxidize and crystalize. The oxides became perforated with nanometer size craters. With titanium, the oxide can be formed with a periodicity equal to the laser wavelength.

As the laser focus moves inside a transparent material the combination of the focusing laser beam and irradiance dependent material polarization allow for interactions in the bulk of the material free of any interfaces. There is an interplay of the saturation of single photon linear absorption, and irradiance induced two-photon nonlinear absorption. For a laser with a wavelength of $532nm$ focused inside water, it is three photon absorption that transfers sufficient energy to lift an electron into the conduction band. From these seed electrons, sufficient time, and a strong electric field, the entire focal volume under laser exposure becomes ionized through cascade ionization.

Once a plasma is formed, the electron interaction to the laser light changes, and energy absorption increases. Vogel and Docchio measured an increase in absorption with higher energies. But in our experiments we observed that the presence of plasma will lower the transmission, but that the rate of change of the transmission relative to

pulse energy remains constant; the slope in the transmission plot is set by the nonlinear absorption which in plasma should be much higher than in water. While a plasma is created, the gradient of the averaged electric field, if strong enough, can push the freed electrons out of the high irradiance area. The shift in plasma density in the laser beam focus causes a low density wave guide. Evidence of a waveguide consisting of a low electron density was that the laser produced plasma filament extended beyond the region where non-guided beam could produce a plasma.

Interestingly, the wave guide should be turned off, or affected greatly if the laser is circularly polarized. This remains untested, but if shown to be true, this allows a way to turn on and off an irradiance dependent interaction. Ultra-short pulsed laser should not see the same type of change with laser polarization because it is the changing electron mass, and not density that allows for filamentation.

In the thin film interactions, the polarization of the laser beam determines the grating direction, and circularly polarized light prevented the grating from forming at all. Patterns in the thin films should also be affected by the angle of incidence of the irradiating laser. If the exposures on solid metals are any guide, the angle of incidence, substrate material, film thickness, and the surface texture, should all affect the final grating characteristics. There are many applications where gratings made of titanium dioxide could be useful, such as memristors, gas sensors, radiation detectors etc... The next step in the thin film work would be to see why a grating did not form on the tungsten target, and to see what happens if oxygen is blown on the target during irradiation. The role of defects in the film should be investigated; determined by film thickness and deposition technique. And when it is possible, exposures with femtosecond laser pulses may lead to interesting results as well.

The work remaining to be done with the cavitation bubbles and plasma analysis is vast. Just the surface of this area of study has been touched. As mentioned above, the use of circularly polarized light should have interesting consequences. It would be prudent to use a lower NA focusing optic in hopes of duplicating the plasma seen in other publications. There is also a wide area of application for femtosecond pulses. While the nanosecond laser pulses were the source of the interactions (shorter pulses

will not see ponderomotive filamentation), femtosecond pulses used as a probe beam would given new insight to the formation of the laser produced plasma. The nanosecond probe beam could resolve the shock wave, but the short lived plasma would always be a time averaged image over the nine nanosecond pulse duration. A femtosecond probe beam would allow for observation of the growth of the plasma. If the femtosecond pulse could be converted to a white light source, a transmission spectrum of the plasma may allow for measuring of the plasma density as well.

While working on this thesis, the underlying theme of design has been prominent. An understanding of the physics of laser matter interaction, combined with the availability of optical apparatus, and the abilities of our fabrication facilities, were the main limits and design parameters that we had to work with. A well designed experiment is repeatable, and tweeze apart the aspects of the physical theory. But most important, the apparatus must be enjoyable to use. An awkward, uncomfortable system causes as many problems as an unstable, overly complicated system. What has been built in the CICESE laboratory is not really a microprocessing system, but a frame work where such a system can easily be set up. In a medical application simplicity is wanted; a black box with a red button is ideal. But for a physics laboratory, flexibility is the ideal. In this thesis four configurations of the microprocessing system were presented. It was a long term goal to leave the lab with a list of optical configurations, computer simulations, and forms of analysis for future scientists to build on to. Hopefully this thesis will become part of that greater work, as a formal presentation of what was achieved so far, and a list of where new discoveries can be made.

Bibliography

Beattie, I. R. and T. R. Gilson 1969. "Oxide phonon spectra". J. Chem. Soc. A, 1(1):2322-2328 p.

Boyd, R. W. 2003. "Nonlinear optics". Academic Press, 525 B Street, Suite 1900, San Diego, CA 92101-4495, USA; http://www.academicpress.com, 2nd edition.

Brandi, H. S., C. Manus, and G. Mainfray 1993. "Relativistic and ponderomotive self-focusing of a laser beam in a radially inhomogeneous plasma. I. paraxial approximation". Phys. Fluids B, 5(10):3539-3551 p.

Brujan, A. and A. Vogel 2006. "Stress wave emission and cavitation bubble dynamics by nanosecond optical breakdown in a tissue phantom". J. Fluid Mech., 558:281-308 p.

Brujan, E. A., K. Nahen, P. Schmidt, and A. Vogel 2001. "Dynamics of laser-induced cavitation bubbles near elastic boundaries: influence of the elastic modulus". J. Fluid Mech., 433:283-314 p.

Brunette, D., P. Tengvall, M. Textor, and P. Thomsen 2001. "Titanium in medicine; material science, surface science, engineering , biological responses and medical applications". Springer, Haberstr. 7, 69126 Heidelberg, Germany.

Camacho-López;, M., L. Escobar-Alarcòn;, and E. Haro-Poniatowski 2004. "Structural transformations in MoO_x thin films grown by pulsed laser deposition". Appl. Phys. A., 78:59-65 p.

Camacho-López, S., R. T. Evans, L. Escobar-Alarcon, M. A. Camacho-López, and M. A. Camacho-López 2008. "Polarization dependent single-beam laser-induced grating-like effects on titanium films". Appl. Surf. Sci., 255:3028-3032 p.

Cazzanelli, E., L. Papalino, A. Pennisi, and F. Simone 2001. "Spatial variation of structural order in sputtered WO_3 films". Electrochem Acta, 46:1937-1944 p.

Chiron, A., G. Bonnaud, A. Duieu, J. L. Miquel, G. Malka, and M. Louis-Jacquet 1996. "Experimental observations and simulations on relativistic self-guiding of an ultra-intense laser pulse in underdense plasmas". Phys. Plasmas, 3(4):1373-1401 p.

de-la Cruz, A. R. and R. Rangel-Rojo 2006. "Compact multi-pass amplifier for chirped-pulse amplification". J. Modern Opt., 53(3):307-11 p.

Dean, J., M. Bercx, F. Frank, R. Evans, S. Camacho-López, M. Nantel, and R. Marjoribanks 2008. "The effects of degraded spatial coherence on ultrafast-laser channel etching". Optics Express, 16:13606-13616 p.

del Pino, A. P., J. M. Fernández-Pradas, P. Serra, and J. L. Morenza 2004. "Coloring of titanium through laser oxidation: comparative study with anodizing". Surface & Coatings Technology, 187:106-112 p.

Diniz, M. G., G. A. Soares, M. J. Coelho, and M. H. Fernandes 2002. "Surface topography modulates the osteogenesiss in human bone marrow cell cultures grown on titanium samples prepared by a combination of mechonical and acid treatments". J. Mater. Sci.: Mat. Med., 13:421-432 p.

Docchio, F., P. Regondi, M. R. C. Capon, and J. Mellerio 1988a. "Study of the temporal and spatial dynamics of plasmas induced in liquids by nanosecond $Nd:YAG$ laser pulses. 1: Analysis of the plasma starting times". Appl. Opt., 27(17):3661-3669 p.

Docchio, F., P. Regondi, M. R. C. Capon, and J. Mellerio 1988b. "Study of the temporal and spatial dynamics of plasmas induced in liquids by nanosecond $Nd:YAG$ laser pulses. 2: Plasma luminescence and shielding". Appl. Opt., 27(17):3669-3675 p.

Doukas, A. G., A. Zweig, J. Frisoli, R. Blrngruber, and T. Deutsch 1991. "Non-invasive determination of shock wave pressure generated by optical breakdown". Appl. Phys. B, 53:237-245 p.

Esarey, E., P. Sprangle, J. Krall, and A. Ting 1997. "Self-focusing and guiding of short laser pulses in ionizing gases and plasmas". IEEE Journal of Quantum Electronics, 33(11):1879-1915 p.

Evans, R., S. Camacho-López, M. A. Camacho-López, C. Sánchez-Pérez, and A. Esparza-García 2007. "Pulsed laser-induced effects in the material properties of tungsten thin films". J.of Phys:Conference Series, Eighth International Conference on Laser Ablation, V(59):436-439 p.

Evans, R., S. Camacho-Lópezpez, F. Perez, and G. Aguilar 2008. "Pump-probe imaging of nanosecond laser-induced bubbles in agar gel". Optics Express, 16(10):7481-7492 p.

Fan, C. H., J. Sun, and J. P. Longtin 2002. "Plasma absorption of femtosecond laser pulses in dielectrics". Journal of Heat Transfere', 124:275-284 p.

Feng, Q., J. V. Moloney, A. C. Newell, E. M. Wright, K. Cook, P. K. Kennedy, D. X. Hammer, B. A. Rockwell, and C. R. Thompson 1997. "Theory and simulation on the threshold of water breakdown induced by focused ultrashort laser pulses". IEEE J. Quantum Electron., 33(2):127-138 p.

Fitzpatrick, R. 1998. "Introduction to plasma physics". Course notes for University of Texas at Austin, Institute for Fusion Studies, URL: http://farside.ph.utexas.edu/teaching/plasma/plasma.html.

Forrester, P., K. Bol, L. Lilge, and R. Marjoribanks 2006. "Effects of heat transfer and energy absorption in the ablation of biological tissues by pulsetrain-burst ($> 100MHz$) ultrafast laser processing". Proc. SPIE - Int. Soc. Opt. Eng. (USA), 6343(63430J-1).

Gamaly, E., S. Juodkazis, K. Nishimura, H. Misawa, and B. Luther-Davies 2006. "Laser-matter interaction in the bulk of a transparent solid: Confined microexplosion and viod formation". Phys. Rev. B, 73(214101):1-15 p.

García, S., F. Fuentes, and C. Paz 2000. "Explicit electromagnetic algorithm for $2D$ using a multi-fluid model in laser-produced plasmas". Computer Physics Communications, 127:271-285 p.

Georg, A., W. Graf, and V. Wittwer 2001. "The gasochromic colouration of supttered WO_3 films with a low water content". Electrochem Acta, 46:2001-2005 p.

Gibbon, P. and E. Forster 1996. "Short-pulse laser-plasma interactions". Plasma Phys. Control. Fusion, 38:769-793 p.

Gojani, A. B. and K. Takayama 2008. "Experimental determination of shock hugoniot for water, castor oil, and aqueous solutions of sodium chloride, sucrose and gelatin". Materials Science Forum, 566:23-28 p.

Granqvist, C. G. 1994. "Electrochromic oxides: Systematics, materials, and applications to smart windows". Renewable Energy, 5:141-153 p.

György;, E., A. P. del Pino;, P. Serra;, and J. Morenza 2004. "Chemical composition of dome-shaped structures grown on titanium by multi-pulse $Nd : YAG$ laser irradiation". Appl. Surf. Sci., 222:415-22 p.

Hale, G. M. and M. R. Querry 1973. "Optical constants of water in the $200nm$ to $200\mu m$ wavelength region". Appl. Opt., 12(3):555-564 p.

Haydn, C. 2003. "Oxide and nitride thin films: processing and characterization". Materials Science Forum, 437-8:193 pp.

Hertwig, A., S. Martin, J. Krüger, and W. Kautek 2004. "Surface damage and color centers generated by femtosecond pulses in borosilicate glass and silica". Appl. Phys. A., 79:1075-1077 p.

Hutson, M. and X. Ma 2007. "Plasma and cavitation dynamics during pulsed laser microsurgery in vivo". Phy. Rev. Let, 99(158104).

Itoh, K. and W. Watanabe 2005. "Integration of three-dimensional waveguides by femtosecond laser pulses". In: "Photonics Based on Wavelength Integration and Manipulation", volume Book 2. IPAP, 355 pp.

Jukna, V., G. Tamosauskas, G. Valiulis, M. Aputis, M. Puida, F. Ivanauskas, and A. Dubientis 2008. "Filamentation of ultrashort light pulses in a liquid scattering medium". Appl. Phys. B, 94:175-179 p.

Kanellos, M. 2008. "HP makes memory from a once-theretical circuit". cnet.

Korotcenkov, G. 2007. "Metal oxides for solid-state gas sensors: What determines our choice?". Materials Science and Engineering A, 139:1-23 p.

Krasovec, U. O., A. S. Vuk, and B. Orel 2001. "IR spectroscopic studies of charged-discharged crystalline WO_3 films". Electrochem Acta, 46(13-14):19221-1929 p.

Lazcano-Hernández, H. E., C. Sánchez-Pérez, and A. García-Valenzuela 2008. "An optically integrated NH_3 sensor using WO_3 thin films as sensitive material". J. Opt. A. Pure. Appl. Opt., 10(104016):1-7 p.

Lerner, K. L. and B. W. Lerner, editores 2004. "The gale encyclopedia of science", volume 5 of Gale Encyclopedia of Science. Thomson Gale, 27500 Drake Rd. Famington Hills, MI 48331-3535, 3rd edition.

Lian, J., Q. Dong, Z. Guo, Q. Xu, J. Yang, J. Hu, Q. Guan, and B. Chen 2005. "Surface oxidation kinetics of Cr film by $Nd:YAG$ laser". Materials Science and Engineering A, 391:210-220 p.

Liu, M. X., Y. L. Huang, F. Ma, and K. W. Xu 2007. "Template-induced formation of a $\alpha - W$ and size-dependent properties of tungsten thin films". Materials Science and Engineering B, 139:99-104 p.

Liu, X., D. Du, and G. Mourou 1997. "Laser ablation and micromachining with ultrashort laser pulses". IEEE J. Quantum Electron., 33(10):1706-1717 p.

Loesel, F. H., C. Horvath, F. Grabon, M. Jost, and M. H. Niemz 1997. "Self-starting femtosecond operation and transient dynamics of a diode-endpumped $Cr:LiSGaF$ laser with a semiconductor saturable absorber mirror". Appl. Phys. B, 65:783-787 p.

Losier, P. and P. Ashrit 2003. "Flash evaporated tungsten oxide thin films for electrochromic applications". Journal of Materials Science Letters, 22(15):1095-8 p.

Maillé, L., C. Sant, C. L. Paven-Thivet, C. Legrand-Buscema, and P. Garnier 2003. "Structure and morphological study of nanometer W and W_3O thin films". Thin Solid Films, 428:237-241 p.

Maisterrena-Epstein, R. 2006. "Caracterización de la ablación láser en metales y en PMMA con pulsos cortos (ns) y ultra cortos (fs)". Tesis de Maestría, CICESE (Centro de Investigación Científica y Educación Superior de Ensenada), Km. 107 Carretera Tijuana-Ensenada BC 22860 Mexico.

Mao, S., F. Quere, S. Guizard, X. Mao, R. Russo, G. Petite, and P. Martin 2004. "Dynamics of femtosecond laser interactions with dielectrics". Appl. Phys. A, 79:1695 pp.

Marburger, J. H. 1975. "Self-focusing: Theory". Prog. Quant. Electr., 4:35-110 p.

Marjoribanks, R. S., F. W. Budnik, L. Zhao, G. Kulcsár, M. Stainer, and J. Mihaychuk 1993. "High-contrast terawatt chirped-pulse-amplification laser that uses a 1-ps $Nd:glass$ oscillator". Optics Letters, 18(5):361-364 p.

Maxwell, I., S. Chung, and E. Mazur 2005. "Nanoprocessing of subcellular targets using femtosecond laser pulses". Medical Laser Applications, 20:193-200 p.

Mina-Rosales, A. 2007. "Ablación de tejido corneal con pulsos de nanosegundo y femtosegundos". Masters thesis, CICESE (Centro de Investigación Científica y Educación Superior de Ensenada), Km. 107 Carretera Tijuana-Ensenada BC 22860 Mexico.

Moulton, P. F. 1986. "Spectroscopic and laser characteristics of $Ti:Al_2O_3$". J. Opt. Soc. Am. B, 3(1):125-134 p.

Nagayama, K., Y. Mori, Y. Motegi, and M. Nakahara 2006. "Shock hugoniot for biological materials". Shock Waves, 15:267-275 p.

Nahen, K. and A. Vogel 1996. "Plasma formation in water by picosecond and nanosecond $Nd:YAG$ laser pulses—part II: Transmission, scattering, and reflection". J. Sel. Top. Quant. Elect., 2(4):861-872 p.

Niemz, M. H., E. G. Klancnik, and J. F. Bille 1991. "Plasma-mediated ablation of corneal tissue at 1053 nm using a $Nd:YLF$ oscillator/regenerative amplifier laser". Laser in Surgery and Medicine, 11:426-431 p.

Nishimura, T., K. Taira, and S. Kurita 1980. "Proton injection phenomena in WO_3-electrolyte electrochromic cells". Applied Physics Letters, 36(77):585-7 p.

Noack, J., D. X. Hammer, G. Noojin, B. Rockwell, and A. Vogel 1998. "Influence of pulse duration on mechanical effects after laser-induced breakdown in water". J. Appl. Phys., 83(12):7488-7496 p.

Noack, J. and A. Vogel 1999. "Laser-induced plasma formation in water at nanosecond to femtoecond time scales: Calculation of thresholds, absorption coefficients, and energy density". IEEE J. Quantum Electron., 35(8):1156-67 p.

Oraevsky, A., L. D. Silva, A. Rubenchik, M. Feit, M. Glinsky, M. Perry, B. Mammini, W. Small, and B. Stuart 1996. "Plasma mediated ablation of biological tissues with nanosecond-to-femtosecond laser pulses: Relative role of linear and nonlinear absorption". IEEE Journal of Quantum Electronics, 2(4):801-810 p.

Osman, F., R. Castillo, and H. Hora 1999. "Relativistic and ponderomotive self-focusing at laser-plasma interaction". J. Plasma Physics, 61(2):263-273 p.

Ozkan, E. 2001. "Optical, structural and electrochromic characteristics of sol-gel deposited tungsten oxide and transition metal oxide doped tungsten oxide films at various temperature". 19th International Congress on Glass, 1(1):125 pp.

Pedraza, A. J., J. D. Fowlers, and Y. F. Guan 2003. "Surface nanostructuring of silicon". Appl. Phys. A, 77:277-284 p.

Pèrez, J. J., P. Sakanaka, M. Algatti, and J. Mendoza-Alvarez 2001. "An improved three-dimensional model for growth of oxide films induced by laser heating". Appl. Surf. Sci., 175-176:703-8 p.

Porto, S. P. S., P. A. Fleury, and T. C. Damen 1967. "Raman spectra of TiO_2, MgF_2, ZnF_2, FeF_2, and MnF_2". Phys. Rev., 154(2):522-527 p.

Pukhov, A. 2003. "Strong field interaction of laser radiation". Rep. Prog. Phys., 66:47-101 p.

Rangel-Rojo, R. 2004. "Optica nolineal". CICESE class notes.

Rau, K. R., A. Guerra, A. Vogel, and V. Venugopalan 2004. "Investigation of laser-induced cell lysis using time-resolved imaging". Appl. Phys. Lett., 84(15):2940-2942 p.

Rau, K. R., P. A. Quinto-Su, A. N. Hellman, and V. Venugopalan 2006. "Pulsed laser microbeam-induced cell lysis: Time-resolved imaging and analysis of hydrodynamic effects". Biophysical Journal, 91:317-329 p.

Romo-Cárdenas, G. S. 2007. "Efectos de calentamiento y formacíon de burbuja inducidos con láseres pulsados en modelos de tejido-biológico". Tesis de Maestría, CICESE (Centro de Investigación Científica y Educación Superior de Ensenada), Km. 107 Carretera Tijuana-Ensenada BC 22860 Mexico.

Schäfer, H., S. Chemnitz, S. Schumacher, V. Koziy, A. Fischer, A. J. Meixner, D. Ehrhardt, and M. B/"ohm 2003. "Microfludics meets thin film electronics - a new approach towards an integrated intelligent lab-on-a chip". Smart Sensors, Actuators, and MEMS, 5116:764-775 p.

Schaffer, C. B., N. Nishimura, E. Glezer, A. M.-T. Kim, and E. Mazur 2002. "Dynamics of femtosecond laser-induced breakdown in water from femtoseconds to microseconds". Optics Express, 10(3):196-204 p.

Shuai, Y., A. Banerjee, D. Klozkin, and I. Papautsky 2008. "On-chip florescence detection with organic thin film devices for diposable lab-on-a-chip sensors". IEEE Sensors 2008 Conference, 1-4244-2581-5:122-126 p.

Siegrist, M. R. 1976. "Self-focusing in a plasma due to ponderomotive forces and relativistic effects". Optics Communications, 16(3):402-408 p.

Sinha, S. K., R. P. Sharma, and M. S. Sodha 1979. "Filamentation of a gaussian laser beam in a plasma". Plasma Physics, 21:283-289 p.

Sipe, J. E., J. F. Young, J. S. Preston, and H. M. van Driel 1983. "Laser-induced periodic surface structure. I. theory". Phys. Rev. B, 27(2):1141-1154 p.

Smith, W. L., P. Liu, and N. Bloembergen 1977. "Superbroadening in H_20 and D_2O by self-focused picosecond pulses from a $YAlG : Nd$ laser". Phys. Rev. A, 15(6):pp. 15-24 p.

Solis, J. and C. Afonso 2003. "Ultrashort-laser-pulse-driven rewritable phase-change optical recording in Sb-based films". Appl. Phys. A, 76:331-338 p.

Sorokina, I. T., E. Sorokin, and E. Wintner 1996. "Prismless passively mode-locked femtosecond $Cr : LiSGaF$ laser". Optics Letters, 21(15):1165-1168 p.

Spence, D. E., P. N. Kean, and W. Sibbett 1991. "60-fsec pulse generation from a self-made-locked $Ti : sapphire$ laser". Optics Letters, 16(1):42-45 p.

Sprangle, P., E. Esarey, and J. Krall 1996. "Self-guiding and stability of intense optical beams in gases undergoing ionization". Phys. Rev. E, 54(4):4211-4233 p.

Strickland, D. and G. Mourou 1985. "Compression of amplified chirped optical pulses". Optics Communications, 56(3):219-221 p.

Stuart, B. C., M. D. Feit, S. Herman, A. M. Rubenchik, B. W. Shore, and M. D. Perry 1996. "Nanosecond-to-femtosecond laser-induced breakdown in dielectrics". Phys. Rev. B, 53(4):1749-1762 p.

Sugioka, K., M. Masuda, T. Hongo, Y. Cheng, K. Shihoyama, and K. Midorikawa 2004. "Three-dimensional microfluidic structure embedded in photostructurable glass by femtosecond laser for lab-on-chip applications". Appl. Phys. A, 79:815-817 p.

Tang, S. B., H. Xia, M. O. Lai, and L. Lu 2006. "Amorphous $LiNiVO_4$ thin-film anode for microbatteries grown by pulsed laser deposition". Journal of Power Sources, 159:685-698 p.

Tsukamoto, M., N. Abe, Y. Soga, M. Yoshida, H. Nakano, M. Fujita, and J. Akedo 2008. "Control of electrical resitance of TiO_2 films by short-pulse laser irradiation". Appl. Phys. A., 93:193-196 p.

Vogel, A., S. Busch, and U. Parlitz 1996a. "Shock wave emission and cavitation bubble generation by picosecond and nanosecond optical breakdown in water". J. Acount. Soc. Am., 100(1):148-166 p.

Vogel, A., N. Linz, S. Freidank, and G. Paltauf 2008. "Femtosecond-laser-induced nanocavitation in water: Implications for optical breakdown threshold and cell surgery". Phy. Rev. Let, 100(038102).

Vogel, A., K. Nahen, D. Theisen, and J. Noack 1996b. "Plasma formation in water by picosecond and nanosecond nd:yag laser pulses—Part I: Optical breakdown at threshold and superthreshold irradiance". IEEE J. Quantum Electron., 2(4):847-861 p.

Vogel, A., J. Noack, G. Huttman, and G. Paltauf 2005. "Mechanisms of femtosecond laser nanosurgery of cells and tissues". Appl. Phys. B, 81:1015-1047 p.

Vogel, A. and V. Venugopalan 2003. "Mechanisms of pulsed laser ablation of biological tissues". Chemical Reviews, 103(2):577-644 p.

Vorobyev, A. Y. and C. Guo 2005. "Enhanced absorptance of gold following multipulse femtosecond laser ablation". Phys. Rev. B, 72(195422).

Vorobyev, A. Y. and C. Guo 2007. "Change in absorptance of metals follewing multi-pulse femtosecond laser ablation". J. Phys. CS, 59:597-585 p.

Weber, S., G. Riazuelo, P. Michel, R. Loubére, F. Walraet, V. T. Tikhonchuk, V. Malka, J. Ovadia, and G. Bonnaud 2004. "Modeling of laser-plasma interaction on hydrodynamic scales: Physics development and comparison with experiments". Laser and Particle Beams, 22:189-195 p.

Wu, B. and Y. C. Shin 2006. "Laser pulse transmission through the water breakdown plasma in laser shock peening". Appl. Phys. Lett., 88(041116).

Yang, J., J. Lian, H. Z. Bai, W. W. Cui, and Z. X. Guo 2005. "Cr_2O_3 film formed by surface oxidation of stainless steel irradiated by a $Nd:YAG$ pulsed laser". ISIJ International, 45(5):730 pp.

Yoshinaga, M., K. Yamamoto, N. Sato, K. Aoki, T. Morixawa, and A. Muramatsu 2009. "Remarkably enhanced photocatalytic activity by nickel nanoparticle deposition on sulfur-doped titanium dioxide thin film". Appl. Catalysis B, 87:239-244 p.

Young, J. F., J. S. Preston, H. M. van Driel, and J. E. Sipe 1983. "Laser-induced periodic surface structure. II. experiments on Ge, Si, Al, and brass". Phys. Rev. B, 27(2):1155 pp.

Young, P. E. 1995a. "Experimental observation of filementation growth in laser-produced". Phys. Plasmas, 2(7):2815-2825 p.

Young, P. E. 1995b. "Experimental observations of filamentation growth in laser-produced plasmas". Phys. Plasmas, 2(7):2815-2825 p.

Yu, C., Y. Wei, W. Hui-Chun, X. Han, and T. You-Wei 2007. "Intense laser beam guiding in self-induced electron cavitation channel in underdense plasmas". Chinese Physics, 16(2):456-463 p.

Yu, J., X. Zhao, and Q. Zhao 2000. "Effect of surface structure on photocotalytic activity of TiO_2 thin films prepared by sol-gel method". Thin Solid Films, 379:7-14 p.

Zhang, H., M. Tang, J. McCoy, and T. Her 2007. "Deposition of tungsten nanogratings induced by a single femtosecond laser beam". Optics Express, 15(10):5937-5948 p.

Zhuang, L., X. Xu, and H. Shen 2003. "A study on the gasochromic properties of WO_3 thin films". Surface & Coatings Technology, 167:217-220 p.

Zysset, B., J. G. Fujimoto, and T. F. Deutsch 1989. "Time-resolved measurements of picosecond opticol breakdown". Appl. Phys. B, 48:137-147 p.